

DYNAMICS IN CHIRAL MAGNETS

MAGNETIC AND ELECTRIC EXCITATIONS OF HELICES AND SKYRMIONS

DYNAMIK IN CHIRALEN MAGNETEN

MAGNETISCHE UND ELEKTRISCHE ANREGUNGEN
VON HELICES UND SKYRMIONEN

DIPLOMA THESIS
BY
JOHANNES WAIZNER



Institute for Theoretical Physics
Faculty of Mathematics and Natural Sciences
University of Cologne

April 2013

Under supervision of:

Prof. Dr. Achim Rosch

Second Examiner:

Priv.-Doz. Dr. Joachim Hemberger

Contents

Introduction	1
1 Chiral Magnets and their Phases	3
1.1 Key property of chiral magnets	3
1.2 Experimental phase diagrams	4
1.3 Ginzburg-Landau free energy functional	7
1.3.1 Anisotropies	8
1.3.2 Demagnetization fields and factors	8
1.3.3 Dipole-dipole interaction	10
1.4 Mean-field analysis	12
1.4.1 The conical phase	12
1.4.2 The Skyrmion phase	15
1.5 Theoretical construction of the phase diagram	17
2 Excitations and Linear Response Dynamics	19
2.1 Spin waves	19
2.1.1 Precession of magnetic moments in a magnetic field	20
2.1.2 Dispersion relation	21
2.2 Resonance	23
2.3 General derivation of the resonance frequencies	24
2.4 Momentum space calculations for numerical purposes	25
2.5 Resonance frequencies and their weights	27
3 Magnetic Excitations	29
3.1 Experimental setup	29
3.2 Excitations with $\mathbf{k} = 0$ and mode characteristics	31
3.2.1 The polarized phase: Kittel's formula	31
3.2.2 The conical phase	33
3.2.3 The Skyrmion phase	38
3.2.4 Summary and experimental comparison	39
3.3 Excitations with a finite \mathbf{k}	41
3.3.1 Consequences for data obtained by experiments	41
3.3.2 Dispersion relations	43
4 Electric Excitations	45
4.1 The polarization	45
4.1.1 Introduction and derivation of the static polarization in chiral materials	45
4.1.2 Directional dependance of the static polarization on external magnetic fields	46
4.1.3 The polarization and charge in the Skyrmion and conical phases	47

Contents

4.2	Linear response and the field-polarized phase	52
4.2.1	Discussion of the field-polarized phase	52
4.2.2	Symmetry arguments in the field-polarized phase	53
4.2.3	Numerical calculation of the resonance frequencies	55
4.2.4	Conflicts and prospects	57
	Summary	61
	Bibliography	66
	Acknowledgements	67

List of Figures

1.1	Crystal structure of MnSi	5
1.2	Experimental phase diagrams	5
1.3	Visualization of helical, conical and Skyrmion phase	6
1.4	Experimental detection of the conical phase	6
1.5	Different Skyrmion detections	6
1.6	High symmetry directions	8
1.7	Three examples for different demagnetization factors	9
1.8	Demagnetization field	10
1.9	Tripod of Q-vectors	15
1.10	From a hedgehog to a chiral Skyrmion configuration	16
1.11	Theoretical phase diagram of a helimagnet	17
2.1	Level splitting due to the Zeeman effect in a finite magnetic field	20
2.2	Precession of a magnetization \mathbf{M} around a static magnetic field \mathbf{H}_0	21
2.3	Dispersion relation of spin-waves	23
2.4	Schematic picture of resonance	23
2.5	Reziprocal conical and Skyrmion lattice	25
3.1	Convention of the experimental setup	30
3.2	Cross-section of the experimental setup	31
3.3	Gray scale plots of resonance experiment	31
3.4	Qualitative plots of theoretical resonance frequencies in polarized phase	33
3.5	Kittel mode with outer field parallel to disc surface	33
3.6	Plots of theoretical resonance frequencies in the conical phase	35
3.7	Resonance plots incl. weights	36
3.8	Illustration of the excitations in the conical phase	37
3.9	Resonances in Skyrmion phase	39
3.10	Mode visualization	40
3.11	Experimental results and comparison	40
3.12	Relation between a finite \mathbf{k} and $\mathbf{k} = 0$ excitation	42
3.13	Experimental results and comparison	43
3.14	Dispersion relations in the conical phase	44
3.15	Dispersion relations in the Skyrmion phase	44
4.1	Polarization of the Skyrmion phase (autoscaled)	48
4.2	Polarization of the Skyrmion phase	49
4.3	Polarization and charge of the Conical phase (autoscaled)	50
4.4	Polarization and charge of the Conical phase	51
4.5	Comparison of calculated absorption spectra for a.c. magnetic and electric fields	57

List of Figures

4.6	Figure of the magnetic field induced by a changing electric field	57
4.7	Electric resonances in the conical phase	59
4.8	Electric resonances in the Skyrmion phase	60

List of Tables

4.1	Directional dependence of electric excitations in the field-polarized phase	54
4.2	Effect of symmetries on the polarization for $\mathbf{H}_0 \parallel [100]$	55
4.3	Effect of symmetries on the polarization for $\mathbf{H}_0 \parallel [1\bar{1}0]$	55

Introduction

“Now, there are some curious bodies in nature (of which I have two specimens on the table) which are called *magnets* or *loadstones* ores of iron, of which there is a great deal sent from Sweden. They have the attraction of gravitation, and attraction of cohesion, and certain chemical attraction; but they also have a great attractive power, for this little key is held up by this stone.”

Michael Faraday

The concept of magnetism has fascinated people for centuries. In the eighteen hundreds, people were still much in awe of magnets and its properties as can be seen by how Faraday introduces ferromagnets in one of his lecture courses [1]. This has not changed a bit since then and even nowadays there is still so much to discover. Quite recently in 2009, the discovery of so-called Skyrmions has been made in MnSi and opened up a whole new field of research possibilities. Skyrmions are topologically stable, whirl-like objects. Their general description goes back to 1961, when T.H.R. Skyrme introduced them as quasiparticles, that act as defects in a non-linear meson field theory [2]. In the magnetic case they form a two-dimensional whirl structure, opposed to the three-dimensional description used in Skyrme’s model, similar the mixed state of type-II superconductors [3]. Experimentally, such a Skyrmion lattice was first observed in the chiral magnet MnSi in 2009 [4].

Since then, Skyrmions have attracted more and more interest. They turned out not to be a unique property of MnSi but present in many chiral materials. Discoveries range from metals to insulators both in bulk form or as thin films, and from low temperature ranges around 40 K up to almost room temperature in thin films [5]. For most of our studies in this thesis, we will focus on three concrete bulk materials namely metallic MnSi and $\text{Fe}_{0.8}\text{Co}_{0.2}\text{Si}$ [6] and insulating Cu_2OSeO_3 [7].

Methods of experimental detection have been quite numerous as well, the first being neutron scattering [4], but also Lorentz transmission electron microscopy [8] and most recently magnetic force microscopy [9].

What make Skyrmions even more amicable are the novel effects they bring along into the realm of magnetic materials. Most prominent examples include possible new applications in computer memory storage devices [10] due to the extremely low spin-polarized currents needed to move them [11, 12], rotation of an entire Skyrmion lattice caused by spin torques or applied field or temperature gradients [13], and even the creation of magnetic monopoles in bulk materials as topological defects, that arise when two Skyrmion lines merge [9].

In some setups, Skyrmions even exist individually in a crossover between the Skyrmion lattice and ferromagnetic phase [8], which opens up the prospect of using them to efficiently couple electric or spin current to a magnetic structure, which could yield numerous applications in nanotechnology [14], especially, because a current-induced motion of Skyrmions seems to be little affected by disorder and damping.

Introduction

Also multiferroic properties play a role of growing importance. Helical and skyrmionic spin textures influence the equilibrium charge distribution and induce a local polarization within a material. Because of the magneto-electric effect, this could enable manipulations of Skyrmion lattices or individual Skyrmions by the use of electric fields and that, at least in insulators, even without energy loss due to joule heating [7].

The endeavor goes on in this new and exciting field and a next step is to gain an even better understanding of how Skyrmions behave and can be manipulated.

To this end, the present thesis focuses on the response of chiral magnets, which provide a Skyrmion lattice under appropriate conditions, to magnetic and electric excitations.

The first chapter serves as an introduction to the field. Characteristics and properties of both materials and occurring phases are stated and explained in a static limit. We continue in the following chapter by providing an insight into the methods of calculation.

Magnetic excitations are covered in chapter 3. The main focus lies on developing a theory that describes experimental data obtained by research groups of Prof. Dr. Pfeleiderer and Prof. Dr. Grundler from the Technical University of Munich.

The final chapter contains an introduction to the electric properties and excitations of helices and Skyrmions.

Chiral Magnets and their Phases

TO START OFF, we introduce chiral magnets as our material of interest. Their difference to common ferromagnets is explained, and a more thorough characterization in terms of crystal structure and of the ordered phases is given. Explicit phase diagrams are presented and the individual phases are described in a mean-field approximation.

1.1 Key property of chiral magnets

Ordinary ferromagnets are quite well understood nowadays. Their description is mainly characterized by the exchange interaction [15]. Taking the Heisenberg-exchange Hamiltonian for a lattice of spins as an example, one can see quite easily, that the energy is lowest, if the spins are aligned in parallel for $J_{ij} > 0$.

$$\mathcal{H}_{Heis} = - \sum_{i,j} J_{ij} \mathbf{S}_i \cdot \mathbf{S}_j \quad (1.1)$$

Here, the summation is over all lattice sites i and j and J_{ij} , the exchange coupling constant, is a function of the vector connecting i th and j th lattice sites. The strength of J_{ij} generally decays exponentially, which makes it often possible to fix J_{ij} to a constant value J for nearest neighbors and zero otherwise. This ultimately limits the summation just to nearest neighbors, which is commonly denoted by $\langle i, j \rangle$. The result of $J > 0$ is therefore the formation of a ferromagnet, whereas $J < 0$ will yield an anti-ferromagnet, in which neighboring spins are aligned antiparallel. This of course depends on the lattice structure, that must, for example, not yield a frustrated arrangement. Frustration means, that the system is unable to satisfy all its bounds, e.g. the anti-ferromagnetic Ising model on a triangular lattice [16].

The description of chiral magnets goes back to a phenomenological theory by Dzyaloshinsky [17], that has been refined by Moriya [18] a couple of years later. In the original theory, Dzyaloshinsky studied *weak ferromagnetism* in α -Fe₂O₃, MnCO₃ and CoCO₃. Weak ferromagnetism occurs for example in Anti-ferromagnets with an anisotropic exchange interaction, which results in a small ferromagnetic component perpendicular to the spin axis [19]. Dzyaloshinsky found, that the surprisingly low magnetic moment, which acts as the spontaneous magnetization, can be explained by a term, that favors a canted spin arrangement in contrast to the expected antiferromagnetic arrangement.

$$\mathcal{H}_{DM} = \mathbf{D}_{ij} \cdot (\mathbf{S}_i \times \mathbf{S}_j)$$

The vector \mathbf{D}_{ij} is called the Dzyaloshinsky-vector. In their studied material α -Fe₂O₃ it points

1 Chiral Magnets and their Phases

along a fixed axis, that is given by the crystal structure.

A continuum theory approach is given by a Ginzburg-Landau free energy description. This theory is very powerful in the vicinity of phase transitions. Here, we consider the change from a magnetically disordered phase to a magnetically ordered one. Since the degrees of freedom, which describe the transition, are long wavelength collective oscillations of spins, it is possible to *coarse grain* the system to a scale, which is much larger than the atomic lattice spacing and where we can define a vector field for the magnetization $\mathbf{M}(\mathbf{r})$ at position \mathbf{r} instead of trying to describe it fully microscopically. The continuous field $\mathbf{M}(\mathbf{r})$ then describes the average of the microscopic spins around the point \mathbf{r} and is the order parameter of our theory.

The theory assumes, that the order parameter is small in the vicinity of the phase transition. Equilibrium thermodynamics is then completely determined by the free energy functional F of temperature and the (local) order parameter. F needs to be invariant under the symmetry group of the disordered phase. Short range interaction is described through gradient expansions [16]. Important for the case of chiral magnets is now, that its lattice has no inversion symmetry. This allows a gradient term of linear order, which represents the Dzyaloshinsky-Moriya interaction. The interaction responsible for this term, is the spin-orbit coupling. The linear order term has the form

$$F_{DM} = \int d^3r 2D \mathbf{M}(\mathbf{r}) \cdot (\nabla \times \mathbf{M}(\mathbf{r})) \quad (1.2)$$

where D is the pre-factor and basically the coupling strength. The to (1.1) corresponding continuum version has the form

$$F_{Heis} = \int d^3r J(\nabla \mathbf{M})^2 \quad (1.3)$$

In a chiral magnet, both terms are present. While F_{Heis} favors parallel arrangement of neighboring spins, F_{DM} favors orthogonal arrangement of neighboring spins. This competition leads to a compromise, which manifests itself in a gradually canted arrangement, for example a helical spin structure. The sign of D in (1.2) fixes the chirality of the resulting helices. A right handed helix is given by $D > 0$ and a left handed otherwise [20].

1.2 Experimental phase diagrams

The experiments under consideration in this thesis are conducted on three different materials, namely MnSi, $\text{Fe}_{0.8}\text{Co}_{0.2}\text{Si}$ and Cu_2OSeO_3 . All materials crystalize in the cubic crystal structure B20, with their non-centrosymmetric space group being P2₁3. A picture of the crystal structure of MnSi as an example can be seen in Figure 1.1.

The properties of $\text{Fe}_{1-x}\text{Co}_x\text{Si}$ depend on its Co-concentration. To achieve a helimagnetic metallic phase, the Kondo insulator FeSi has to be doped with cobalt, in our case with a ratio of one per four iron atoms, so $x = 0.2$. The possible doping range to achieve a helimagnetic metal goes up to a cobalt concentration of roughly 80%. Some experiments, that we also refer to, use a ratio of 50% doping [21]. While MnSi and $\text{Fe}_{0.8}\text{Co}_{0.2}\text{Si}$ are both helimagnetic metallic, Cu_2OSeO_3 is of insulating nature. Although the latter is characterized by the same space group, its atom coordination is very different [7]. The materials described above possess four interesting and different magnetic phases: a field-polarized ferromagnetic phase, a helical, conical and a Skyrmion phase. In the polarized phase, all spins are aligned parallel. The other phases are conceptually visualized in Figure 1.3. The figures need to be imagined in a bulk setting. The helical and conical picture are hence to be seen as multiple helices next to each other. The arrows represent the vector field $\mathbf{M}(\mathbf{r})$. Whereas the propagation direction of the conical helix is parallel to an applied magnetic field $\mathbf{M}(\mathbf{r})$ the direction in the helical phase is less dependent on an external

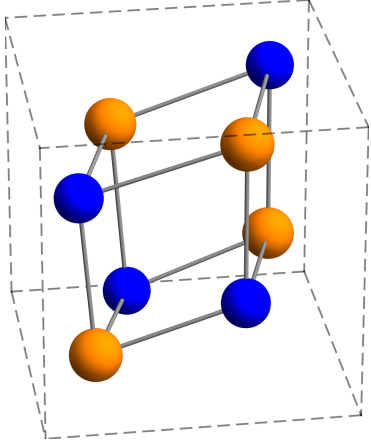


Figure 1.1: Crystal structure of MnSi. Manganese atoms with a radius of 127pm are shown in orange and Silicon atoms with a radius of 117.6pm in blue. The unit cell contains atoms at positions $(u, u, u; \frac{1}{2}+u, \frac{1}{2}-u, \bar{u}; \frac{1}{2}-u, \bar{u}, \frac{1}{2}+u; \bar{u}, \frac{1}{2}+u, \frac{1}{2}-u)$, with $u_{\text{Mn}} = 0.183$ and $u_{\text{Si}} = 0.845$ [22].

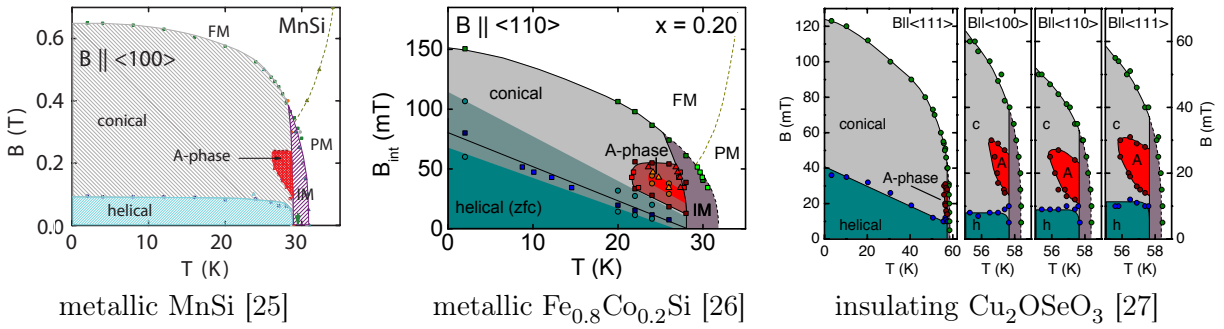


Figure 1.2: Experimental phase diagrams of the three studied materials in bulk form. Thin films will lead to a broader Skyrmion phase (here called A-phase) [7]. The intermediate phase (IM) stands for a fluctuation-induced first-order transition [28] between the paramagnetic and helimagnetic phases of the chiral magnet.

magnetic field but fixed by cubic anisotropy terms as described in subsection 1.3.1. In MnSi it is, for example, the $\langle 111 \rangle$ direction. The Skyrmion lattice, as it is depicted in Figure 1.3, forms in a plane perpendicular to the magnetic field. Furthermore, it is translation invariant in field-direction, which leads to a tube-like structure in a way, that circles of constant magnetization in \hat{e}_z -direction form hollow cylinders.

The whereabouts of the phases depend strongly on temperature and the strength of the applied magnetic field. Phase diagrams of the three studied materials are shown in Figure 1.2.

Without such an external magnetic field and below a critical temperature of $T_c^{\text{MnSi}} \approx 29.5$ K, helical magnetic order develops in MnSi [4]. In $\text{Fe}_{1-x}\text{Co}_x\text{Si}$, the critical temperature depends on the doping of Co and has its maximum of $T_c^{\text{Fe}_{1-x}\text{Co}_x\text{Si}} \approx 60$ K at $x = 0.35$ [23]. According to Kohn [24] $T_c^{\text{Cu}_2\text{OSeO}_3} \approx 58.8$ K.

The phase transition from the helical into the conical phase occurs at a temperature dependent critical field $H_{c1}(T)$. The transition to the polarized phase happens at the critical field $H_{c2}(T)$. The phase diagram also depends on the shape of the specimen, especially concerning the Skyrmion phase. While its phase space is merely a small pocket in a bulk material, it broadens in the case of a thin film, where the external field is applied perpendicular to the surface. When the film is thin enough, there is not enough room to build up an entire conical helix pointing in field direction. As a result, the conical phase is suppressed and a Skyrmion arrangement much easier stabilized, even down to $T = 0$ K [8].

Experimental detection of the different phase has been done predominantly by neutron scattering experiments. In the conical phase, one sees two scattered dots pointing along the direction

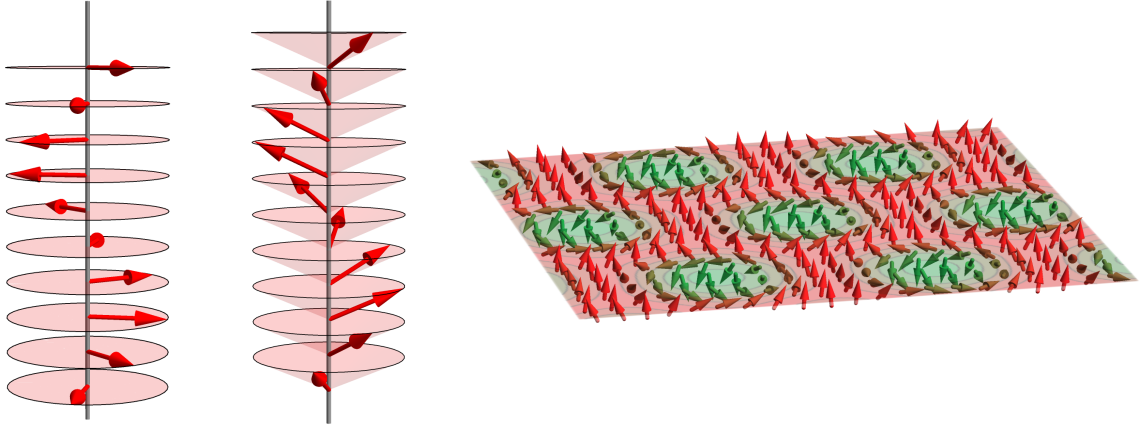


Figure 1.3: From left to right: helical phase, conical phase and Skyrion phase. To obtain the three dimensional phases, the pictures of the helical and conical phase need to be imagined in array translated perpendicular to the helix axis. The Skyrion picture has to be seen as translation invariant in direction of the plane normal.

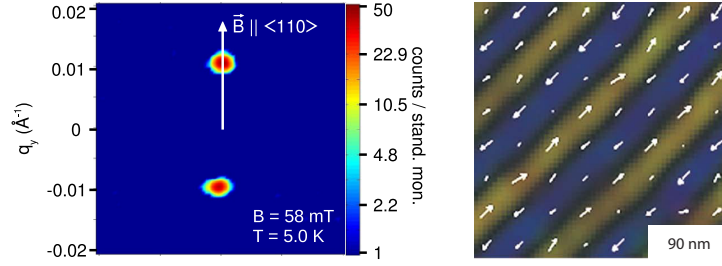


Figure 1.4: Experimental detection of the conical phase. **Left:** Typical small angle neutron scattering pattern in the conical phase in bulk Cu_2OSeO_3 [27]. **Right:** experimentally observed real-space images of helical spin texture at zero magnetic field via Lorentz transmission electron microscopy in a thin film of $\text{Fe}_{0.5}\text{Co}_{0.5}\text{Si}$ [8].

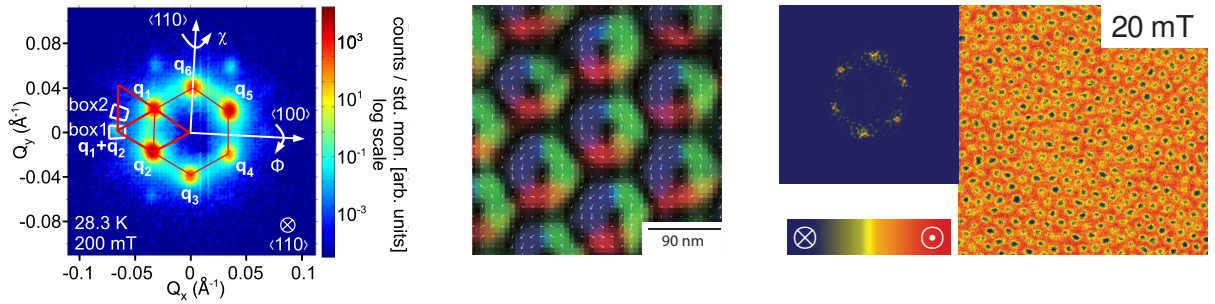


Figure 1.5: Experimental detection of the Skyrion lattice phase. **Left:** Typical intensity distribution obtained by small angle neutron scattering experiments on bulk MnSi . An applied magnetic field is aligned parallel to the incident neutron beam. Notice the higher order scattering peaks [29]. **Middle:** Detection of Skyrmions in thins films of $\text{F}_{0.5}\text{Co}_{0.5}\text{Si}$ via Lorentz transmission microscopy [8]. **Right:** Typical magnetic force microscopy data at the surface of $\text{Fe}_{0.5}\text{Co}_{0.5}\text{Si}$ blue (red) areas indicate a magnetization pointing into (out of) the plane surface, respectively. The inset on the left hand side shows the Fourier transformation of the real space signal [9].

of the applied magnetic field, as can be seen in Figure 1.4. They indicate the pitch-vector of the underlying helical magnetic structure. In the purely helical phase those two spots lie along the axes, that are preferred by cubic anisotropy. Lorentz transmission electron microscopy measurements show the conical and helical phases as a striped area, which is shown in Figure 1.4, too. A lattice of Skyrmions has first been experimentally observed via neutron scattering in MnSi [4], but later also as a real-space picture by Lorentz transmission electron microscopy through a thin film [8] and via magnetic force microscopy at the surface of bulk $\text{Fe}_{0.5}\text{Co}_{0.5}\text{Si}$ (cf. Figure 1.5).

1.3 Ginzburg-Landau free energy functional

The general free energy, that accommodates terms to describe all important occurring effects as well as the time dependent magnetic and electric perturbations, has the form

$$\tilde{F}[\tilde{\mathbf{M}}] = \int d^3\tilde{r} \left(\tilde{f}_0 + \tilde{f}_{\text{demagnetization}} + \tilde{f}_{\text{anisotropy}} + \tilde{f}_{\text{oszil. magnetic}}(t) + \tilde{f}_{\text{oszil. electric}}(t) \right) \quad (1.4)$$

The term \tilde{f}_0 is the most important one, as it already generates by itself the underlying magnetic structure, and it is given by

$$\tilde{f}_0 = (r_0 \tilde{\mathbf{M}}^2 + J \underbrace{(\nabla \tilde{\mathbf{M}})^2}_{:=\partial_\alpha \tilde{M}_\beta \partial_\alpha \tilde{M}_\beta} + 2D \tilde{\mathbf{M}} \cdot (\nabla \times \tilde{\mathbf{M}}) + U(\tilde{\mathbf{M}}^2)^2 - \mu_0 \tilde{\mathbf{H}} \cdot \tilde{\mathbf{M}}) \quad (1.5)$$

The first two terms in (1.5) are the usual quadratic terms with the common gradient term that favours parallel alignment of the magnetization. The third term represents the Dzyaloshinsky-Moriya interaction (1.2), responsible for the canted contribution, and the last term is the Zeemann-term, that couples the magnetization to an external magnetic field. The quartic term stabilizes the magnetic order, which will be explained in more detail later, and accounts in lowest order for the effects of mode-mode interactions. The prefactors of the individual terms still depend on microscopic interactions as well as external parameters such as temperature. The pitch length Q of the generated helices is given by the competition between the exchange and the Dzyaloshinsky-Moriya interaction strengths $Q = D/J$.

Most of the time we do our calculations in rescaled units. Advantages are, for example, that results can be described with less pre-factors, but rescaling also introduces a new parameter t , that is zero at the critical temperature as well as proportional to temperature. Upon re-scaling all lengths as $\mathbf{r} = Q\tilde{\mathbf{r}}$, magnetizations as $\mathbf{M} = [U/JQ^2]^{1/2}\tilde{\mathbf{M}}$, and magnetic fields as $\mathbf{H} = [U/(JQ^2)^3]^{1/2}\tilde{\mathbf{H}}$, we arrive with $\kappa = J^2Q/U$ and $t = r_0/(JQ^2) - 1 \propto T - T_c$ at

$$F_0[\mathbf{M}] = \kappa \int d^3r f_0 = \kappa \int d^3r \left((t+1)\mathbf{M}^2 + (\nabla \mathbf{M})^2 + 2\mathbf{M} \cdot (\nabla \times \mathbf{M}) + \mathbf{M}^4 - \mu_0 \mathbf{H} \cdot \mathbf{M} \right) \quad (1.6)$$

One may note, that only a linear dependence of temperature is kept in the parameters, because one linearizes all T dependences around T_c in the Ginzburg-Landau approach. The free energy functional hence takes the form

$$F[\mathbf{M}] = \kappa \int d^3r \left(f_0 + f_{\text{demagnetization}} + f_{\text{anisotropy}} + f_{\text{oszil. magnetic}}(t) + f_{\text{oszil. electric}}(t) \right) \quad (1.7)$$

Cubic anisotropy effects are expressed by terms in $f_{\text{anisotropy}}$. Although they are responsible for a finite phase space area of the purely helical phase, we will neglect them in our calculations because, for one, they are small compared to the remaining parts of the free energy, but also because we are mostly interested in the conical and Skyrmion phases.

Shape dependences of the calculated resonance frequencies are taken into account by $f_{\text{demagnetization}}$.

This term does not change the general appearance of the magnetic structure, but is of grave importance in the calculations of resonance frequencies, which play a major role in this thesis. As they influence the effective internal field, they also influence the phase diagram to some degree as is shown in subsection 1.4.1. Therefore, this term will be explained and thoroughly discussed in the next subsections.

The remainder of this chapter will deal with the static case. That means, that the time dependent contributions $f_{\text{oszil. magnetic}}(t)$ and $f_{\text{oszil. electric}}(t)$ will be set to zero. Later, they will play the role of the magnetic and electric excitation fields, respectively.

1.3.1 Anisotropies

Although we neglect those terms in the calculations, it is worthwhile to keep their general function at the back of one's mind. Already mentioned was the effect of anisotropies to be responsible for the appearance of a purely helical phase at a finite applied magnetic field and a pitch direction different to the field direction [30, 31]. Experiments suggest a term, that minimizes the free energy at low fields, when the helix points in $\langle 111 \rangle$ direction. That means a term, that is minimal for the pitch vector $\mathbf{Q} \parallel \langle 111 \rangle$. A term to lowest order in spin-orbit coupling that favors exactly this alignment is given by [32]

$$f_{\text{anisotropy, hel.}} = (\partial_x^4 + \partial_y^4 + \partial_z^4) \mathbf{M}^2 \quad (1.8)$$

The consequence of favoring a distinct direction at low fields, is a phase transition from high to low fields, i.e. in our case from the conical into the helical phase. The transition itself follows two characteristic patterns. In one, the external magnetic field points in an arbitrary direction. When its strength is reduced, a crossover takes place, and the conical helix becomes gradually the purely helical helix. The story is different, when the magnetic field points into a direction of higher symmetry like $\langle 110 \rangle$ or $\langle 100 \rangle$, cf. Figure 1.6. In the former case, the helix now has two possible $\langle 111 \rangle$ directions which are closest to the applied field direction to choose from. In the latter case, there are even four options. The result is, that this transition is spontaneous, i.e. of second order [33].

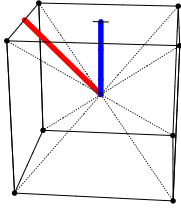


Figure 1.6: Special high symmetry directions (see text).
Red: $\langle 110 \rangle$ **Blue:** $\langle 100 \rangle$
Dotted: $\langle 111 \rangle$.

The orientation of the Skyrmion lattice is, without anisotropies, just characterized by the magnetic field direction. As such, it has the liberty to freely turn about this axis, without changing the free energy. This freedom of rotational symmetry is however broken by higher order spin-orbit coupling [20]. To fix the thus far arbitrary rotation angle Φ to a preferred direction, one needs an effective potential of the form $\cos(6n\Phi + \phi_0)$ with $n = 1, 2, \dots$ and some constant phase ϕ_0 , because it needs to accommodate the six-fold rotational symmetry of the Skyrmion lattice. One example of a term in lowest order perturbation theory, that can lock Φ into a fixed position, is

$$f_{\text{anisotropy, Sky.}} = (\partial_x^3 \mathbf{M})^2 + (\partial_y^3 \mathbf{M})^2 + (\partial_z^3 \mathbf{M})^2 \quad (1.9)$$

1.3.2 Demagnetization fields and factors

To motivate the inclusion of demagnetizing fields and factors, one can cite a paper by Charles Kittel from 1947 [34]. In this paper he comments on resonance experiments conducted by J. H. E. Griffiths in the 1940s. His results showed values for the resonance frequencies, that were two to six times larger than the expected frequency, which was the Larmor frequency, that we explain in subsection 2.1.1. His attempts, to describe this discrepancy by introducing the Lorentz cavity

force into his calculation, where unsuccessful and according to Kittel not even justified. Kittel on the other hand deduced, that the geometry of the specimen played an important role. Since one has to deal with a large magnetization, the strength of the demagnetization field becomes relevant and has to be taken into account. Translated to our setup it would mean, that, including only the initial free energy density \tilde{f}_0 in (1.4), the theory for the polarized phase would predict solely a linear dependence of the resonance frequency on the strength of the magnetic field and the Landé factor. But first things first: this subsection provides a short introduction to demagnetization fields.

A magnetized body produces effective magnetic surface charges (cf. Figure 1.8). From the outside, this results in a collective magnetic moment, which aligns parallel to an external magnetic field \mathbf{H}^o . Inside the material, the surface charges create another field \mathbf{H}^D called demagnetizing field. Its name hints to the fact, that it acts against the magnetization and therefore in general also against the external magnetic field. As a result, the effective internal magnetic field \mathbf{H}^i consists of both those components.

$$\mathbf{H}^i = \mathbf{H}^o + \mathbf{H}^D \quad (1.10)$$

The demagnetizing field can be characterized via demagnetization factors N_i , with $i = x, y, z$ indicating the principal axes of the specimen. This is only true for ellipsoidal shapes, where \mathbf{H}^D is constant. An arbitrary shape results in an inhomogeneous internal magnetic field. With this definition the demagnetizing field has the form

$$\tilde{\mathbf{H}}^D = - \begin{pmatrix} N_x & 0 & 0 \\ 0 & N_y & 0 \\ 0 & 0 & N_z \end{pmatrix} \cdot \tilde{\mathbf{M}} =: -\underline{N} \cdot \tilde{\mathbf{M}} \quad (1.11)$$

The tilde notation indicates the true physical fields. One may note, that the demagnetization factors do not depend on the scale of the body but purely on the shape. An additional condition set for the N_i is that their sum equals one in SI-units and 4π in cgs-units.

$$\text{(SI)} \quad N_x + N_y + N_z = 1 \quad (1.12)$$

For example a rod in z-direction will have a smaller demagnetizing field in z-direction. For an infinitely long, cylindrical, rotation invariant rod we will get $N_x = N_y = \frac{1}{2}$ and $N_z = 0$. A disc, or in the ideal case an infinite plane, with the plane-normal in z-direction has $N_x = N_y = 0$ and $N_z = 1$. A perfect sphere will yield $N_x = N_y = N_z = \frac{1}{3}$ and so forth. Corresponding pictures can be seen in Figure 1.7.

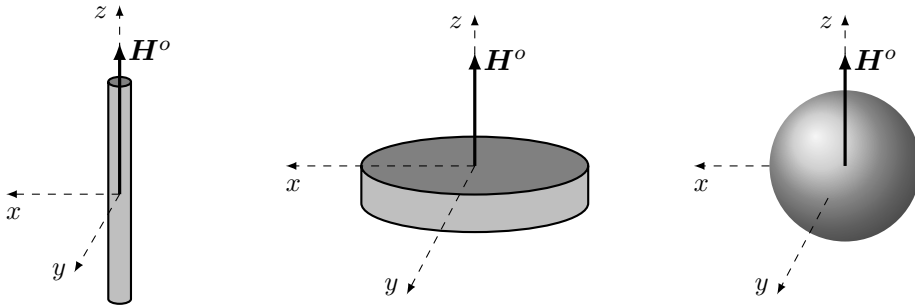


Figure 1.7: Examples of three different shapes with three mainly different demagnetization factors. **Left:** rod or infinite cylinder with $N_x = N_y = \frac{1}{2}$ and $N_z = 0$, **Middle:** disk or infinite surface (dark gray) with $N_x = N_y = 0$ and $N_z = 1$, **Right:** perfect sphere with $N_x = N_y = N_z = \frac{1}{3}$.

1 Chiral Magnets and their Phases

Remembering, that $\mu_0 \mathbf{H}^{eff} = -\frac{\delta F}{\delta \mathbf{M}}$ gives a contribution of

$$\tilde{f}_{\text{demagnetization}, \mathbf{k}=0} = \frac{1}{2} \mu_0 \tilde{\mathbf{M}} \cdot \underline{\mathbf{N}} \cdot \tilde{\mathbf{M}} \quad (1.13)$$

to the free energy density [35]. Rescaling all quantities like in the beginning of this section gives us an additional prefactor $\frac{1}{\alpha}$.

$$f_{\text{demagnetization}, \mathbf{k}=0} = \frac{1}{2} \frac{\mu_0}{JQ^2} \mathbf{M} \cdot \underline{\mathbf{N}} \cdot \mathbf{M} = \frac{1}{2} \frac{\mu_0}{\alpha} \mathbf{M} \cdot \underline{\mathbf{N}} \cdot \mathbf{M} \quad (1.14)$$

We defined $\alpha = JQ^2 = \frac{D^2}{J}$, which will be important later on, to switch between the rescaled units and the true order parameter units, which are needed to establish a connection to the experiments.

Since these formulas were derived in the long wavelength limit $|\mathbf{k}| \ll 1/L$, with L being the extent of the specimen, it is important to realize, that (1.14) is only the contribution to the free energy for basically $\mathbf{k} = 0$. For a finite \mathbf{k} , long-range dipole-dipole interaction needs to be considered.

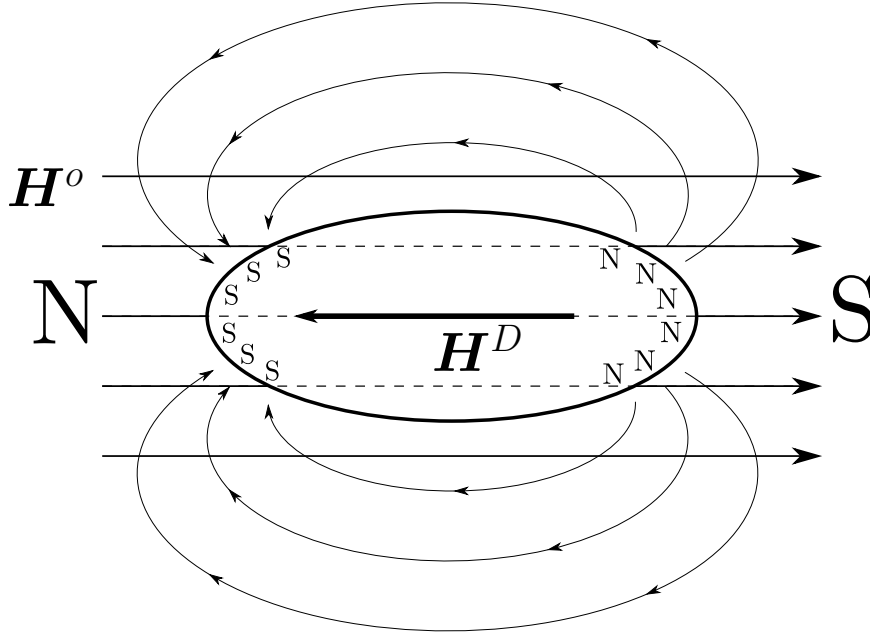


Figure 1.8: Illustration of the creation of a demagnetizing field \mathbf{H}^D . A magnetic body is subject to an outer magnetic field \mathbf{H}^o . Magnetic surface charges arise and the resulting field inside the body acts against the outer magnetic field.

1.3.3 Dipole-dipole interaction

Two magnetic dipoles \mathbf{m}_1 and \mathbf{m}_2 that are separated by \mathbf{r} have an estimated interaction energy U of

$$U = \frac{1}{r^3} [\mathbf{m}_1 \cdot \mathbf{m}_2 - 3(\mathbf{m}_1 \cdot \hat{\mathbf{r}})(\mathbf{m}_2 \cdot \hat{\mathbf{r}})]$$

For typical magnetic solids, U amounts to no more than 10^{-4} eV. This is small compared to the exchange coupling and therefore dipolar interaction effects usually play a secondary role in the realm of magnetic ordering [15].

The most interesting part to us of this interaction is, how it affects the internal magnetic field and hence the resonance frequencies in our experiments. Regarding the case of isotropic and parallel spin arrangement ($\mathbf{k} = 0$), the situation can be well described by demagnetization factors, as is explained in the previous section. If an inhomogeneous field with a considerable wave vector is used to excite the system, it is necessary to have a closer look at the field $\tilde{\mathbf{H}}_s$ due to the spins themselves. Ultimately we would like to obtain an additional term, that describes the coupling of the magnetization to this additional field contribution.

Since its origin are the microscopic magnetic moments, $\tilde{\mathbf{H}}_s$ depends on the distribution of the magnetization \mathbf{M} . The physical magnetic induction $\tilde{\mathbf{B}} = \mu_0(\tilde{\mathbf{H}} + \tilde{\mathbf{M}})$, which suggest the application of Maxwells equations to establish a relation between the two entities $\tilde{\mathbf{M}}$ and $\tilde{\mathbf{H}}_s$.

$$\nabla \cdot \tilde{\mathbf{B}} = \mu_0 \nabla \cdot (\tilde{\mathbf{H}}_s + \tilde{\mathbf{M}}) \stackrel{!}{=} 0 \quad \text{and} \quad \nabla \times \tilde{\mathbf{H}}_s = 0 \quad (1.15)$$

or in the rescaled units with $\mathbf{B} = (U/JQ^2)^{1/2} \tilde{\mathbf{B}}$

$$\nabla \cdot \mathbf{B} = \mu_0 \nabla \cdot (\alpha \mathbf{H}_s + \mathbf{M}) \stackrel{!}{=} 0 \quad \text{and} \quad \nabla \times \mathbf{H}_s = 0 \quad (1.16)$$

One can toggle hence between the physical and rescaled units in the following calculation, by setting $\alpha = 1$ for the physical units and $\alpha = JQ^2$ in the rescaled case. The Fourier representations of the magnetization $\mathbf{M}(\mathbf{r})$ and \mathbf{H}_s are

$$\mathbf{M}(\mathbf{r}) = \sum_{\mathbf{q}} \mathbf{m}_{\mathbf{q}} e^{i\mathbf{q} \cdot \mathbf{r}} \quad \text{and} \quad \mathbf{H}_s(\mathbf{r}) = \sum_{\mathbf{q}} \mathbf{h}_{s,\mathbf{q}} e^{i\mathbf{q} \cdot \mathbf{r}}$$

Using the in the second equation of (1.16) fixes the direction of $\mathbf{h}_{s,\mathbf{q}}$.

$$\begin{aligned} \nabla \times \mathbf{H}_s &= \sum_{\mathbf{q}} (\mathbf{q} \times \mathbf{h}_{s,\mathbf{q}}) e^{i\mathbf{q} \cdot \mathbf{r}} \stackrel{!}{=} 0 \\ &\leadsto \mathbf{q} \parallel \mathbf{h}_{s,\mathbf{q}} \end{aligned} \quad (1.17)$$

The first equation of (1.16) gives

$$\begin{aligned} \nabla \cdot \mathbf{M} &= \sum_{\mathbf{q}} (\mathbf{m}_{\mathbf{q}} \cdot \mathbf{q}) e^{i\mathbf{q} \cdot \mathbf{r}} \stackrel{!}{=} -\alpha \nabla \cdot \mathbf{H}_s = \alpha \sum_{\mathbf{q}} (\mathbf{h}_{s,\mathbf{q}} \cdot \mathbf{q}) e^{i\mathbf{q} \cdot \mathbf{r}} \\ \mathbf{m}_{\mathbf{q}} \cdot \mathbf{q} &= \alpha \mathbf{h}_{s,\mathbf{q}} \cdot \mathbf{q} \stackrel{(1.17)}{=} \alpha |\mathbf{h}_{s,\mathbf{q}}| |\mathbf{q}| \\ \leadsto |\mathbf{h}_{s,\mathbf{q}}| &= -\frac{1}{\alpha} \frac{(\mathbf{m}_{\mathbf{q}} \cdot \mathbf{q})}{|\mathbf{q}|} \\ \leadsto \mathbf{H}_s &= -\frac{1}{\alpha} \sum_{\mathbf{q}} \frac{(\mathbf{m}_{\mathbf{q}} \cdot \mathbf{q})}{|\mathbf{q}|} \hat{\mathbf{q}} e^{i\mathbf{q} \cdot \mathbf{r}} \end{aligned} \quad (1.18)$$

For \mathbf{H}_s is an additional component to the internal magnetic field, an additional term F_{dd} in the free energy needs arise with the property $\frac{\delta F_{dd}}{\delta \mathbf{M}} = -\mu_0 \mathbf{H}_s$. A first guess is

$$\begin{aligned} -\mu_0 \int d^3r \mathbf{M} \cdot \mathbf{H}_s &= \frac{\mu_0}{\alpha} \int d^3r \left(\sum_{\mathbf{q}} \mathbf{m}_{\mathbf{q}} e^{i\mathbf{q} \cdot \mathbf{r}} \right) \cdot \left(\sum_{\mathbf{q}'} \mathbf{h}_{s,\mathbf{q}'} e^{i\mathbf{q}' \cdot \mathbf{r}} \right) \\ &= \frac{\mu_0}{\alpha} \sum_{\mathbf{q}, \mathbf{q}'} \mathbf{m}_{\mathbf{q}} \cdot \frac{(\mathbf{m}'_{\mathbf{q}'} \cdot \mathbf{q}')}{|\mathbf{q}'|^2} \mathbf{q}' \underbrace{\int d^3r e^{i(\mathbf{q}+\mathbf{q}') \cdot \mathbf{r}}}_{\delta_{\mathbf{q}+\mathbf{q}'}} \\ &= \frac{\mu_0}{\alpha} \sum_{\mathbf{q}} \frac{(\mathbf{m}_{\mathbf{q}} \cdot \mathbf{q})(\mathbf{m}_{-\mathbf{q}} \cdot \mathbf{q})}{|\mathbf{q}|^2} \end{aligned} \quad (1.19)$$

1 Chiral Magnets and their Phases

To substantiate this guess, it is good to differentiate (1.19) with respect to the i th component of $\mathbf{m}_{-\mathbf{q}}$.

$$\begin{aligned} -\frac{\partial \int d^3r \mathbf{M} \cdot \mathbf{H}_s}{\partial m_{-\mathbf{q}}^i} &= \frac{1}{\alpha} \frac{\partial}{\partial m_{-\mathbf{q}}^i} \sum_{\mathbf{q}} \frac{(\mathbf{m}_{\mathbf{q}} \cdot \mathbf{q})(\mathbf{m}_{-\mathbf{q}} \cdot \mathbf{q})}{|\mathbf{q}|^2} \\ &= \frac{1}{\alpha} \left[\frac{\partial}{\partial m_{-\mathbf{q}}^i} \left(\frac{(\mathbf{m}_{\mathbf{q}} \cdot \mathbf{q})(\mathbf{m}_{-\mathbf{q}} \cdot \mathbf{q})}{|\mathbf{q}|^2} \right) + \frac{\partial}{\partial m_{-\mathbf{q}}^i} \left(\frac{(\mathbf{m}_{-\mathbf{q}} \cdot (-\mathbf{q}))(\mathbf{m}_{\mathbf{q}} \cdot (-\mathbf{q}))}{|-\mathbf{q}|^2} \right) \right] \\ &= \frac{2}{\alpha} \frac{\mathbf{m}_{\mathbf{q}} \cdot \mathbf{q}}{|\mathbf{q}|^2} q^i = \frac{2}{\alpha} h_{s,\mathbf{q}}^i \end{aligned} \quad (1.20)$$

To obtain the right contribution to the free energy, we just need to compensate the additional factor of 2 in our initial formula leading to

$$f_{\text{demagnetization}, \mathbf{k} \neq 0} = \frac{1}{2} \frac{\mu_0}{\alpha} \sum_{\mathbf{q}} \frac{(\mathbf{m}_{\mathbf{q}} \cdot \mathbf{q})(\mathbf{m}_{-\mathbf{q}} \cdot \mathbf{q})}{|\mathbf{q}|^2}$$

Combining the two limits for \mathbf{k} in one result, one can write

$$f_{\text{demagnetization}} = \frac{1}{2} \mathbf{M}_i \chi_{\text{dem}, ij}^{-1} \mathbf{M}_j \quad (1.21)$$

or

$$\tilde{f}_{\text{demagnetization}} = \frac{1}{2} \tilde{\mathbf{M}}_i \chi_{\text{dem}, ij}^{-1} \Big|_{\alpha=1} \tilde{\mathbf{M}}_j \quad (1.22)$$

respectively, with

$$\chi_{\text{dem}, ij}^{-1}(\mathbf{q}) = \frac{\mu_0}{\alpha} \begin{cases} \frac{\mathbf{q}_i \mathbf{q}_j}{|\mathbf{q}|^2} & \text{if } \mathbf{q} \gg 1/L \\ \delta_{ij} N_i & \text{if } \mathbf{q} \ll 1/L \end{cases} \quad (1.23)$$

where L denotes the length scale of the specimen. Plainly speaking, it is necessary for the wavelength of the exciting wave to be much larger than the dimension of the specimen to justify the use of demagnetization factors. Is the wavelength comparable to the length scale of the specimen and hence cannot be seen as a homogeneous excitation any more, one has to resort to the direct dipole-dipole field description.

1.4 Mean-field analysis

1.4.1 The conical phase

The dimensionless free energy G as a function of the magnetic field and temperature is given by

$$e^{-G} = \int \mathcal{D}\mathbf{M} e^{-F[\mathbf{M}]} \quad (1.24)$$

The favored phase is described by a magnetization field, that minimizes the free energy. To prove, that the helical/conical phase represents the global minimum, let us consider a Fourier transformation of $\mathbf{M}(\mathbf{r})$, which is allowed due to translation invariance of (1.6) [32]. Plugging this transformation into the free energy, (1.6) can be written as a sum of a constant term plus several quadratic terms [4]:

$$\begin{aligned} \frac{F_0[\mathbf{M}]}{\kappa} &= -V \frac{t^2 - \mu_0^2 \mathbf{H}^2}{4} + V \sum_{\mathbf{q} \neq 0} \mathbf{m}_{-\mathbf{q}}^\alpha \left[r^{\alpha\beta}(\mathbf{q}) - t \delta^{\alpha\beta} \right] \mathbf{m}_{\mathbf{q}}^\beta \\ &\quad + \int \left(\mathbf{M}^2 + \frac{t}{2} \right)^2 d^3r + V \left(M_0 - \frac{\mu_0 \mathbf{H}}{2} \right)^2 \end{aligned} \quad (1.25)$$

The system volume is given by V and $r^{\alpha\beta} = (1 + t + k^2)\delta^{\alpha\beta} - 2i \epsilon^{\alpha\beta\gamma} k^\gamma$. The Fourier transform of \mathbf{M} is given by

$$\mathbf{M}(\mathbf{r}) = \sum_{\mathbf{q}} \mathbf{m}_{\mathbf{q}} e^{i\mathbf{q}\cdot\mathbf{r}} \quad (1.26)$$

The two terms on the far right in (1.25) are obviously greater or equal to zero. The eigenvalues of the matrix $[r^{\alpha\beta}(\mathbf{q}) - t \delta^{\alpha\beta}]$ are $\{1 + q^2, (1 - q)^2, (1 + q)^2\}$, which makes it positive semi-definite. As a result, the free energy is bounded from below by the constant $-\kappa V(t^2 - \mu_0^2 \mathbf{H}^2)/4$.

To get a first, simple idea of the representation of the structure and parameter relations, let us consider a helical ansatz for the magnetization in the mean-field limit.

$$\mathbf{M}_{hel}(\mathbf{r}) = \begin{pmatrix} A \cos(\mathbf{Q} \cdot \mathbf{r}) \\ A \sin(\mathbf{Q} \cdot \mathbf{r}) \\ M_0 \end{pmatrix} = \begin{pmatrix} A \cos(Q z) \\ A \sin(Q z) \\ M_0 \end{pmatrix} \quad (1.27)$$

We choose here, as a simplification, the propagation direction of the helix $\mathbf{Q} = Q\hat{e}_z$ to be parallel to \hat{e}_z , which in turn is also the direction of a static external magnetic field $\mathbf{H}_0 = \{0, 0, H_z\}$.

Plugging (1.27) into (1.6) minimization with respect to Q , A and M_0 yields the solution:

$$Q = 1 \quad A^2 = -M_0^2 - \frac{t}{2} \quad M_0 = \frac{1}{2}\mu_0 H_z \quad (1.28)$$

One can see, that this solution effectively minimizes the free energy as it puts all quadratic terms of (1.25) simultaneously to zero.

Through a combination of the equations in (1.28) and setting A to zero, one obtains the boundary of the phase transition between the conical and the polarized phase as

$$H_{c2} = \sqrt{-2t}$$

Notably, the zero-field phase transition is at $t = 0$.

In the purely helical phase the homogeneous contribution M_0 vanishes. As explained in subsection 1.3.1, its occurrence of the helical phase even at a finite field is due to additional anisotropy terms, that pin the helix to the underlying atomic lattice and keep it from aligning with the external magnetic field. The here applied theory to describe the helical and conical phases is isotropic. In this setup, the pure helical phase arises only at $\mathbf{H}_0 = 0$, which has to be kept in mind.

Before we go into more detail and study the effect of demagnetization factors in the mean-field limit, it is worthwhile to elaborate on the previous calculation in a new basis, that accommodates the twist in the magnetic structure. While \hat{e}_x , \hat{e}_y and \hat{e}_z are the ordinary cartesian unit vectors, the new basis has the form

$$\hat{e}_z = \hat{e}_z, \quad \hat{e}^\pm = \frac{\hat{e}_x \pm i\hat{e}_y}{\sqrt{2}} \quad \text{or} \quad \hat{e}_x = \frac{\hat{e}^+ + \hat{e}^-}{\sqrt{2}}, \quad \hat{e}_y = \frac{\hat{e}^+ - \hat{e}^-}{i\sqrt{2}} \quad (1.29)$$

We further assume, that the pitch of the helix, as well as the magnetic field, point in \hat{e}_z -direction. In this new basis, we can formulate an ansatz for the magnetization in the mean-field limit as follows.

$$\mathbf{M}_{hel}(\mathbf{r}) = M_0 \hat{e}_z + A \hat{e}^- e^{i\mathbf{Q}\mathbf{r}} + A^* \hat{e}^+ e^{-i\mathbf{Q}\mathbf{r}} \quad (1.30)$$

Here, A is a complex amplitude of the helix and M_0 the homogeneous component in direction of the applied magnetic field. One may note, that this ansatz is still valid even while considering dipole-dipole interaction. Since $\mathbf{q} \parallel \mathbf{M}_{\mathbf{q}}$, no dipole fields arise. Using this ansatz in the free energy

1 Chiral Magnets and their Phases

(1.7), which now only consists of the densities f_0 and $f_{\text{demagnetization}}$ that are defined by (1.6) and (1.14) respectively, we obtain an expression for the energy density $f = f_0 + f_{\text{demagnetization}}$ in terms of the new basis and the rescaled units:

$$f = (t+1) \left(M_0^2 + 2|A|^2 \right) + 2Q^2|A|^2 - 4Q|A|^2 + \left(M_0^2 + 2|A|^2 \right)^2 - \mu_0 H_z M_0 + \frac{1}{2} \frac{\mu_0}{\alpha} \bar{N} M_0^2 \quad (1.31)$$

We have introduced \bar{N} as the demagnetization factor ‘‘pointing along’’ the magnetic field direction $\bar{N} = \hat{H} \cdot \underline{N} \cdot \hat{H}$. Differentiation with respect to Q leads to $Q = 1$, which concurs with our rescaling of units. Minimizing (1.31) with respect to M_0 and A^* gives two equations of states.

$$\left(2(t+1) + \frac{\mu_0}{\alpha} \bar{N} \right) M_0 + 4 \left(M_0^2 + 2|A|^2 \right) M_0 = \mu_0 H_z \quad (1.32a)$$

$$2tA + 4 \left(M_0^2 + 2|A|^2 \right) A = 0 \quad (1.32b)$$

Being in the conical/helical phase implies a finite helix amplitude. Assuming hence a finite A and combining both equations of (1.32) yields an expression for the homogeneous component of the magnetization.

$$M_0 = \frac{\mu_0 H_z}{2 + \frac{\mu_0}{\alpha} \bar{N}} \quad (1.33)$$

It is noteworthy, that M_0 does not depend on temperature to first order, which leads to an also temperature independent susceptibility ($\chi_{\text{con}} = M_0/H_z$) in the conical phase

$$\chi_{\text{con}} = \frac{\mu_0}{2 + \frac{\mu_0}{\alpha} \bar{N}} \quad (1.34)$$

This makes the susceptibility indeed nearly constant in the conical phase, as has been measured by Bauer *et al.* [25]. The measured susceptibility however is expressed by the susceptibility $\tilde{\chi}_{\text{con}}$ calculated analogously in the not rescaled units used of (1.4). The relation amongst each other is given by

$$\tilde{\chi}_{\text{con}} = \frac{1}{\alpha} \chi_{\text{con}}$$

Combining this relation and (1.34) provides us with a concrete value for the thus far unfixed pre-factor α in terms of measurable quantities.

$$\frac{\mu_0}{\alpha} = \frac{2}{\tilde{\chi}_{\text{con}}^{-1} - \bar{N}} \quad (1.35)$$

For the helix amplitude we obtain via (1.32b) and (1.33) the expression

$$|A|^2 = -\frac{t}{4} - \frac{1}{2} \left(\frac{\mu_0 H_z}{2 + \frac{\mu_0}{\alpha} \bar{N}} \right)^2 \quad (1.36)$$

A finite helix amplitude is given as long as H_z is smaller than a critical field H_{c2} , for which the relation

$$0 = -\frac{t}{2} - \left(\frac{\mu_0 H_{c2}}{2 + \frac{\mu_0}{\alpha} \bar{N}} \right)^2 \quad (1.37)$$

holds. The helix amplitude can then also be expressed in terms of the critical field H_{c2}

$$|A|^2 = \frac{\chi_{\text{con}}^2}{2} (H_{c2}^2 - H_z^2) \quad (1.38)$$

1.4.2 The Skyrmion phase

The emergence of Skyrmions came about as part of a non-linear field theory by T.H.R. Skyrme, which unifies mesons (i.e. the nuclear “glue” that holds the nuclei together [36]) and their particle sources. This theory has static solutions of a singular nature, and the number of those entities has been found to be a rigorously conserved constant of motion [37, 2]. Such localized field configurations were long sought after as an ingredient for a general field theory of elementary particles and hence a remarkable accomplishment. Over the years, Skyrmions were discovered in several other fields of research.

In 1989, Bogdanov and Yablonskii already predicted the possible existence of thermodynamically stable vortices, which later turned out to be Skyrmions, as stable ground states in magnetically ordered crystals. The real breakthrough happened around 20 years later, where a lattice Skyrmions were experimentally verified by Mühlbauer *et. al* in MnSi by neutron scattering experiments.

Such a lattice of Skyrmions, can in principle and in lowest order be geometrically constructed by a superposition of three helices, whose propagation direction form angles of 120° amongst each other. For the true lattices, higher modes need to be taken into account as well, which are also evident in experimental results [29]. All (three) of them are orthogonal to the applied magnetic field, so that the lattice plane normal is parallel to it. The resulting texture of the magnetization is depicted in Figure 1.3.

For an elaborate description of the magnetization field for the Skyrmion phase, we start again with the free energy functional (1.6). A valid ansatz consists of generally infinitely many helices pointing in the three \mathbf{Q} -direction shown in Figure 1.9. To first order, three helices suffice, cf. supplementary information of [4].

$$\begin{aligned} M_{sky}(\mathbf{r}) &= M_0 + \sum_{i=1}^{\infty} \left(M_{\mathbf{Q}_i} e^{i\mathbf{Q}_i \cdot \mathbf{r}} + \text{c.c.} \right) \\ &\approx M_0 + \sum_{i=1}^3 |A_i| \left(\hat{n}'_{\mathbf{Q}_i} \cos(\mathbf{Q}_i \cdot \mathbf{r} + \phi_i) - \hat{n}''_{\mathbf{Q}_i} \sin(\mathbf{Q}_i \cdot \mathbf{r} + \phi_i) \right) \end{aligned} \quad (1.39)$$

\mathbf{Q}_1 , \mathbf{Q}_2 and \mathbf{Q}_3 are the wavevectors of the three helices, \mathbf{Q}_i with $i > 3$ denote higher order wave vectors, and

$$M_{\mathbf{Q}_i} = \frac{1}{2} A_i \left(\hat{n}'_{\mathbf{Q}_i} + i \hat{n}''_{\mathbf{Q}_i} \right)$$

where $A_i = |A_i| \exp(i\phi_i)$ is a complex amplitude and $\hat{n}'_{\mathbf{Q}_i}$, $\hat{n}''_{\mathbf{Q}_i}$ are orthogonal vectors. Additionally, minimization of the free energy returns the same chirality for all three helices. This means, that $\hat{n}'_{\mathbf{Q}_i}$, $\hat{n}''_{\mathbf{Q}_i}$ fulfill the relation $\hat{n}'_{\mathbf{Q}_i} \times \hat{n}''_{\mathbf{Q}_i} = \hat{\mathbf{Q}}_i$. Mühlbauer *et al.* [4] show, that after minimization the helices have equal weight, i.e. $|A_1| = |A_2| = |A_3|$, and that the relative phases ϕ_i are fixed in such a way, that at an arbitrary point (say $\mathbf{r} = 0$) the magnetization of each helix points opposite to the field direction, which leads to the center of a Skyrmion being at precisely that point. The previously mentioned angle of 120° between the helices is also a consequence of the minimization process, but can easier be motivated by an analogy to crystal formation out of a liquid phase. Crystal formation is often driven by cubic interactions and can be written in momentum space as

$$\sum_{\mathbf{k}, \mathbf{k}', \mathbf{k}''} \rho_{\mathbf{k}} \rho_{\mathbf{k}'} \rho_{\mathbf{k}''} \delta(\mathbf{k} + \mathbf{k}' + \mathbf{k}'')$$

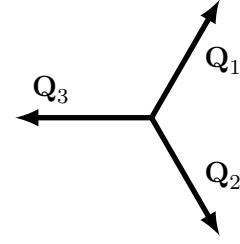


Figure 1.9: The basis vectors of the spin order in the Skyrmion lattice phase.

1 Chiral Magnets and their Phases

If a finite uniform magnetization \mathbf{M}_f is present, a similar mechanism can arise in helical magnets as well. Some of the quartic terms of (1.6) have hence a similar structure and these terms cause a gain in energy, when the momenta form the proclaimed tripod so that the delta function vanishes.

$$\sum_{\mathbf{k}, \mathbf{k}', \mathbf{k}''} (\mathbf{M}_f \cdot \mathbf{M}_{\mathbf{k}})(\mathbf{M}_{\mathbf{k}'} \cdot \mathbf{M}_{\mathbf{k}''})\delta(\mathbf{k} + \mathbf{k}' + \mathbf{k}'')$$

A comparison of the energies between the conical and the Skymion phase is given in section 1.5

Topological aspects

Another prominent feature of Skymions is their topological stability. It has, for instance, played a crucial role in identifying the proper kind of defects that appear in the transition phase between a pure Skymion-tube phase and the conical phase, and hence to the discovery of magnetic monopoles in bulk chiral magnets [9].

While the initial theory by T.H.R. Skyrme considered a three dimensional version of Skymions, the term was later generalized to arbitrary dimensions. Nowadays, the general definition of a Skymion is a smooth, topologically stable field configuration, that has a surjective mapping from real or momentum space to an order parameter space with a non-trivial topology [32].

On the unit sphere, the magnetic structure corresponds to a hedgehog arrangement with all magnetic moments pointing outward. To arrive at a two dimensional representation of the hedgehog structure, one needs to project it onto a plane surface, where the south pole is identified with the origin and the north pole with infinity. To incorporate the chiral nature of the studied materials into the planar structure, combing of the hedgehog in the appropriate direction is required prior to the projection, as is demonstrated in Figure 1.10.

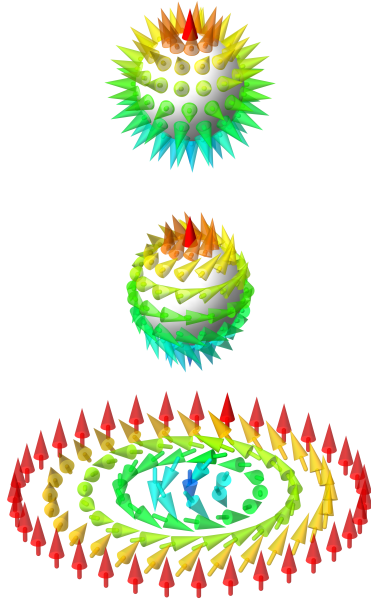


Figure 1.10: The principal on how to obtain a Skymion lattice, as it occurs in chiral magnets, from a hedgehog like spin configuration: From top to bottom: Radially outward pointing spin configuration on the surface of a sphere. Combing this arrangement is necessary to incorporate the chirality of the system. Then, one projects this configuration onto a plane surface, where the south pole is projected to the origin of that surface and the north pole to infinity. The picture is taken from [32].

1.5 Theoretical construction of the phase diagram

The general recipe to obtain an actual phase diagram is to calculate and plot the phases with lowest free energy. The first approach is to consider energies in the mean-field approximation. As it turns out however, the free energy in the mean-field limit of the Skyrmion phase is always higher than the free energy of the conical phase. This does not concur with experimental results. A theoretical explanation for the stabilization of the Skyrmion phase was given by adding Gaussian fluctuations as a first order correction to the mean-field theory [4].

The free energy G is given by (1.24). Let \mathbf{M}^{MF} be the mean-field solution, then additional Gaussian fluctuations around the mean-field lead to

$$\mathbf{G} \approx F[\mathbf{M}^{MF}] + \frac{1}{2} \log \det \left(\frac{\delta^2 F}{\delta \mathbf{M} \delta \mathbf{M}} \right) \Big|_{\mathbf{M}^{MF}} \quad (1.40)$$

This procedure explains in the end only the existence but not the extent of a stable Skyrmion phase as it covers only thermal fluctuations to a Gaussian level around the mean-field theory. A more elaborate approach to the phase diagram has been made by Buhrandt and Fritz [38], namely a classical Monte Carlo study, which incorporates fluctuations of the system in a non-perturbative manner. Taking anisotropy compensation and finite size effects into account, their calculations yield a phase diagram (Figure 1.11) in excellent agreement with experiments on MnSi.

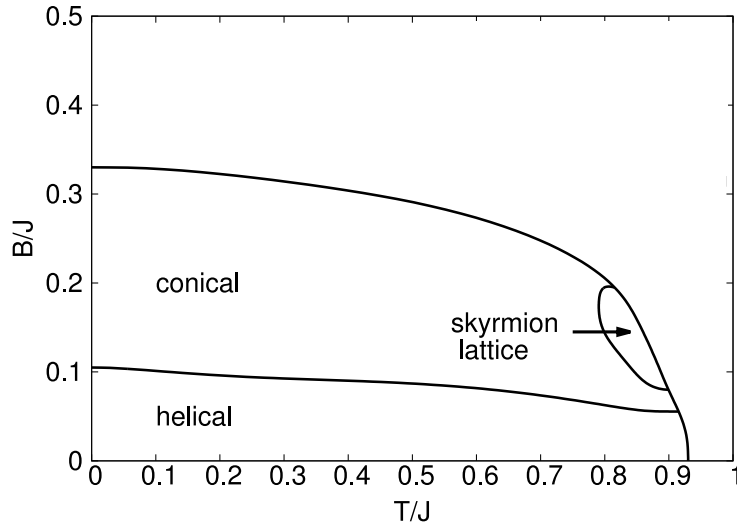


Figure 1.11: Phase diagram as a result of a classical Monte Carlo simulation. Temperature and magnetic field are gauged to the ferromagnetic exchange J [38].

Excitations and Linear Response Dynamics

CONDENSED MATTER EXPERIMENTS typically probe the response of a system to weak perturbations. If the perturbation is weak enough, the response will bear a linear character. As this is the case for the here studied experiments, we can focus on perturbations to first order only. We will use this chapter to give an explanation on how to calculate resonance frequencies as a response to weak magnetic or electric field oscillations. A large portion is dedicated to the numerical implementation.

First however, we give a short introduction on simple wave motions in a ferromagnet as a preparation for the more elaborate calculations later on. We conclude that part with magnon and helimagnon dispersion relations, as well as a brief introduction of the concept of resonance.

2.1 Spin waves

To get familiar with the idea of spin waves and ultimately their measurement via resonance experiments, it is instructive to study an ordinary ferromagnet without all the additional effects like demagnetization fields etc. This is the focus of this section.

Below the critical Curie temperature, a ferromagnet orders magnetically. The internal magnetic moments align in a certain direction given by magnetic anisotropies or an external magnetic field, and form a joint spontaneous magnetization. The latter takes its maximum at zero temperature. In other words, the individual electron spins add up to a maximum spin S .

When temperature rises, thermal fluctuations lead to a change of the total spin, effectively in its lowering. This could already be achieved for example by flipping one spin. This procedure, however, would result in a state, that is not an eigenstate of the hamiltonian of the problem. This hamiltonian consists of the exchange energy and a Zeeman contribution, where the spins couple to the effective, internal magnetic field, which includes a possible external field as well as any molecular field.

But a change of the total spin could also be achieved by an even distribution of the excitation energy onto the entire system, so that every spin is changed a little bit instead of completely flipping one single spin. In such a collective excitation, the movement of neighboring spins are coupled together and form so-called spin waves or speaking in terms of quasiparticles excitations: magnons.

Their creation and behavior is closely related to phonon excitations in a solid, but they do have a different dispersion relation (cf. subsection 2.1.2).

2.1.1 Precession of magnetic moments in a magnetic field

The magnetic object of interest is subject to a homogeneous magnetic field \mathbf{H}_0 . The magnet contains electrons, that carry a spin of $\frac{1}{2}$. More generally, it suffices to consider charged particles with a general angular momentum \mathbf{J} that induce a magnetic moment \mathbf{m} parallel to \mathbf{J} .

$$\mathbf{m} = \gamma \mathbf{J}$$

The proportionality constant $\gamma = \frac{g_L \mu}{\hbar} = \frac{g_L q}{2m}$ is called the gyromagnetic ratio. Here, g_L is the Landé factor and $\mu = \frac{q\hbar}{2m}$ the magneton for a particle with charge q and mass m . Hence for an electron we get $\gamma = -\frac{g_L e}{2m_e}$ with $-e < 0$ the charge of the electron and m_e its mass.

Obviously, this setup leads to some form of interaction between the internal magnetic moments and the external magnetic field. The energy density connected to said coupling is

$$U = -\mu_0 \mathbf{m} \cdot \mathbf{H}_0 \quad (2.1)$$

Let us consider a fixed direction of the outer magnetic field, $\mathbf{H}_0 = H_0 \hat{e}_z$. The interaction energy density then only depends on the z-component of the angular momentum:

$$U = -\mu_0 m_z H_0 = -\gamma \mu_0 H_0 J_z$$

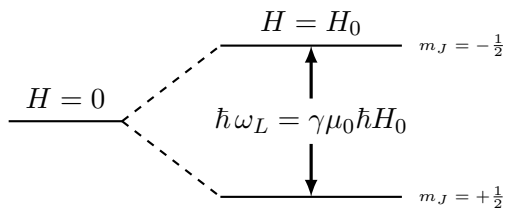


Figure 2.1: Level splitting due to the Zeeman effect in a finite magnetic field.

In the case of itinerant electrons, we can neglect the orbital angular momentum part, so that $J_z = S_z = \pm\frac{1}{2}$. As a consequence of a finite, external magnetic field, the energy (2.1) has to be taken into account and the formerly degenerate energy splits into two possible levels as can be seen in Figure 2.1. The m_J stand for the possible quantum numbers of J_z .

Between these two levels, the energy difference scales linear in the magnetic field, which leads to the fundamental condition for the magnetic resonance absorption [39, pp. 528]:

$$\omega_L = \gamma \mu_0 H_0 \quad (2.2)$$

The resonance frequency ω_L is called Larmor-frequency. To get an impression of what is actually going on in the crystal, let us now consider the Heisenberg equation of motion for spins $\frac{d}{dt} \mathbf{S} = \frac{1}{i\hbar} [\mathbf{S}, \mathcal{H}]$. For \mathcal{H} we take the interaction energy (2.1) from above with the magnetic moment now being just a single spin. Using the commutation relations for spins $\frac{1}{i\hbar} [\mathbf{S}_i, \mathbf{S}_j] = \epsilon_{ijk} \mathbf{S}_k$ leads to

$$\frac{d}{dt} \mathbf{S} = \frac{1}{i\hbar} [\mathbf{S}, -\gamma \mu_0 \mathbf{S} \cdot \mathbf{H}_0] = \gamma \mu_0 \mathbf{S} \times \mathbf{H}_0 \quad (2.3)$$

This equation describes the precession of the spin \mathbf{S} around the static field \mathbf{H}_0 .

An analog in the macroscopic world can be drawn, if one sees that a macroscopic magnetization is the sum over all microscopic magnetic moments, in this case spins $\mathbf{M} = \sum_i \mathbf{m}_i$. This approach yields an expression, which describes a precession of the macroscopic magnetization around the applied magnetic field (see Figure 2.2) [39].

$$\boxed{\frac{d\mathbf{M}}{dt} = \gamma \mu_0 \mathbf{M} \times \mathbf{H}_0} \quad (2.4)$$

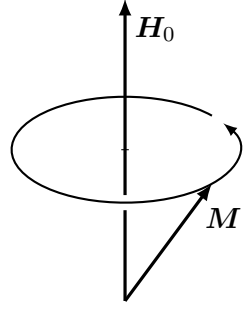


Figure 2.2: Precession of a magnetization \mathbf{M} around a static magnetic field \mathbf{H}_0 , cf. (2.4).

2.1.2 Dispersion relation

The next step to a detailed description of spin waves lies in obtaining their dispersion relation. In its derivation we follow [40]. To derive the relation, we take the exchange energy (1.1) with $J_{ij} = J > 0$ and summation only over nearest neighbors, as well as the Zeeman term (2.1) as the free energy F for our model. Let us have a look at a setup with equal atoms at each site. For site a of the lattice, with nearest neighbors j and the use of magnetic moments $\mathbf{m}_a = \mathbf{S}_a/\gamma$ instead of spins, then applies

$$F = -J \sum_{\langle j \rangle_a} \mathbf{S}_a \cdot \mathbf{S}_j - \mathbf{m}_a \cdot \mathbf{H} = -\frac{J}{\gamma^2} \sum_{\langle j \rangle_a} \mathbf{m}_a \cdot \mathbf{m}_j - \mathbf{m}_a \cdot \mathbf{H} \quad (2.5)$$

The summation over $\langle j \rangle_a$ denotes the summation over all sites j , that are nearest neighbors to a . The effective magnetic field is given via $\mu_0 \mathbf{H}^{eff} = -\frac{\partial F}{\partial \mathbf{m}_a}$. Applying this to (2.5) yields

$$\mathbf{H}^{eff} = \mathbf{H} + \frac{J}{\gamma^2} \sum_{\langle j \rangle_a} \mathbf{m}_j$$

Plugging this field into the precession equation (2.4) gives us the equation of motion for the magnetic moment on site a .

$$\frac{d\mathbf{m}_a}{dt} = \gamma \mu_0 \mathbf{m}_a \times \mathbf{H} + \mathbf{m}_a \times \frac{J}{\gamma \mu_0} \sum_{\langle j \rangle_a} \mathbf{m}_j \quad (2.6)$$

To simplify this equation further, let us make the following approximations: $\mathbf{H} = \mathbf{H}_0 \parallel \hat{\mathbf{e}}_z$, i.e. $H_x = H_y = 0$, and $m_x, m_y \ll m_z$ and therefore $m_z \approx M_0$. With the last assumption at hand, we can neglect terms of the sort $m_x m_y$ or of similar quadratic order. Equations for the individual components are now

$$\begin{aligned} \frac{dm_{a,x}}{dt} &= \gamma \mu_0 m_{a,y} H_0 + \frac{J}{\gamma} \left(m_{a,y} \sum_{\langle j \rangle_a} m_{j,z} - m_{a,z} \sum_{\langle j \rangle_a} m_{j,y} \right) \\ &= \gamma \mu_0 m_{a,y} H_0 + \frac{JM_0}{\gamma} \left(\bar{n} m_{a,y} - \sum_{\langle j \rangle_a} m_{j,y} \right) \end{aligned} \quad (2.7a)$$

$$\frac{dm_{a,y}}{dt} = -\gamma \mu_0 m_{a,x} H_0 - \frac{JM_0}{\gamma} \left(\bar{n} m_{a,x} - \sum_{\langle j \rangle_a} m_{j,x} \right) \quad (2.7b)$$

$$\frac{dm_{a,z}}{dt} \approx 0 \quad (2.7c)$$

2 Excitations and Linear Response Dynamics

The number of nearest neighbors to the site a is introduced above as \bar{n} . We now make the following ansatz of a Fourier representation for the magnetic moments

$$\begin{aligned} m_{a,x} &= M_x e^{i(\mathbf{k} \cdot \mathbf{r}_a - \omega t)} \\ m_{a,y} &= M_y e^{i(\mathbf{k} \cdot \mathbf{r}_a - \omega t)} \end{aligned} \quad (2.8)$$

where \mathbf{r}_a points to the a th site. Plugging it into (2.7a) leads to

$$\begin{aligned} -i\omega M_x e^{i(\mathbf{k} \cdot \mathbf{r}_a - \omega t)} &= \gamma\mu_0 M_y H_0 e^{i(\mathbf{k} \cdot \mathbf{r}_a - \omega t)} + \frac{JM_0}{\gamma} \left(\bar{n} M_y e^{i(\mathbf{k} \cdot \mathbf{r}_a - \omega t)} - \sum_{\langle j \rangle_a} M_y e^{i(\mathbf{k} \cdot \mathbf{r}_j - \omega t)} \right) \\ -i\omega M_x &= \gamma\mu_0 M_y H_0 + \frac{JM_0}{\gamma} \left(\bar{n} M_y - \sum_{\langle j \rangle_a} M_y e^{i\mathbf{k} \cdot (\mathbf{r}_j - \mathbf{r}_a)} \right) \\ 0 &= i\omega M_x + M_y \left[\gamma\mu_0 H_0 + \frac{JM_0}{\gamma} \left(\bar{n} - \sum_{\langle j \rangle_a} e^{i\mathbf{k} \cdot (\mathbf{r}_j - \mathbf{r}_a)} \right) \right] \\ 0 &= i\omega M_x + M_y \left[\gamma\mu_0 H_0 + \frac{JM_0}{\gamma} \left(\bar{n} - \sum_{\langle j \rangle_a} \cos(\mathbf{k} \cdot (\mathbf{r}_j - \mathbf{r}_a)) \right) \right] \\ 0 &= i\omega M_x + M_y \underbrace{\left[\gamma\mu_0 H_0 + \frac{JM_0}{\gamma} \sum_j (1 - \cos(\mathbf{k} \cdot \tilde{\mathbf{r}}_j)) \right]}_{:=\beta} \end{aligned}$$

In the penultimate line, we have assumed, that the lattice is periodic, so that one can always find pairs \mathbf{r}_i and \mathbf{r}_j within the set of nearest neighbors to site a , on whose connecting line the midpoint is equal to \mathbf{r}_a .

$$\mathbf{r}_a = \frac{\mathbf{r}_i - \mathbf{r}_j}{2}$$

That way, the two terms for the opposing sites form a cosine. In the last line, $\tilde{\mathbf{r}}_j$ is the vector connecting the center site a to the neighbor j . It therefore has the length of the lattice constant. Along the lines of this calculation, we get a similar equation for (2.7b) and in total the set

$$\begin{aligned} 0 &= i\omega M_x + \beta M_y \\ 0 &= i\omega M_y - \beta M_x \end{aligned} \quad (2.9)$$

Solving this set of equations for a finite magnetization provides us with the sought after spin wave dispersion relation (cf. [40]).

$$\boxed{\omega = \beta = \gamma\mu_0 H_0 + \frac{JM_0}{\gamma} \sum_j (1 - \cos(\mathbf{k} \cdot \tilde{\mathbf{r}}_j))} \quad (2.10)$$

For $\mathbf{k} = 0$ and in a finite and homogeneous external field H_0 , all magnetic moments are aligned in parallel, and precess around \mathbf{H}_0 according to (2.4). As previously mentioned, the rotation frequency is the Larmor-frequency, or as we have now calculated, the first term of the dispersion relation.

Without the presence of the external magnetic field, a typical \mathbf{k} dependence is shown in Figure 2.3.

To simplify things, an equal distance between all atoms \tilde{r} was assumed. For a small k , i.e. $k\tilde{r} \ll 1$, the dispersion relation is quadratic in k .

$$\omega = \frac{JM_0\tilde{r}^2}{2\gamma}k^2$$

This is a noticeable difference to phonons, whose dispersion relation goes linear in k around $k = 0$. Also in an anti-ferromagnet, the dispersion relation would be linear in \mathbf{k} .

Going a step further is to calculate the dispersion relation of so-called helimagnons for a helical state, which has been done by Belitz *et al.* [41]. They show, that the helimagnon dispersion relation is highly anisotropic. The mode is softer in the direction perpendicular to the wave vector than in the longitudinal direction.

$$\omega \propto \sqrt{c_{\parallel}k_{\parallel}^2 + c_{\perp}k_{\perp}^4} \quad (2.11)$$

This means a linear dispersion relation for wave vectors parallel to the pitch vector, and quadratic one for wave vectors orthogonal to it. The coefficients c_{\parallel} and c_{\perp} are constants. For further discussion and numerical calculations of the dispersion relation of Skyrmions, we refer to subsection 3.3.2.

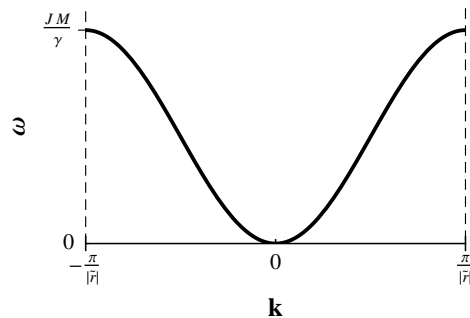


Figure 2.3: Dispersion relation of spin-waves in a one dimensional chain. $|\tilde{\mathbf{r}}|$ is the distance between neighboring sites.

2.2 Resonance

Atomic magnetic moments are associated with an angular momentum, as we have seen in the previous section. As a consequence, the change of an applied field does not lead to an instantaneous rotation of the magnetization vector to the new equilibrium direction or even a delayed following, but to a precession around it. Due to damping caused by dissipative processes, the precession motion loses energy and the new equilibrium position will be reached eventually [35].

If the system were in equilibrium, the application of a small oscillating field perpendicular to the initial equilibrium direction, will hence not lead to a pendulum like movement of the magnetization, but to a forced precession around the equilibrium direction. These dynamical effects gain importance for the three materials, which were introduced in the first chapter, especially at radio and microwave frequencies, because their natural frequencies are of the same order of magnitude. Our focus lies on the response of the system to external field oscillations. Resonance comes about, when the oscillation frequency ω of the external magnetic field coincides with one of the eigenfrequencies, say ω_0 , of the magnet. Then, the oscillation amplitude $A(\omega)$ is largest and also the energy taken from the external oscillation reaches its

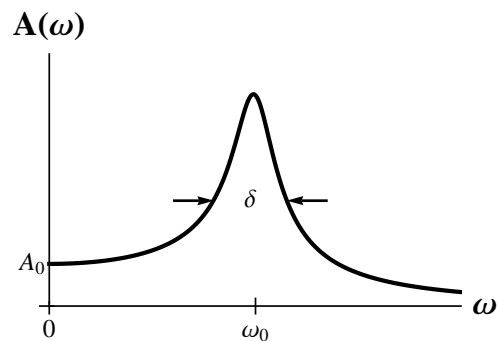


Figure 2.4: Schematic picture of the resonating amplitude of an oscillator with eigenfrequency ω_0 depending on the excitation frequency ω $A(\omega) = A_0/\sqrt{(\omega_0^2 - \omega^2)^2 + (2\delta\omega)^2}$, where δ is some damping coefficient.

maximum, as can be seen in absorption spectroscopy.

A typical resonance spectrum of a damped harmonic oscillator is shown in Figure 2.4 and has a Lorentzian shape.

2.3 General derivation of the resonance frequencies

In this part, we introduce the so far disregarded time dependent contributions to the free energy functional. Schematically, we can split the free energy functional into a time independent part F_{stat} and a time dependent part $F(t)$.

$$F = F_{stat} + F(t)$$

The time dependent part obviously comprises the oscillating electric or magnetic fields, whose energies we regard as small quantities compared to the static terms, while F_{stat} contains f_0 , $f_{\text{demagnetization}}$ and in principle also $f_{\text{anisotropy}}$ of (1.7). We are interested in the response of the magnetization to the time dependence of the external field oscillation. To this end, we see the time dependent deviations from the equilibrium mean-field solution \mathbf{M}^{MF} as a small quantity, too.

$$\mathbf{M} = \mathbf{M}^{MF} + \delta\mathbf{M}(t) \quad (2.12)$$

Sought-after is therefore a linear relation between $\delta\mathbf{M}$ at a time t due to the oscillating field at time t' , and the oscillating field itself. It may be noted here, that the system is not explicitly time dependent so that the response will hence just depend on the difference $t - t'$. Fourier transformation with respect to time will yield the important statement within the linear response regime, that a perturbation acting at a frequency ω will result in a response of the same frequency [42]. Strictly speaking, the excitation is not necessarily confined to be homogeneous in space. Therefore, we make an ansatz for the oscillations with not only a time dependance, but a spacial variation as well:

$$F(t, \mathbf{r}) = \bar{F} e^{-i(\omega t + \mathbf{q} \cdot \mathbf{r})} \quad (2.13a)$$

$$\delta\mathbf{M}(t, \mathbf{r}) = \delta\mathbf{M} e^{-i(\omega t + \mathbf{q} \cdot \mathbf{r})} \quad (2.13b)$$

Due to the translation invariance of the system, the upper statement for the response in time applies to the spatial oscillation in a similar fashion. Since we are dealing with a discrete translation symmetry, the momenta of the excitation and the response only coincide up to a reciprocal lattice vector.

Using this ansatz in the precession equation (2.4) lets us obtain a general scheme to calculate resonances of our system. \mathbf{H}^{eff} now contains both the static and oscillating outer fields.

$$\partial_t \mathbf{M} = \gamma \mu_0 \mathbf{M} \times \mathbf{H}^{eff} = -\gamma \mathbf{M} \times \frac{\delta F}{\delta \mathbf{M}} = -\gamma \mathbf{M} \times \left(\frac{\delta F_{stat}}{\delta \mathbf{M}} + \frac{\delta F(t, \mathbf{r})}{\delta \mathbf{M}} \right) \quad (2.14)$$

Expansion of F_{stat} to quadratic order in $\delta\mathbf{M}(t, \mathbf{r})$ gives

$$F_{stat}[\mathbf{M}] = F_{stat}[\mathbf{M}^{MF}] + 0 \cdot \delta\mathbf{M}(t, \mathbf{r}) + \frac{1}{2} \delta\mathbf{M}(t, \mathbf{r}) \frac{\delta^2 F_{stat}}{\delta \mathbf{M}^2} \Big|_{\mathbf{M}^{MF}} \delta\mathbf{M}(t, \mathbf{r}) + \mathcal{O}(\delta\mathbf{M}(t)^3) \quad (2.15)$$

Here, we utilized the mean-field condition $\frac{\delta F_{stat}}{\delta \mathbf{M}} \Big|_{\mathbf{M}=\mathbf{M}^{MF}} = 0$. The next step is to plug this expansion into (2.14). In doing so, we only keep terms to linear order in $\delta\mathbf{M}$ and \bar{F} . Furthermore,

$\partial_t \mathbf{M}^{MF} = 0$ and use of the explicit time dependencies of $\delta \mathbf{M}$ lead to

$$-i\omega \delta \mathbf{M} = -\gamma \left(\mathbf{M}^{MF} \times \frac{\delta^2 F_{stat}}{\delta \mathbf{M}^2} \Big|_{\mathbf{M}^{MF}} \delta \mathbf{M} + \mathbf{M}^{MF} \times \frac{\delta \tilde{F}}{\delta \mathbf{M}} \Big|_{\mathbf{M}^{MF}} \right) \quad (2.16)$$

$$\delta \mathbf{M} = - \left[i\omega - \gamma \mathbf{M}^{MF} \times \frac{\delta^2 F_{stat}}{\delta \mathbf{M}^2} \Big|_{\mathbf{M}^{MF}} \right]^{-1} \cdot \left(\gamma \mathbf{M}^{MF} \times \frac{\delta \tilde{F}}{\delta \mathbf{M}} \Big|_{\mathbf{M}^{MF}} \right) \quad (2.17)$$

$$\curvearrowright \omega_{\text{resonance}} = \text{Im Eigenvalues} \left[\gamma \mathbf{M}^{MF} \times \frac{\delta^2 F_{stat}}{\delta \mathbf{M}^2} \Big|_{\mathbf{M}^{MF}} \right] \quad (2.18)$$

Here, we have used the definition for the effective magnetic field $\mu_0 \mathbf{H}^{eff} = -\frac{\delta F}{\delta \mathbf{M}}$. The last line comes about, because the variation of $\delta \mathbf{M}$ is maximal, if the denominator of the penultimate line is zero.

2.4 Momentum space calculations for numerical purposes

For numerical purposes, we switch to a representation in momentum space of the precession equation. For periodic structures like in the conical and Skyrmion phase, it is possible to decompose the continuous momentum vector \mathbf{q} into a reciprocal lattice vector, i.e. a discrete part, which also functions as a Brillouin-zone index, and a continuous part, which is restricted to the first Brillouin zone. Thereby $\mathbf{q} = \mathbf{Q} + \mathbf{k}$ with \mathbf{Q} being the discrete reciprocal lattice vector and $\mathbf{k} \in 1.\text{BZ}$ continuous. The reciprocal lattice in the conical phase is one dimensional, while the reciprocal lattice of the Skyrmion phase is two dimensional. They are both shown in Figure 2.5.

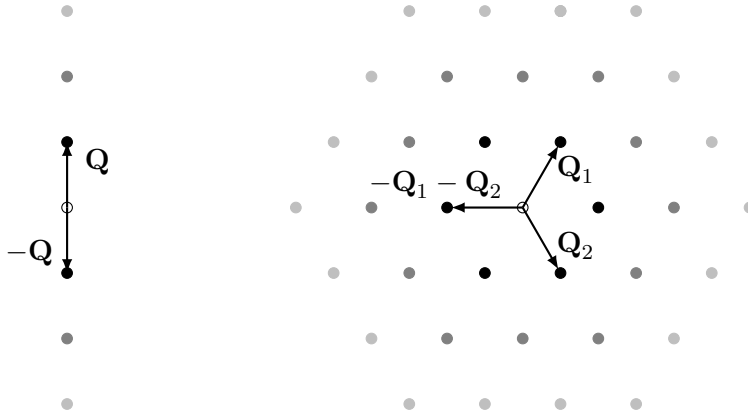


Figure 2.5: Image of the reciprocal lattice in the conical (left) and Skyrmion phase (right). The latter is spanned by the two vectors \mathbf{Q}_1 and \mathbf{Q}_2 . Black solid dots define the first ring, gray ones the second ring, light gray ones the third and so forth.

We have chosen the following convention for the vectorial structure for the conical phase in momentum space.

$$\mathbf{M}_{\text{con}}(\mathbf{q}) = \left\{ M_0^x, M_0^y, M_0^z; M_{\mathbf{Q}}^x, M_{\mathbf{Q}}^y, M_{\mathbf{Q}}^z; M_{-\mathbf{Q}}^x, M_{-\mathbf{Q}}^y, M_{-\mathbf{Q}}^z; \dots \right\}(\mathbf{k}) \quad (2.19)$$

$$=: \{ M_0, M_{\mathbf{Q}}, M_{-\mathbf{Q}}, M_{2\mathbf{Q}}, M_{-2\mathbf{Q}}, \dots \}(\mathbf{k}) \quad (2.20)$$

Analogous for the Skyrmion phase

$$\mathbf{M}_{\text{sky}}(\mathbf{q}) = \left\{ M_0, M_{\mathbf{Q}_1}, M_{-\mathbf{Q}_1}, M_{\mathbf{Q}_2}, M_{-\mathbf{Q}_2}, M_{\mathbf{Q}_1+\mathbf{Q}_2}, M_{-\mathbf{Q}_1-\mathbf{Q}_2}, M_{2\mathbf{Q}_1}, M_{-2\mathbf{Q}_1}, \dots \right\}(\mathbf{k}) \quad (2.21)$$

2 Excitations and Linear Response Dynamics

Before dealing with the entire equation, we have a look at individual parts.

The Fourier transform of the fluctuation matrix $\left. \frac{\delta^2 F}{\delta \mathbf{M}^2} \right|_{\mathbf{M}^{MF}}$ is given by (cf. supplementary information of [4])

$$\begin{aligned} \frac{\delta^2 F}{\delta M^i(-\mathbf{q}) \delta M^j(\mathbf{q}')} &= 2 g_{\mathbf{q}\mathbf{q}'}^{ij} = 2 g_{\mathbf{Q}\mathbf{Q}'}^{ij}(\mathbf{k}, \mathbf{k}') \\ &\quad \begin{array}{l} \mathbf{q} = \mathbf{Q} + \mathbf{k} \\ \mathbf{q}' = \mathbf{Q}' + \mathbf{k}' \\ \mathbf{k}, \mathbf{k}' \in 1.BZ \end{array} \\ &= \gamma \left[\delta_{\mathbf{k}\mathbf{k}'} \delta_{\mathbf{Q}\mathbf{Q}'} r^{ij}(\mathbf{Q} + \mathbf{k}) + 2 \delta^{ij} \sum_{\mathbf{Q}''} M_{-\mathbf{Q}''} \cdot M_{\mathbf{Q}-\mathbf{Q}'+\mathbf{Q}''} \delta_{\mathbf{k},\mathbf{k}'} + 4 \sum_{\mathbf{Q}''} M_{-\mathbf{Q}''}^i M_{\mathbf{Q}-\mathbf{Q}'+\mathbf{Q}''}^j \delta_{\mathbf{k}\mathbf{k}'} \right] \\ &= 2 g_{\mathbf{Q}\mathbf{Q}'}^{ij}(\mathbf{k}) \delta_{\mathbf{k}\mathbf{k}'} \quad (2.22) \end{aligned}$$

with $r^{ij}(\mathbf{q}) = (1 + t + \mathbf{q}^2) \delta^{ij} - 2i \epsilon^{ijk} q^k + D^{ij}(\mathbf{q})$ where $D^{ij}(\mathbf{q})$ is an additional term representing the demagnetization field contributions:

$$D^{ij}(\mathbf{q}) = \frac{1}{2} \frac{\mu_0}{\alpha} \begin{cases} \frac{N \delta^{ij}}{|\mathbf{q}|^2} & , \mathbf{q} = 0 \\ \frac{q^i q^j}{|\mathbf{q}|^2} & , \mathbf{q} \neq 0 \end{cases} \quad (2.23)$$

This scheme can also be applied to the effective magnetic field ¹

$$\begin{aligned} \mu_0 (H^{eff})^i(\mathbf{q}) &= \mu_0 (H^{eff})^i_{\mathbf{Q}}(\mathbf{k}) = - \sum_{\mathbf{q}'} \frac{\delta^2 F}{\delta M^i(-\mathbf{q}) \delta M^j(\mathbf{q}')} \delta M^j(\mathbf{q}') - \frac{\delta F(t, \mathbf{q})}{\delta M^i(\mathbf{q})} \\ &= - \sum_{\mathbf{q}'} 2 g_{\mathbf{q}\mathbf{q}'}^{ij} \delta M^j(\mathbf{q}') = -2 \sum_{\mathbf{Q}'\mathbf{k}'} g_{\mathbf{Q}\mathbf{Q}'}^{ij}(\mathbf{k}) \delta_{\mathbf{k}\mathbf{k}'} M_{\mathbf{Q}'}^j(\mathbf{k}') - \frac{\delta F(t, \mathbf{k})}{\delta M_{\mathbf{Q}}^i(\mathbf{k})} \\ &= -2 \sum_{\mathbf{Q}'} g_{\mathbf{Q}\mathbf{Q}'}^{ij}(\mathbf{k}) \delta M_{\mathbf{Q}'}^j(\mathbf{k}) - \frac{\delta F(t, \mathbf{k})}{\delta M_{\mathbf{Q}}^i(\mathbf{k})} \end{aligned} \quad (2.24)$$

Now, we can begin with our calculation in Fourier space. Doing the Fourier transform in space via $\mathbf{M}(\mathbf{r}) = \sum_{\mathbf{q}} \mathbf{M}_{\mathbf{q}} e^{i\mathbf{q}\cdot\mathbf{r}}$ yields the following expression for (2.14).

$$\begin{aligned} \partial_t \delta M^i(\mathbf{q}) &= \partial_t \delta M_{\mathbf{Q}}^i(\mathbf{k}) = \gamma \mu_0 \sum_{\mathbf{Q}'} \epsilon^{ijl} M_{\mathbf{Q}'}^j (H^{eff})_{\mathbf{Q}''}^l(\mathbf{k}) \delta_{\mathbf{Q}'+\mathbf{Q}''-\mathbf{Q}} \\ &= -\gamma \mu_0 \left(\sum_{\mathbf{Q}'} \epsilon^{ijl} M_{\mathbf{Q}'}^j \delta_{\mathbf{Q}'+\mathbf{Q}''-\mathbf{Q}} \right) \left(-(H^{eff})_{\mathbf{Q}''}^l(\mathbf{k}) \right) \\ &= -\gamma \underbrace{\left(\sum_{\mathbf{Q}'} \epsilon^{ijl} M_{\mathbf{Q}'}^j \delta_{\mathbf{Q}'+\mathbf{Q}''-\mathbf{Q}} \right)}_{=:(M \times)_{\mathbf{Q}\mathbf{Q}''}^{il}} \sum_{\mathbf{Q}''} \left(2 g_{\mathbf{Q}''\mathbf{Q}''}^{lb}(\mathbf{p}) \delta M_{\mathbf{Q}''}^b(\mathbf{k}) + \frac{\delta F(t, \mathbf{k})}{\delta M_{\mathbf{Q}}^i(\mathbf{k})} \right) \end{aligned} \quad (2.25)$$

$(M \times)_{\mathbf{Q}\mathbf{Q}''}^{il}$ is skew-hermitian (anti-hermitian) due to the anti-symmetric epsilon tensor and has therefore purely imaginary eigenvalues. Following the steps in section 2.3 to arrive at (2.17) gives

$$-i\omega \delta M_{\mathbf{Q}}^i(\mathbf{k}) = -\gamma \left((M^{MF} \times)_{\mathbf{Q}\mathbf{Q}''}^{il} \right) \left(2 g_{\mathbf{Q}''\mathbf{Q}''}^{lb}(\mathbf{k}) \right) \delta M_{\mathbf{Q}''}^b(\mathbf{k}) + \left((M^{MF} \times)_{\mathbf{Q}\mathbf{Q}''}^{in} \right) \xi_{\mathbf{Q}''}^n \quad (2.26)$$

¹The general structure is $\mu_0 \mathbf{H}^{eff} = -\frac{\delta F}{\delta \mathbf{M}} \approx -\frac{\delta^2 F}{\delta \mathbf{M}^2} \delta \mathbf{M}$ and the pair of \mathbf{M} in the denominator are arranged in a $\mathbf{M}(-\mathbf{q})\mathbf{M}(\mathbf{q})$ fashion due to momentum conservation. Hence, the structure of $\frac{\delta^2 F}{\delta \mathbf{M}^2}$ is $\frac{\delta^2 F}{\delta \mathbf{M}(-\mathbf{q}) \delta \mathbf{M}(\mathbf{q})}$

where

$$\xi_{\mathbf{Q}''}^n = - \left(\frac{\delta \tilde{F}}{\delta \mathbf{M}} \Big|_{\mathbf{M}^{MF}} \right)_{\mathbf{Q}''}^n \quad (2.27)$$

contains the direction and strength of the oscillating field coupling to the magnetization, either magnetic or electric. We elaborate on both cases in separate chapters. Again, taking steps analogous to the schematic calculation for (2.18), we arrive at

$$\delta M_{\mathbf{Q}''}^b = - \left[i\omega \delta^{ib} \delta_{\mathbf{Q}\mathbf{Q}''} - \gamma ((M^{MF} \times)_{\mathbf{Q}\mathbf{Q}''}^{il}) (2g_{\mathbf{Q}''\mathbf{Q}''}^{lb}(\mathbf{k})) \right]^{-1} ((M^{MF} \times)_{\mathbf{Q}\mathbf{Q}''}^{in}) \xi_{\mathbf{Q}''}^n \quad (2.28)$$

In principle, the sums extend over infinitely many \mathbf{Q} -vectors. Numerically, a cutoff Λ has to be chosen with $|\mathbf{Q}| \leq \Lambda$. This is valid since the free energy approaches a finite limit in the mean-field limit plus Gaussian fluctuations for $\Lambda \rightarrow \infty$ [4].

The numerical challenge is to include as many \mathbf{Q} -vectors in the calculations as possible, especially in the Skyrmion phase calculations. There, we achieve to include up to five rings. A definition of *rings* is given in Figure 2.5. A pretty good convergence of the resonance frequencies is found to happen already by including four rings.

2.5 Resonance frequencies and their weights

Usually, resonance peaks have a Lorentz-peak structure as has been explained in section 2.2. Since we do not consider damping terms in our calculation, the obtained peak structure is a delta peak and the weight is hence not given via the area taken by the resonance peak. One can however take the pre-factor of the delta peak of the resonance condition (2.17) as a weight. In a schematic sketch, the equation in momentum space has the structure

$$\delta \mathbf{M}_\alpha(\omega) = - [i\omega \mathbf{1} - R]_{\alpha\beta}^{-1} T_\beta \quad (2.29)$$

where the matrix $R = \left(\gamma \mathbf{M}^{MF} \times \frac{\delta F_0^2}{\delta \mathbf{M}^2} \Big|_{\mathbf{M}^{MF}} \right)$ and the vector $\mathbf{T} = \left(\gamma \mathbf{M}^{MF} \times \frac{\delta \tilde{F}}{\delta \mathbf{M}} \Big|_{\mathbf{M}^{MF}} \right)$. The indices α and β run over all individual components of for example the generally infinite vector (2.19). To accommodate the same momentum structure, the matrices are constructed accordingly as has been shown in the section above.

To “purify” the denominator of (2.29), we perform an eigenbasis decomposition of R into a diagonal part R' , whose diagonal elements consist of the eigenvalues of R , and matrices P and P' , that consist of the corresponding eigenvectors.

$$\delta \mathbf{M}_i(\omega) = [i\omega \mathbf{1} - PR'P^{-1}]_{\alpha\beta}^{-1} T_\beta = P_{\alpha\eta} [i\omega \mathbf{1} - R']_{\eta\eta}^{-1} P_{\eta\beta}^{-1} T_\beta$$

The matrix $[i\omega \mathbf{1} - R']^{-1}$ has diagonal form and its diagonal elements can be written as

$$[i\omega \mathbf{1} - R']_{\eta\eta}^{-1} = \frac{\hat{e}_\eta \hat{e}_\eta^T}{i\omega - R'_\eta} \quad (2.30)$$

Letting \hat{e}_η (\hat{e}_η^T) act to the left (right) will select the appropriate components of P (P^{-1}), which belong to the η th eigenvalue of R' . To obtain the weight of the resonance for a specific ω_n belonging to the n th eigenvalue of R' , one then needs to project $\delta \mathbf{M}$ onto the direction of probing \hat{e}_{out} , because it can change with direction. Since the delta peak is given by the denominator of (2.30), the remaining pre-factor, and from now on referred to as the weight W_{ω_n} of the η th resonance frequency, including the projection onto \hat{e}^{out} amounts to

$$W_{\omega_n} = -i \hat{e}_\alpha^{\text{out}} P_{\alpha\eta} \hat{e}_\eta \hat{e}_\eta^T P_{\eta\beta}^{-1} T_\beta \quad (2.31)$$

2 *Excitations and Linear Response Dynamics*

The direction \hat{e}_{out} corresponds to the direction of measurement, which can potentially differ from the excitation-direction \hat{e}^{in} . The measurements performed accompanying this thesis, both directions are equal for the used coplanar wave guides.

Magnetic Excitations

THE SCHEME TO calculate resonance frequencies in principal has been explained in the previous chapter. We focus in this chapter on concrete applications. Additionally, analytical descriptions are provided and considered where possible.

This chapter considers magnetic excitations only. Electric ones are covered in the next chapter. A cooperation with physicists in Munich provided us with resonance measurements. We start by introducing the experiments from a theoretical and an experimental viewpoint followed by an analysis of an exciting wave with $\mathbf{k} = 0$. Influences of a finite \mathbf{k} -vector are given in the last section.

3.1 Experimental setup

In the remainder of the chapter we discuss magnetic excitations, their resonances to be more precise, firstly of three different materials. Some of their properties have already been introduced in section 1.2. A big influence on the resonance frequencies are not only these material specific properties, but also the shapes of the studied specimen. They are completely different for all three of them and characterized by the following demagnetization factors.

$$\begin{aligned}
 \text{MnSi} \quad N_x = N_y = 0.175, N_z = 0.651 & \\
 \text{Corresponding to a disc with plane normal in z-direction} & \\
 \text{Fe}_{0.8}\text{Co}_{0.2}\text{Si} \quad N_x = 0.074, N_y = N_z = 0.463 & \\
 \text{Corresponding to a rod in x-direction} & \\
 \text{Cu}_2\text{OSeO}_3 \quad N_x = 0.39, N_y = 0.27, N_z = 0.34 & \\
 \text{Corresponding to an almost spherical shape} &
 \end{aligned} \tag{3.1}$$

The setup is such, that an applied static magnetic field \mathbf{H}_0 is always pointing in z-direction and the excitation direction, i.e. the direction of the oscillating field \mathbf{H}^ω , is always the x-direction relating to the given demagnetization factors. It is important for the calculations, that $\hat{\mathbf{e}}_x$, $\hat{\mathbf{e}}_y$ and $\hat{\mathbf{e}}_z$ are the principal axes of the ellipsoid. A sketch of this setup is shown in Figure 3.1. We define $\mathbf{H}^o = \mathbf{H}_0 + \mathbf{H}^\omega$ as the general outer field and \mathbf{H}^i as the internal field combining the outer and demagnetization fields.

Additionally to the three shapes of the specimen, we include a perfect sphere in our calculations as a reference.

3 Magnetic Excitations

Another material specific quantity is the constant susceptibility in the conical phase, which we already mention in subsection 1.4.1. Its values for the three materials and the sphere are

$$\begin{aligned}
 \text{MnSi} & \quad \tilde{\chi}_{\text{con}}^{\text{MnSi}} = 0.28 \\
 \text{Fe}_{0.8}\text{Co}_{0.2}\text{Si} & \quad \tilde{\chi}_{\text{con}}^{\text{Fe}_{0.8}\text{Co}_{0.2}\text{Si}} = 0.5 \\
 \text{Cu}_2\text{OSeO}_3 & \quad \tilde{\chi}_{\text{con}}^{\text{Cu}_2\text{OSeO}_3} = 1.1 \\
 N/A & \quad \tilde{\chi}_{\text{con}}^{\text{sphere}} = 1
 \end{aligned} \tag{3.2}$$

The value for $\tilde{\chi}_{\text{con}}^{\text{sphere}}$ does not represent a specific material, but is chosen to be as simple and still realistic as possible. Whenever we refer to *the three materials* in the remainder of this chapter, we always include the here described setup and shapes, unless specifically noted.

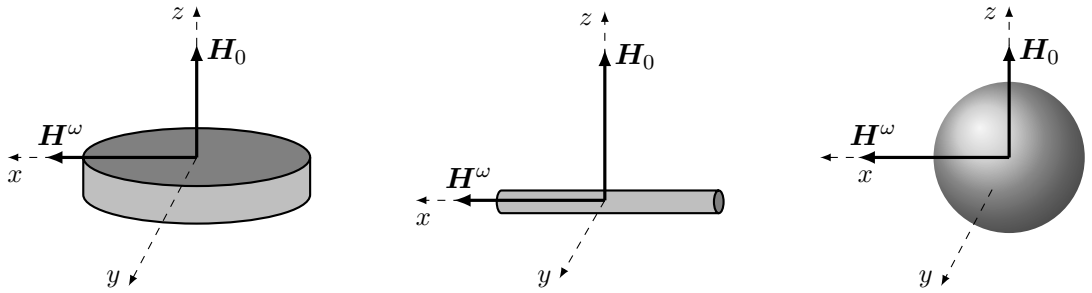


Figure 3.1: Schematic visualization of the experimental setups. The chosen convention is: $\mathbf{H}_0 \parallel \hat{e}_z$ and $\mathbf{H}^\omega \parallel \hat{e}_x$. **Left:** Shape that corresponds to the used MnSi specimen **Middle:** shape of the $\text{Fe}_{0.8}\text{Co}_{0.2}\text{Si}$ specimen **Right:** shape of the Cu_2OSeO_3 specimen.

To provoke dynamic excitations in the specimen experimentally, a coplanar waveguide (CPW) is used [43]. A schematic picture can be seen in Figure 3.2. It consists of two ground lines and a signal line in between. The outer lines carry half the current of the signal line in opposite direction, leading to reversed magnetic field lines. An external magnetic field \mathbf{H}_0 is additionally applied perpendicular to the waveguide and the specimen is placed on top of it. The high frequency field created by the waveguide has a strong in-plane component orthogonal to the external magnetic field, which corresponds to the above defined \mathbf{H}^ω , but also a small out-of-plane component. The latter is at least one order of magnitude smaller than the in-plane component, because of the small height of the CPW of around 120 nm compared to its width of approximately 20 μm .

The in-plane high frequency field induces spin precession in the specimen. The signal created by the induced spin precession then couples inductively back to the CPW. One could say, that the signal line has two purposes. It leads the exciting field to the magnetic specimen and carries the induced voltage signal further to the microwave-detector. This allows for absorption spectroscopy. The resulting data is plotted in the form of gray scale plots as shown in Figure 3.3. These specific plots show raw data of field sweeps in bulk MnSi. Subfigure (a) shows data from a field sweep at a temperature, where no Skyrmion phase occurs. The next two figures (b,c) show measurements that also contain a sweep through the Skyrmion phase at a fixed temperature. The second row shows the temperature dependence of the Skyrmion phase. While the range of the magnetic field sweep is fixed, the extent of the Skyrmion phase is temperature dependent. It is worthwhile to compare these plot to the earlier described phase diagrams for consistency and to gain awareness of the effects of temperature in the setup.

The spin-wave wave vector \mathbf{k} is defined by the geometry of the waveguide. The corresponding wavelength in the used setup is large compared to length scales of the specimen, and hence in particular also much larger than \mathbf{Q} , so that the excitation field can be considered almost

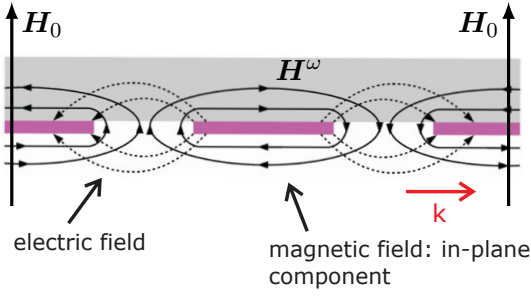


Figure 3.2: Cross-section of the experimental setup of the coplanar waveguide [45] with a homogeneous field H_0 and a high frequency field H^ω .

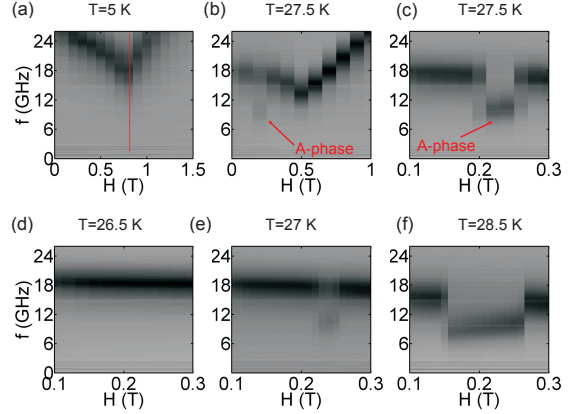


Figure 3.3: Grayscale plots of the absorbed intensity in bulk MnSi. The scale of darkness correspond to the amount of resonance [46]. For details see text.

homogeneous. The fact that it is only almost homogeneous, leads to a broadening of the resonance peaks, which will be explained in more detail later (cf. subsection 3.3.1). The broadening, which is caused by damping as could be seen in the experiments by Onose *et al.* [44], could not be resolved in the considered experiments. We hence do not include damping terms in our theory, because the finite line-width is more likely to be caused by the aforementioned inhomogeneities of the magnetic field.

3.2 Excitations with $\mathbf{k} = 0$ and mode characteristics

In this section we assume, that the static and oscillating outer magnetic fields are both spatially homogeneous. This situation is described by a wavevector $\mathbf{k} = 0$ of the exciting wave. The dynamical contribution to the free energy (1.7) has the form

$$f_{\text{oszil. magnetic}}(t) = -\mu_0 \mathbf{H}^\omega(t) \cdot \mathbf{M} = -\mu_0 \bar{\mathbf{H}} e^{-i\omega t} \cdot \mathbf{M} \quad (3.3)$$

where $\bar{\mathbf{H}}$ is the time independent part of \mathbf{H}^ω . For the numerical calculations, ξ is needed, as defined by (2.27), and given in Fourier space by

$$\xi_{\mathbf{Q}} = \{\bar{\mathbf{H}}; 0; 0; \dots\} \quad (3.4)$$

because \mathbf{H}^ω does not couple to the magnetization with finite \mathbf{Q} .

3.2.1 The polarized phase: Kittel's formula

We have seen and studied in section 2.1 the behavior of spins, or in a broad sense of a ferromagnet, that is subjected to an external magnetic field. The magnetic moments precess around the direction of the applied magnetic field with the Larmor-frequency ω_L , that is proportional to the field strength. We now extend this result by including the influence of the sample shape in our calculations. We use the physical units but the tilde is omitted for this subsection to keep the notation simple. Taking the demagnetization factors N_i into account results in an effective, inner field with components

$$\begin{aligned} H_x^i &= H_x^o - N_x M_x = H^\omega - N_x M_x \\ H_y^i &= H_y^o - N_y M_y = -N_y M_y \\ H_z^i &= H_z^o - N_z M_z = H_0 - N_z M_z \end{aligned} \quad (3.5)$$

3 Magnetic Excitations

Using this new field in the precession equation (2.4), we obtain a set of linear, differential equations.

$$\begin{aligned}\frac{dM_x}{dt} &= \gamma\mu_0 [H_0 + (N_y - N_z)M_z] M_y = \gamma\mu_0\eta_y M_y \\ \frac{dM_y}{dt} &= \gamma\mu_0 [M_z H^\omega - [H_0 + (N_x - N_z)M_z] M_x] = \gamma\mu_0 [M_z H^\omega - \eta_x M_x] \\ \frac{dM_z}{dt} &= \gamma\mu_0 [-M_y H^\omega + (N_x - N_y)M_x M_y] \approx 0\end{aligned}\quad (3.6)$$

For a static magnetic field in z-direction the magnetization points in the same direction. Hence, components perpendicular to that direction can be seen as small, since the perpendicular perturbation \mathbf{H}^ω is small as well. Therefore the last line of (3.6) is of quadratic order and can be neglected. To simplify the notation, we introduced

$$\begin{aligned}\eta_x &:= [H_0 + (N_x - N_z)M_z] \\ \eta_y &:= [H_0 + (N_y - N_z)M_z]\end{aligned}$$

The basis for our calculation was an assumed small oscillation in x-direction, which we now concretize by

$$H^\omega(t) = \bar{H}_x \sin(\omega t)$$

As we have seen in section 2.3, the response of the system is of the same frequency. This leads to the following ansatz for the magnetization.

$$\begin{aligned}M_x(t) &= \bar{M}_x \sin(\omega t) \\ M_y(t) &= \bar{M}_y \cos(\omega t)\end{aligned}$$

Plugging this ansatz into (3.6) brings us to

$$\omega \bar{M}_x = \gamma\mu_0 \eta_y \bar{M}_y \quad (3.7a)$$

$$\omega \bar{M}_y = -\gamma\mu_0 \eta_x \bar{M}_x + \gamma\mu_0 M_z \bar{H}_x \quad (3.7b)$$

Solving (3.7a) for \bar{M}_x leads to an expression for the transversal magnetic susceptibility in x-direction $\chi_{xx}^{mag} = \bar{M}_x / \bar{H}_x$

$$\bar{M}_x = \frac{M_z / \eta_x}{1 - \frac{\omega^2}{\gamma^2 \mu_0^2 \eta_x \eta_y}} \bar{H}_x = \frac{\chi_x^0}{1 - (\omega/\omega_0)^2} \bar{H}_x \equiv \chi_{xx}^{mag} \bar{H}_x \quad (3.8)$$

where $\chi_x^0 = M_z / [H_0 + (N_x - N_z)\bar{M}_z] = M_z / \eta_x$. After an analogous calculation for an exciting field in y-direction, we would obtain

$$\bar{M}_y = \frac{M_z / \eta_y}{1 - \frac{\omega^2}{\gamma^2 \mu_0^2 \eta_x \eta_y}} \bar{H}_y = \frac{\chi_y^0}{1 - (\omega/\omega_0)^2} \bar{H}_y \equiv \chi_{yy}^{mag} \bar{H}_y \quad (3.9)$$

with $\chi_y^0 = M_z / \eta_y$. The resonance frequency ω_0 is in both cases given by

$$\boxed{\omega_0^2 = \gamma^2 \mu_0^2 [H_0 + (N_y - N_z)M_z] [H_0 + (N_x - N_z)M_z]} \quad (3.10)$$

The last line will be referred to as the Kittel formula. It describes the resonance frequency in a ferromagnet including demagnetization factors (cf. [47]). Since we are at $\mathbf{k} = 0$, we are dealing with a uniform mode, in which all moments precess together in phase with the same amplitude around \mathbf{H}_0 . For a perfect sphere, where all $N_i = \frac{1}{3}$, we arrive again at the Larmor-frequency (2.2).

Experimental link

To get a grasp of the effect of demagnetization factors in the polarized regime, the plots in Figure 3.4 below qualitatively show the resonance frequency in dependence of the homogeneous, magnetic field strength for all three materials in comparison to $N_i = \frac{1}{3}$ for $i = 1, 2, 3$ and so representing a perfect sphere. In our cases, we obtain resonance frequencies lower than the Larmor-frequency.

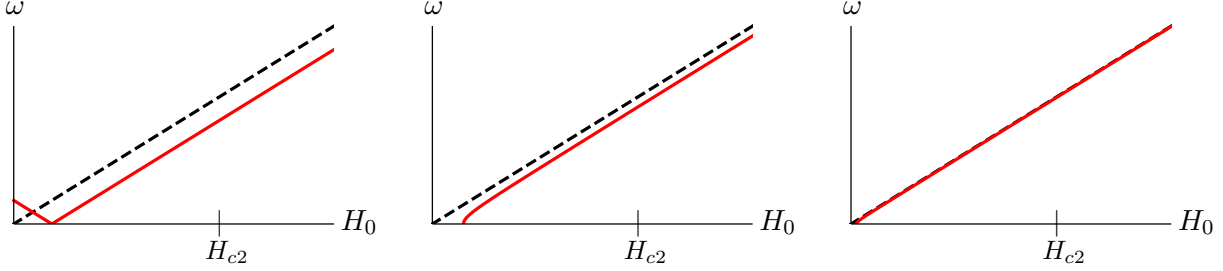


Figure 3.4: Qualitative plots of theoretical resonance frequencies ω in the polarized phase depending on an external magnetic field \mathbf{H}_0 for the three studied materials. Demagnetization factors are included (red curves) and those curves are compared to a perfect sphere (dashed lines). From left to right: MnSi, $\text{Fe}_{0.8}\text{Co}_{0.2}\text{Si}$ and Cu_2OSeO_3 .

The direction of the static magnetic field is of great importance. In the experiments of the disc-shaped MnSi specimen, \mathbf{H}_0 has been applied normal to the disk surface. If it would have been applied in parallel, the resonance frequency curve would change its form significantly as can be seen in Figure 3.5. It now lies above the Larmor-frequency.

To obtain these curves, we have assumed that the body is magnetized to a constant saturation M_{c2} [27]. Since we reach the polarized phase only at comparably high field strengths, such an approximation is justified in the field strength range above H_{c2} , which also corresponds to the appropriate magnetic field range of the field-polarized phase in chiral magnets.

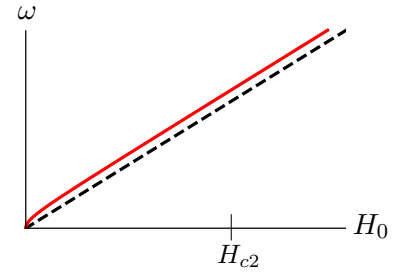


Figure 3.5: Kittel mode with outer field parallel to disc surface.

3.2.2 The conical phase

Resonance frequencies

To obtain the resonance frequencies in the conical phase and ultimately in the Skyrmion phase, we need to calculate the eigenvalues of the matrix

$$\left[\gamma \mathbf{M}^{MF} \times \frac{\delta^2 F_{stat}}{\delta \mathbf{M}^2} \Big|_{\mathbf{M}^{MF}} \right]$$

cf. the derivation of (2.18). Using the helical ansatz \mathbf{M}_{hel} in the chiral basis (1.30) and the expression for the helix amplitude A in terms of χ_{con} and H_{c2} (1.38) plus the term for the homogeneous part M_0 of the magnetization (1.33), it is possible to calculate the resonance frequencies for the conical phase analytically [33]. The obtained expression then only depends on the measured and constant susceptibility $\tilde{\chi}_{con}$, the shape dependent demagnetization factors N_i and the magnetic field, here gauged to the critical field ($\mathbf{h} = \mathbf{H}/H_{c2}$):

3 Magnetic Excitations

$$\begin{aligned}
\frac{\omega_{\pm Q}^2}{(\gamma\mu_0 H_{c2})^2} &= \frac{1}{4} \left(8 + 2(2 + N_x + N_y - 8N_z)\tilde{\chi}_{\text{con}} - (N_x + N_y - 4N_z)(-1 + 2N_z)\tilde{\chi}_{\text{con}}^2 \right. \\
&\quad \left. + h^2(-4 - \tilde{\chi}_{\text{con}}(4 + (N_x + N_y - 2N_x N_y)\tilde{\chi}_{\text{con}} + 4N_z(-2 + (-1 + N_z)\tilde{\chi}_{\text{con}}))) \right) \\
&\quad \mp \tilde{\chi}_{\text{con}} \left[N_x^2 (2 + (1 + h^2(-1 + 2N_y) - 2N_z)\tilde{\chi}_{\text{con}})^2 + N_y^2 (-2 + (-1 + h^2 + 2N_z)\tilde{\chi}_{\text{con}})^2 \right. \\
&\quad \left. + 2N_x N_y \left(- (2 + \tilde{\chi}_{\text{con}} - 2N_z\tilde{\chi}_{\text{con}})^2 - 2h^2(4 + (1 + N_y - 4N_z)\tilde{\chi}_{\text{con}})(-2 + (-1 + 2N_z)\tilde{\chi}_{\text{con}}) \right. \right. \\
&\quad \left. \left. - h^4(8 + \tilde{\chi}_{\text{con}}(8 + \tilde{\chi}_{\text{con}} + 2N_y\tilde{\chi}_{\text{con}} + 8N_z(-2 + (-1 + N_z)\tilde{\chi}_{\text{con}}))) \right) \right]^{\frac{1}{2}} \quad (3.11)
\end{aligned}$$

This result of the analytical calculation yields in fact two different modes, dubbed $\omega_{\pm Q}$, instead of only one found in the polarized phase. This nomenclature was already used by Kataoka in 1987 [48]. In his work, he calculated electron spin resonance energies in systems with a helical/conical spin density wave due to two different origins, one being a symmetric and the other an antisymmetric exchange interaction. In the symmetric exchange interaction, anisotropies are responsible for the helical spin structure. The anti-symmetric one corresponds to the Dzyaloshinsky-Moriya interaction, which we take as the foundation for our theoretical calculations. He proclaims to consider a specimen of spherical shape but sets the demagnetization factors to zero. In the field-polarized phase this would be tantamount to all $N_i = \frac{1}{3}$, but not in the helical/conical phase, as can be seen by plugging these values into (3.11).

$$\omega_{\pm Q}^2|_{N_i=0} = (\gamma\mu_0 H_{c2})^2 (2 + \tilde{\chi}_{\text{con}} - h^2(1 + \tilde{\chi}_{\text{con}})) \quad (3.12)$$

$$\begin{aligned}
\omega_{\pm Q}^2|_{N_i=\frac{1}{3}} &= (\gamma\mu_0 H_{c2})^2 \frac{1}{18} \left[36 - \tilde{\chi}_{\text{con}}^2 + 2h^2(-9 - 3\tilde{\chi}_{\text{con}} + \tilde{\chi}_{\text{con}}^2) \right. \\
&\quad \left. \mp \tilde{\chi}_{\text{con}} \sqrt{h^2(-6 + \tilde{\chi}_{\text{con}})(3h^2(2 + \tilde{\chi}_{\text{con}}) - 2(6 + \tilde{\chi}_{\text{con}}))} \right] \\
&= \omega_{\pm Q}^2|_{N_i=0} + \Delta \cdot (\gamma\mu_0 H_{c2})^2 \quad (3.13)
\end{aligned}$$

with

$$\Delta = \frac{1}{18} \tilde{\chi}_{\text{con}} \left(-18 - \tilde{\chi}_{\text{con}} + 2h^2(\tilde{\chi}_{\text{con}} + 6) \mp \sqrt{h^2(\tilde{\chi}_{\text{con}} - 6)(3h^2(\tilde{\chi}_{\text{con}} + 2) - 2(\tilde{\chi}_{\text{con}} + 6))} \right)$$

which is only zero for $\tilde{\chi}_{\text{con}} = 0$. For example even for $\text{Fe}_{0.8}\text{Co}_{0.2}\text{Si}$ with the lowest conical susceptibility of the three materials, Δ leads to a change in value of about 10%.

One may note here, that the degeneracy of the resonance frequency in the conical phase is only lifted for a finite $\tilde{\chi}_{\text{con}}$ and when demagnetization factors are included.

For the three materials the resonance frequencies are plotted in Figure 3.6 below. The conical susceptibility is decisively influenced by the ratio of μ_0 and $\alpha = JQ^2$. It can, potentially, reach very small values. It is hence instructive to give an expression of $\omega_{\pm Q}$ for $\tilde{\chi}_{\text{con}} \rightarrow 0$. The complicated expression for the resonance frequencies then reduces to the very simple form $\sqrt{2 - h^2}$, which is shown as a dashed line up to H_{c2} in the plots below as well. The dashed line above H_{c2} is just given by $\frac{\omega}{\gamma\mu_0 H_{c2}} = \frac{\hbar\omega}{g\mu_B\mu_0 H_{c2}} = h$, i.e. the Kittel mode for a sphere.

The plots in Figure 3.6 demonstrate nicely the key feature of the calculated resonance formula, namely its universal applicability and temperature independence, when everything is gauged to the critical magnetic field H_{c2} , which by itself is temperature dependent. Another prominent feature is the degeneracy for $\mathbf{H}_0 = 0$ for the disc-shaped specimen MnSi on the very left. This degeneracy happens, whenever the two demagnetization factors for the axes orthogonal to the direction of the static field are equal. In the picture on the very right, the two modes are close at

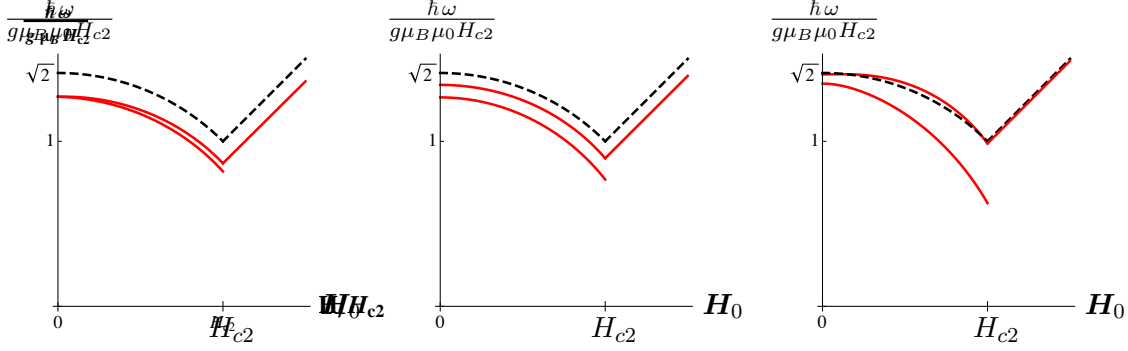


Figure 3.6: Plots of theoretical resonance frequencies in the conical phase for the three studied materials including their dependance on demagnetization factors (red curves) compared to a material with $\tilde{\chi}_{\text{con}} = 0$ (dashed lines). From left to right: MnSi, $\text{Fe}_{0.8}\text{Co}_{0.2}\text{Si}$ and Cu_2OSeO_3 .

that point, but do not touch completely. This is because the shape of the Cu_2OSeO_3 specimen was only close to a sphere, but not a perfect sphere. If that were indeed the case, the two modes would touch at $H_0 = 0$.

The spread between the two modes is greatly determined by $\tilde{\chi}_{\text{con}}$. As one can see it is closest for the MnSi specimen, which has the smallest susceptibility of the three materials, cf. (3.2).

Frequency weights

Numerical calculations provide us with corresponding peak-weights according to (2.31). In the conical phase, we only get two analytical resonances for ω . The matrix R' , however, has many more eigenvalues. The realized resonance frequencies are those eigenvalues, whose corresponding weight is non-vanishing.

Typical plots, in form of bubble-diagrams, of the conical and polarized phases with weights proportional to the area of the bubbles are shown below in Figure 3.7. To emphasize the directional weight dependence, we picked $\text{Fe}_{0.8}\text{Co}_{0.2}\text{Si}$ as an example, because it is the only one of the three materials, whose demagnetization factors are different in the plane perpendicular to the static field direction (cf. (3.1)). The four pictures show different combinations between the incident wave direction and the direction of probing restricted to the xy-plane, because no resonances are obtained in H_0 -direction. Further plots are shown at the end of this section. They comprise theoretical results for all three materials as well as experimental data (cf. Figure 3.11). Nice to see here is, that the one of the conical modes, whose frequency transitions continuously into the Kittel mode, also continuously transitions into the Kittel mode with respect to its weight. While this mode gains full weight, gauged to the weight of the Kittel mode, the second one vanishes as H_0 approaches H_{c2} .

Mode characteristics

To paint a picture about how the oscillating modes are realized in real-space, it is key to remember the initial statement, that spin waves with wave-vectors corresponding to $\mathbf{q} = +\mathbf{Q}$ and $\mathbf{q} = -\mathbf{Q}$ are excited. Onose *et. al* [44] have interpreted the wave motion calculated by Kataoka [48] as two different precession directions of the individual spins, i.e. a clockwise and counterclockwise precession around their equilibrium position. Our analysis shows, that rather the collective excitation changes direction while the individual spins keep the same precession direction.

To be more concrete, let us have a look at the perturbation $\delta\mathbf{M}(\omega)$ of the magnetization. A non-diverging momentum representation of $\delta\mathbf{M}(\omega)$ without the singularity at a resonance frequency

3 Magnetic Excitations

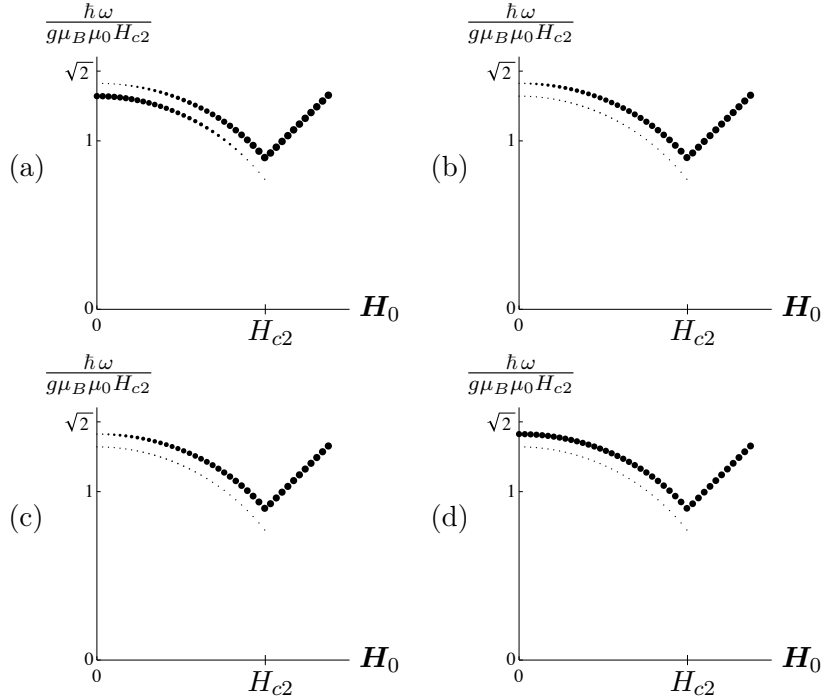


Figure 3.7: Plots of the resonance frequencies in the conical phase up to H_{c2} . Direction of the static magnetic field is always the z-direction. Demagnetization factors are $N_x = 0.074, N_y = N_z = 0.463$. (a) Excitation field in x-direction, probing in x-direction (b) Excitation field in x-direction, probing in y-direction (c) Excitation field in y-direction, probing in x-direction (d) Excitation field in y-direction, probing in y-direction.

ω_η is obtained similarly to the weight, that belongs to the excitation frequency ω . It just lacks the final projection onto the direction of observation.

$$\delta \mathbf{M}_\alpha(\omega_\eta) = -i P_{\alpha\eta} \hat{\mathbf{e}}_\eta \hat{\mathbf{e}}_\eta^T P_{\eta\beta}^{-1} T_\beta \quad (3.14)$$

For real-space interpretations, a Fourier transform of the magnetization back to $\mathbf{M}(\omega, \mathbf{r})$ is needed.

$$\mathbf{M}(\omega, \mathbf{r}) = \sum_{\mathbf{q}} \text{Re} [\mathbf{M}_{\mathbf{q}}^{MF} + \epsilon e^{-i\omega t} \delta \mathbf{M}_{\mathbf{q}}(\omega) e^{i\mathbf{q}\mathbf{r}}] \quad (3.15)$$

where ϵ is a small parameter tuning the approximate strength of the oscillation and the summation over generally infinitely many \mathbf{q} runs only over $\mathbf{q} = -2\mathbf{Q}, -\mathbf{Q}, 0, \mathbf{Q}, 2\mathbf{Q}$. We find no contributions for $|\mathbf{q}| > 2|\mathbf{Q}|$ in general, and for the mean-field part the only contributions come from terms with $|\mathbf{q}| \leq |\mathbf{Q}|$.

The difference between the two modes lies in the strengths of the individual, \mathbf{q} -dependent contributions $\delta \mathbf{M}_{\mathbf{q}}(\omega)$. The setting in the conical phase is such, that we generally excite two modes with frequencies ω_{-Q} and ω_{+Q} where $\omega_{-Q} < \omega_{+Q}$ as long as a present external field and a finite demagnetizing field lift the degeneracy. The labeling of the two frequencies is arbitrary at the moment, but the reasoning will be clear by the end of this subsection.

Starting with the higher frequency ω_{+Q} , numerical calculations reveal, that the corresponding eigenvector in momentum space has the form

$$\delta \mathbf{M}_{\mathbf{q}}(\omega_{+Q}) = \{\mathbf{v}_0, \mathbf{0}, \mathbf{v}_{+Q}, \mathbf{0}, \mathbf{v}_{+2Q}\}$$

with

$$\mathbf{v}_{+Q} = \begin{pmatrix} 0 \\ 0 \\ v_{+Q}^z \end{pmatrix} \quad \text{and} \quad \mathbf{v}_{+2Q} = \begin{pmatrix} v_{+Q}^x \\ v_{+Q}^y \\ 0 \end{pmatrix}$$

The eigenvector of the lower frequency mode ω_{-Q} has components of the form

$$\delta\mathbf{M}_{\mathbf{q}}(\omega_{-Q}) = \{\bar{v}_0, \bar{v}_{-Q}, \mathbf{0}, \bar{v}_{-2Q}, \mathbf{0}\}$$

with

$$\bar{v}_{-Q} = \begin{pmatrix} 0 \\ 0 \\ \bar{v}_{-Q}^z \end{pmatrix} \quad \text{and} \quad \bar{v}_{-2Q} = \begin{pmatrix} \bar{v}_{-2Q}^x \\ \bar{v}_{-2Q}^y \\ 0 \end{pmatrix}$$

The vectors \mathbf{v}_{-2Q} and \mathbf{v}_{+2Q} possess the chiral character in the xy-plane for $\mathbf{v}_{-2Q} \cdot \mathbf{v}_{-2Q} = 0$ and $\mathbf{v}_{+2Q} \cdot \mathbf{v}_{+2Q} = 0$. More importantly, for the higher frequency mode ω_{+Q} the z-component of the magnetization (z-direction is the helix pitch direction in the conical phase) oscillates with $\epsilon v_{+Q}^z e^{-i\omega_{+Q}t} e^{iQz}$. The helix hence experiences a distortion of the neighboring spin tip distances, that propagates *up* the helical staircase. The other mode in turn exhibits the same distortion, but a movement in the opposite direction. The movement is illustrated in Figure 3.8.

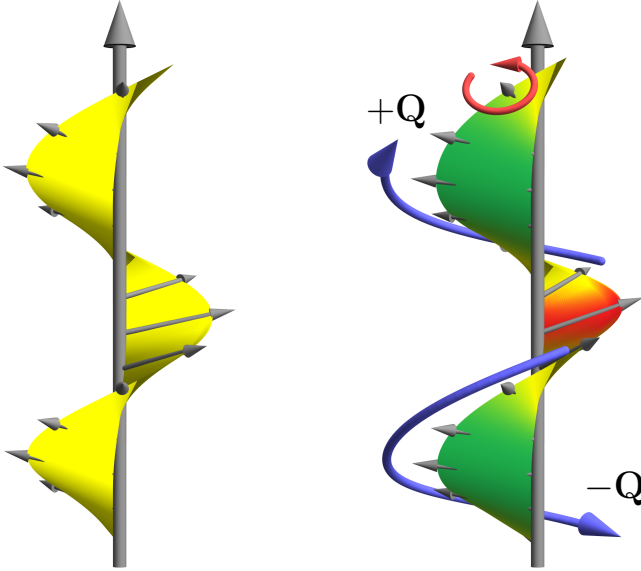


Figure 3.8: Illustration of the excitations in the conical phase. **Left:** Equilibrium state in which all neighboring spin tips have the same distance from each other. **Right:** The equilibrium state is distorted in such a way, that the spin tips of neighboring spins are either closer together (green) or farther away (red). This distortion propagates either *up* or *down* the spiral spin staircase. *Up* is here the direction of the helix pitch vector and the external magnetic field.

If we would have not considered demagnetization fields or looked at zero-field excitations for a select subset of shapes, where the modes join at $|\mathbf{H}_0| = 0$, the two resonance frequencies would be one and the same and two fold degenerate. The calculated eigenvectors, that span the degenerate eigenspace, now contain mixed components of both $\delta\mathbf{M}_{+Q}$ and $\delta\mathbf{M}_{-Q}$, which can be decomposed into two eigenvectors that carry pure $+Q$ and $-Q$ contributions, respectively.

Note, that the numerical calculations have been performed by employing negative gyromagnetic ratio $\gamma < 0$ in the precession equation (2.4), as is the case for electrons. It fixes the sense of the local precession of the spins, indicated by the red arrow in Figure 3.8.

Historical and recent measurements

In 1977, Date *et al.* measured electron spin resonances in MnSi single crystals. Their experimental results yield the same two peak structure in the conical phase of which one mode continuously transitions into the Kittel mode in the polarized phase, just as we have calculated here. They try to explain their results with a theory developed by Cooper and Elliot, and give a concrete

3 Magnetic Excitations

formula for the resonance frequencies [49]. However, their consideration of demagnetization effects do not coincide with our calculations. Their theoretically calculated curves therefore look a little optimistically fitted to the data. Furthermore, as Kataoka already pointed out in [48], their derivation is based on a symmetric exchange interaction which requires a uniaxial magnetic anisotropy, whose origin is not necessarily obvious. The shape of our calculated curves would explain for one the small discrepancy in their peak position, but would also explain missing data points for the higher frequency branch, because of peak weight loss.

More recently in 2012, Onose *et al.* measured resonance frequencies in bulk Cu_2OSeO_3 [44]. The shape of their resonance peak positions within the conical phase and Skyrmion phase, the latter is discussed in the next section, concurs with our theory very well. They even provide measurements for the purely helical phase. By adding anisotropy effects to our numerical calculations, it is conceptually possible to arrive at the measured peak positions. But since different terms could potentially lead to the same shift it is not certain which ones contribute primarily in the helical phase. The only thing one can say so far is, that anisotropy terms are responsible for a change in the resonance frequencies in the helical phase with respect to the conical phase.

3.2.3 The Skyrmion phase

Resonance frequencies

We apply the same numerical method as in the conical phase, to obtain the resonance frequencies and corresponding weights in the Skyrmion phase. Unfortunately it is not possible to express them in an analytical fashion. We take the eigenvalues of R in (2.29) again as all possible resonance frequencies.

Considering all potential resonance frequencies and plotting them including their weight analogously to the conical plots in Figure 3.7, we get a plethora of modes. Nearly all of the modes with small weight fluctuate strongly, if one changes the ring number used to calculate the resonance frequencies. Because it is, for one, not certain enough whether those strongly fluctuating modes will stabilize and secondly, they have a vanishingly small weight, we focus on the modes, that arrive at a stable position and have a considerable weight. These are essentially two modes for magnetic excitations perpendicular to the static magnetic field and one for excitations parallel to the external field.

EXCITATIONS ORTHOGONAL TO \mathbf{H}_0 – In the orthogonal excitation direction, we obtain two stable modes with non-negligible weight. The two modes are plotted in red in Figure 3.9 for a perfect sphere in comparison to the conical and polarized resonances shown as a dashed line. Demagnetization effects affect merely the overall position of the resonances, but not the shape of the branches or their weight distribution as they have in the conical phase.

EXCITATIONS PARALLEL TO \mathbf{H}_0 – In the case of an excitation parallel to the static magnetic field, i.e. orthogonal to the Skyrmion lattice, the analysis yields only one significant mode. Its frequency dependance on the magnetic field strengths is also shown in Figure 3.9 as a blue curve.

Mode characteristics

Like in the conical phase, each of the three Skyrmion modes relates to a different characteristic movement in real-space. The two modes in the orthogonal case are a *clockwise* and *counterclockwise* rotation of the averaged z-component of the magnetization around the center of each Skyrmion. As usual, \hat{e}_z points in external field direction. The question of which mode corresponds to which

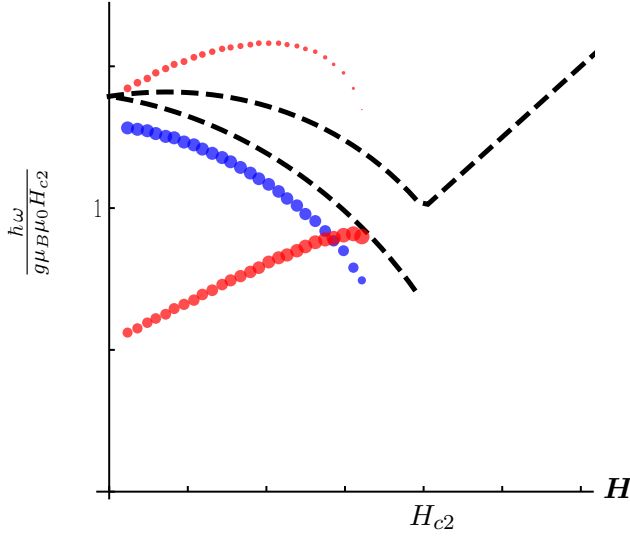


Figure 3.9: Plot of resonance frequencies in the Skyrmion phase for a perfect sphere. The numerical cutoff is four rings. As an orientation, the resonances of the conical and polarized phases are shown by dashed lines. Considerable resonances of an excitation perpendicular to the external field are shown in red, resonances for a parallel excitation are shown in blue.

rotation direction is actually not answered by the sign of the Dzyaloshinsky-Moriya term in the free energy, but by the sign of γ in (2.4). We chose a negative sign and obtain a counterclockwise rotation for the low frequency mode and a clockwise rotation for the high frequency mode. An illustration of the different movements is given in Figure 3.10. They have already been calculated in a Monte-Carlo simulation by Mochizuki *et al.* [50]. Their calculated rotation directions concur with ours, i.e. $\omega_{CCW} < \omega_{CW}$. It has to be noted, that their chosen sign for the Dzyaloshinsky-Moriya interaction is just the opposite of ours, which again demonstrates the independence of the rotation direction on the Skyrmion chirality.

For an exciting field parallel to the static field, Mochizuki *et al.* predict a *breathing* mode, which perfectly agrees with our results in Figure 3.10.

3.2.4 Summary and experimental comparison

At this intermediate point, it makes sense to reflect on the so far obtained results. For an exterior field strength H_0 greater than H_{c2} , i.e. in the field-polarized phase, we find the so-called Kittel mode as an answer to an additionally applied, oscillating field \mathbf{H}^ω , whose field strength is small compared to the external homogeneous field. It is important, that this perturbation is applied perpendicular to the static field. For $H_0 < H_{c2}$, there are potentially five different modes of the system, though they cannot all be excited and seen simultaneously. Only one, belonging to the Skyrmion phase, is obtained, if the oscillating component of the magnetic field is parallel to the static component. The other four potentially occur below H_{c2} , when the oscillating field \mathbf{H}^ω is applied perpendicular to the static field component. Two of them in the conical phase and two in the Skyrmion phase. Their actual occurrence is temperature dependent as can be deduced from the phase diagrams of the three studied materials, cf. Figure 1.2.

Magnetic field and frequency sweeps were generally measured for a fixed temperature. This has been done by experimentalists in Munich for the three materials, each for a couple of different temperatures. The resulting intensity distributions have then been reduced to points with error bars. Comparing graphs are shown in Figure 3.11. As one can see, the measured data agrees very well with our theoretical calculations. An important feature is, that our calculated resonance spectra are universally applicable to numerous materials, as long as their demagnetization factors and susceptibilities in the conical phase are known. Temperature merely influences which phase is realized at which magnetic field strength. In Cu_2OSeO_3 for example, the Skyrmion phase is only reached, at the measuring temperature of 57.0 K but then stretches over quite an extended magnetic field range, compared for instance to $\text{Fe}_{0.8}\text{Co}_{0.2}\text{Si}$.

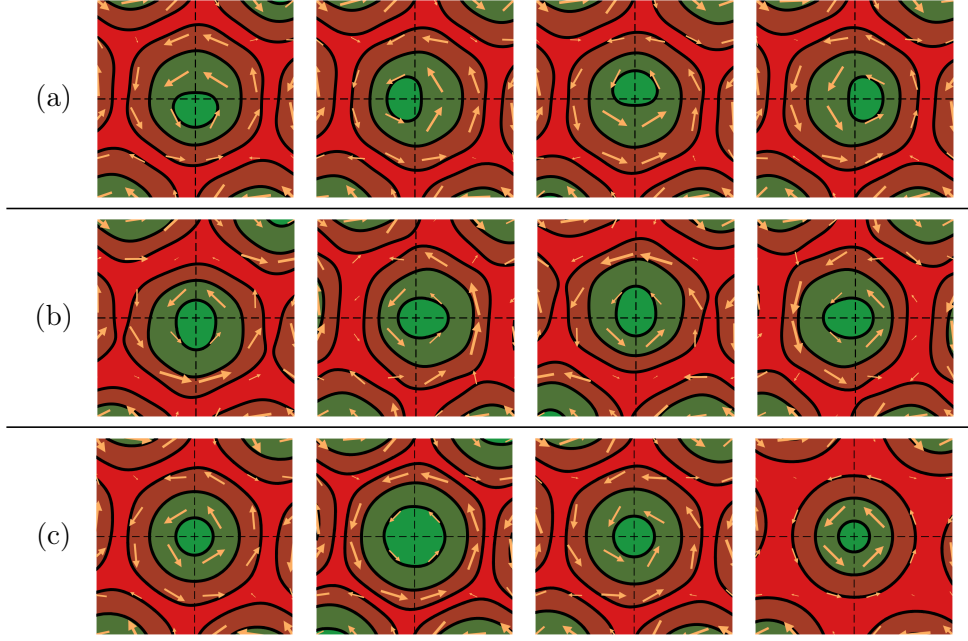


Figure 3.10: The xy-component of the magnetization is shown in each case by an amber colored arrow. The z-component is represented by a contour plot where green corresponds to the magnetization pointing into the plane, i.e. parallel to the line of sight, and red stands for the magnetization pointing out of the plane, as does the static magnetic field. (a) Clockwise, high frequency mode (b) Counterclockwise, low frequency mode (c) breathing mode.

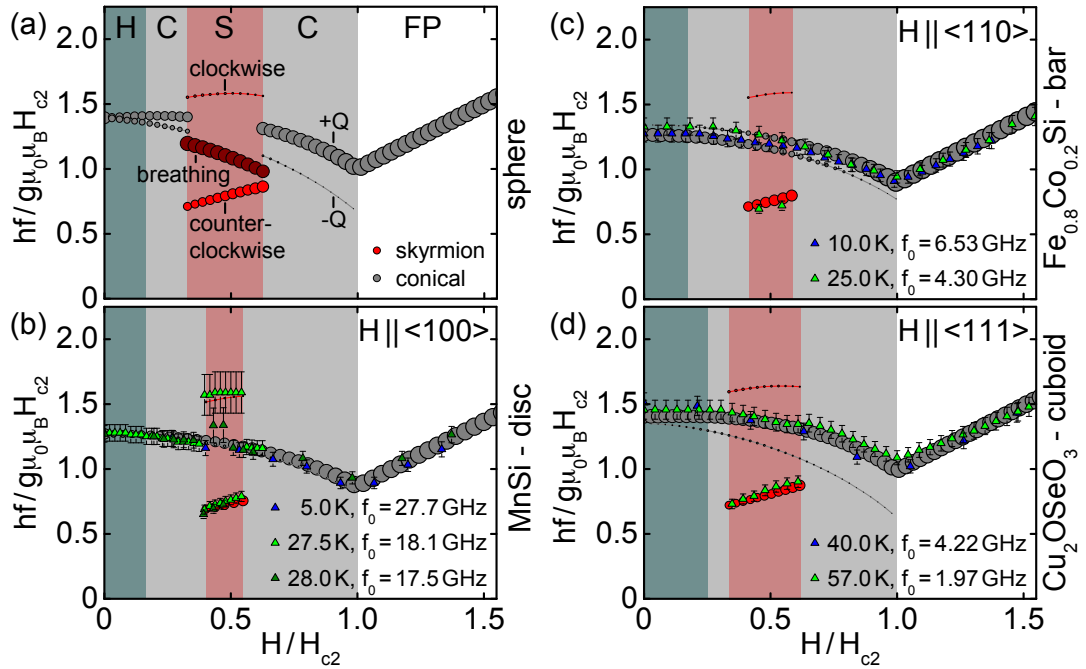


Figure 3.11: Experimental results of resonance measurements with the exciting field direction perpendicular to the direction of the static magnetic field \mathbf{H} ((b)-(d)). Experimental data are represented by green and blue triangles according to the appropriate temperature. The circles represent numerical calculations. Gray: conical and field-polarized phase, red: Skyrmion phase. In panel (a) the breathing mode, which only occurs for an excitation field parallel to the static field, is shown in dark red. The vertical stripes indicate the different phases. They include a teal colored one representing the purely helical phase below H_{c1} for completeness. Its properties due to anisotropies were, however, not included in the shown calculations due to the lack of experimental resolution: it was impossible to tell the difference between the conical or helical phase unlike in the experiments of Onose *et al.* [44].

3.3 Excitations with a finite \mathbf{k}

3.3.1 Consequences for data obtained by experiments

So far we assumed, that the experimental setup produces a completely homogeneous magnetic field. For this reason, we chose the exciting wave to be homogeneous in space as well, and only varying in time. As it turns out, the exciting field cannot be seen as completely homogeneous. Rather, we have to describe the situation by a field with a finite, though relatively large, wavelength in space, that is, however, of the same order of magnitude as the dimension of the specimen. To comply with this demand, we need to calculate the resonance frequencies not for an excitation with $\mathbf{k} = 0$ but $\mathbf{k} \rightarrow 0$. As a consequence we cannot rely on the demagnetization factors any more, but have to take long range dipole-dipole interaction as the responsible effect into account. They are described in subsection 1.3.3.

For the analysis of the resonance frequencies, we start again with the precession equation (2.4) for resonances in the field-polarized phase. As a preparatory step, we define again that the static magnetic field \mathbf{H}_0 points in z-direction. The linear ansatz for the magnetization consists hence of a large static component \mathbf{M}_0 in field direction, and by neglecting amplitude modulations, small fluctuating components in x- and y-direction.

$$\mathbf{M} = \mathbf{M}_0 + \begin{pmatrix} \delta M_x e^{i(\omega t + \mathbf{k} \cdot \mathbf{r})} \\ \delta M_y e^{i(\omega t + \mathbf{k} \cdot \mathbf{r})} \\ 0 \end{pmatrix} = \begin{pmatrix} \delta M_x e^{i(\omega t + \mathbf{k} \cdot \mathbf{r})} \\ \delta M_y e^{i(\omega t + \mathbf{k} \cdot \mathbf{r})} \\ M_z \end{pmatrix} \quad (3.16)$$

The internal field then consists out of the mentioned static part plus the magnetic field created by the spins within the magnet itself. The latter contribution is given in Fourier space by (1.18). For the effective, internal magnetic field we get in total

$$\mathbf{H}^{eff} = \begin{pmatrix} 0 \\ 0 \\ H_0 \end{pmatrix} - \frac{\mathbf{k} \cdot \delta \mathbf{M}}{|\mathbf{k}|^2} \mathbf{k} e^{i(\omega t + \mathbf{k} \cdot \mathbf{r})} \quad (3.17)$$

Plugging the approximations into the precession equation brings us to

$$-i\omega \delta \mathbf{M} = \gamma \mu_0 \left(-\mathbf{M}_0 \times \mathbf{k} \frac{\mathbf{k} \cdot \delta \mathbf{M}}{|\mathbf{k}|^2} + \delta \mathbf{M} \times \mathbf{H}_0 \right) \quad (3.18)$$

Neglecting higher order terms yields a set of linear differential equations for the x- and y-components of $\delta \mathbf{M}$.

$$\begin{aligned} -i\omega \delta M_x &= \gamma \mu_0 \left[M_z \left(\frac{k_x k_y}{|\mathbf{k}|^2} \right) \delta M_x + \left(H_0 + M_z \left(\frac{k_y^2}{|\mathbf{k}|^2} \right) \right) \delta M_y \right] \\ -i\omega \delta M_y &= -\gamma \mu_0 \left[\left(H_0 + M_z \left(\frac{k_x^2}{|\mathbf{k}|^2} \right) \right) \delta M_x + M_z \left(\frac{k_x k_y}{|\mathbf{k}|^2} \right) \delta M_y \right] \end{aligned}$$

A solution ω_0 to this set of equations has been calculated by Herring and Kittel [51] for $\mathbf{k} \rightarrow 0$ and is given in our notation by

$$\omega_0^2 = \gamma^2 \mu_0^2 (H_0^2 + M_z H_0 \sin^2 \theta_{\mathbf{k}}) = \gamma^2 \mu_0^2 H_0 (H_0 + M_z \sin^2 \theta_{\mathbf{k}}) \quad (3.19)$$

where $\theta_{\mathbf{k}}$ is the angle between \mathbf{k} and the static, magnetic field direction \mathbf{H}_0 . Having an excitation with a finite but small momentum, hence leads to a modulation of the resulting resonance frequency between two boundaries, depending on the direction of \mathbf{k} . The first boundary is given

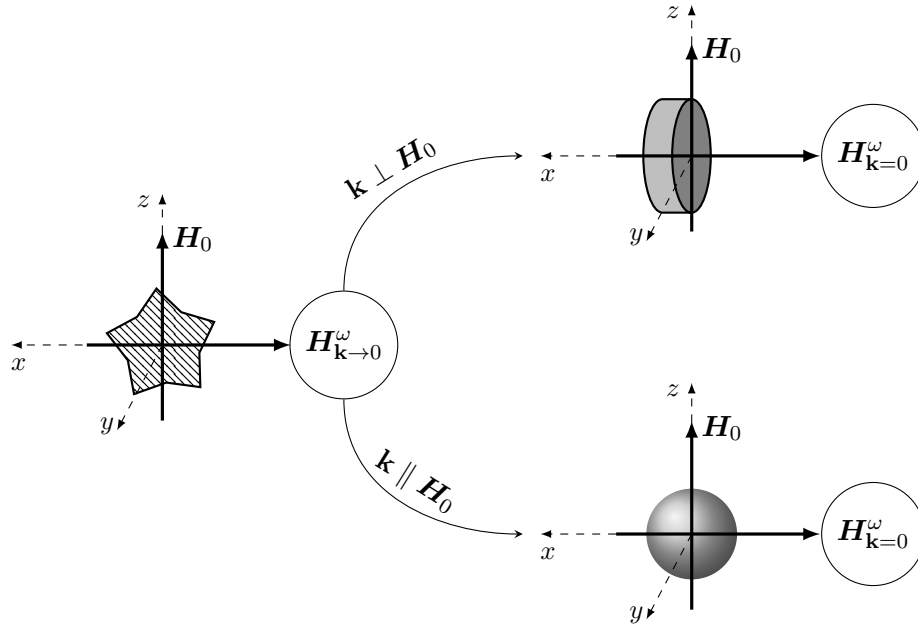


Figure 3.12: Schematic description of how an excitation with finite \mathbf{k} -vector and $\mathbf{k} \rightarrow 0$ relates to an excitation at $\mathbf{k} = 0$, depending on the direction of \mathbf{k} . The striped star represents an arbitrary shape of the specimen. For more details see text.

by the case of $\mathbf{k} \parallel \mathbf{H}_0 \leadsto \sin \theta_{\mathbf{k}} = 0$ and is actually equivalent to the case of $\mathbf{k} = 0$ and a sample shape of a perfect sphere with all demagnetization factors $N_i = \frac{1}{3}$, cf. (3.10). The other extremal case is $\mathbf{k} \perp \mathbf{H}_0$ which corresponds again to a familiar case with $\mathbf{k} = 0$. This time with the shape of an infinite disc, where the homogeneous field is applied parallel to the surface, i.e. in our notation $N_y = N_z = 0$ and $N_x = 1$. As a result, one can summarize the following: conducting a magnetic resonance experiment in the field-polarized phase with a specimen of an arbitrary shape and a not completely homogeneous field, gives resonances, that are not unambiguously described by demagnetizing factors. They rather lie in a broader zone, whose borders could be obtained by conducting an experiment with an indeed homogeneous excitation field, i.e. $\mathbf{k} = 0$, and the specimen in two shapes, namely the perfect sphere for the lower boundary and a potentially infinite disc with the static field applied parallel to the surface. This relationship is shown conceptually in Figure 3.12.

In the numerical approach for the $\mathbf{k} \rightarrow 0$ case, we boldly picked a small enough, finite value for k for either the parallel or orthogonal direction to \mathbf{H}_0 of about $k = 10^{-4}$ with $k \approx \frac{1}{2}$ being the border of the 1. BZ. This is more than justified for the orthogonal direction, because the thereby calculated frequencies converge with a zero slope, to a finite value for $\mathbf{k} \rightarrow 0$, which is, of course, different to the value at $\mathbf{k} = 0$. And for the longitudinal direction, the slope is small enough, so that the change in frequency at $k \approx 10^{-4}$ is orders of magnitude smaller than the frequency itself, and therefore negligible. The calculations show, that there are also limiting values for the resonance frequencies in the conical and Skyrmion phase. They effectively yield a band-like area, in which the possible resonance frequencies may lie, when the exciting field is not completely homogeneous. Plots, analog to those in Figure 3.11, are shown in Figure 3.13, including the mentioned bands as a gray background area for the conical and field-polarized phase and dark red bands for the Skyrmion phase.

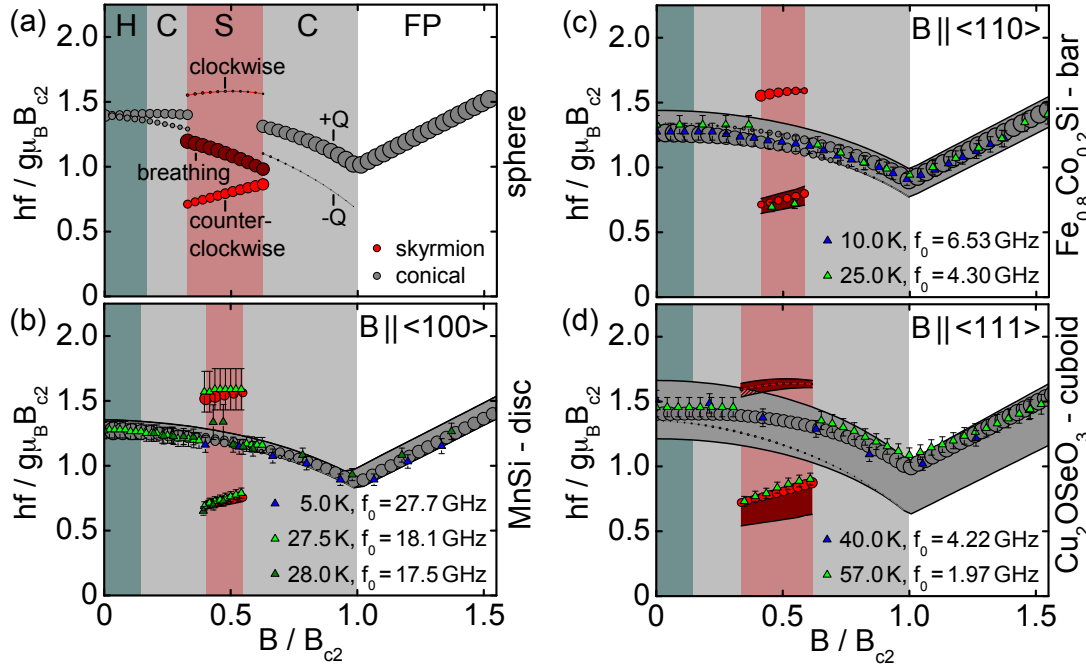


Figure 3.13: Experimental and theoretical results in comparison, analog to Figure 3.11. Here included are gray and dark red bands in the background, that indicate a broader area, where resonance peaks may lie, when the excitation field is not completely homogeneous.

3.3.2 Dispersion relations

Spontaneous symmetry breaking occurs, when a system is invariant under a certain global continuous symmetry, for example rotational symmetry of all spins in a ferromagnet, but its ground state, e.g. the ordered state of the exemplary ferromagnet, does not possess the same symmetry [42]. In that case, one finds soft modes due to residual fluctuations on top of the symmetry broken ground state, called Goldstone modes, or in the example from above: ferromagnetic magnons. In subsection 2.1.2 we have seen, that these magnons carry a quadratic dispersion relation, $\omega \propto k^2$, which is an expression for the price, that needs to be paid when including weak spatial fluctuations in the coordinate profile. Also mentioned in said subsection is the anisotropic dispersion relation for helimagnons, that are Goldstone modes in the purely helically ordered state. While also quadratic in k in the direction perpendicular to the propagation direction of the helices, their dispersion relation is linear in pitch direction. We confirm that statement in this subsection numerically, extend it to the conical case with a finite, static magnetic field components and present numerical results for the Skyrmion phase. We also study the impact of long-range dipole-dipole interaction to the dispersion relations.

Figure 3.14 shows numerical results in the conical phase. Calculations done without dipole-dipole interactions are shown in black while their inclusion give the red curves. Numerical results for the Skyrmion phase are presented in Figure 3.15.

In the helical phase with $\mathbf{H}_0 = 0$ we reproduce the predictions of Belitz *et al.* [41] quite nicely. Without anisotropies, nothing changes in the direction parallel to the pitch vector \mathbf{Q} when the magnetic field is turned on and one goes over into the conical phase. The behavior of the dispersion orthogonal to \mathbf{Q} , on the other hand, changes from a quadratic to a linear dispersion as H_0 increases. Concerning dipole-dipole interaction, one can say, that they do affect merely the slope of the dispersion relation, but not their character. In the purely helical case for $\mathbf{k} \perp \mathbf{Q}$, they do not seem to change the dispersion relation at all.

3 Magnetic Excitations

We find, that the Goldstone modes have a quadratic dispersion relation in directions parallel and orthogonal to the applied magnetic field. The results for the latter direction is independent of the rotation angle around \mathbf{H}_0 . Also in this case, the dipole-dipole interaction does not affect the \mathbf{k} -dependence of the dispersion relation significantly.

While our studies were mainly confined to the regime of $\mathbf{k} \approx 0$, it might be interesting for future studies to do calculations for wave vectors of sizeable values. They could lead to potentially different results for the resonance frequencies especially in the longitudinal helix direction during the transition between the helical and conical phase.

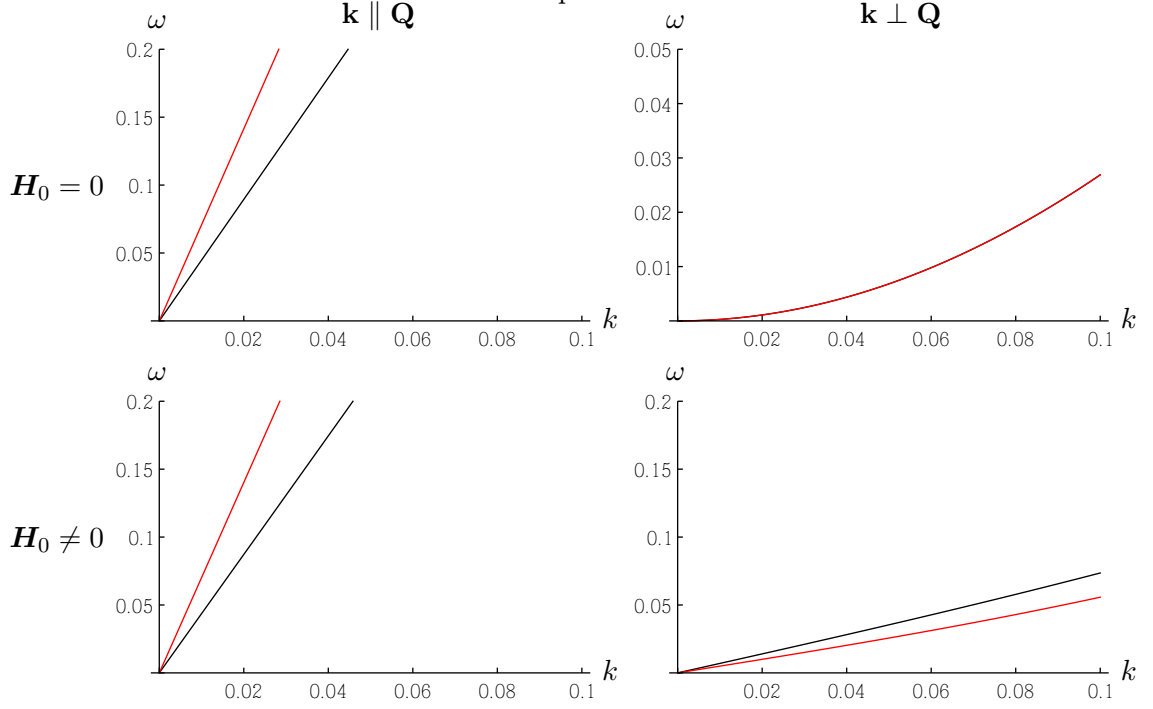


Figure 3.14: Dispersion relations in the conical phase. Black lines are obtained via calculations that include just the f_0 term in the free energy (1.7) and the red curves by including demagnetization fields of the sphere and dipole-dipole interactions (1.21). In the picture on the upper right, both curves lie on top of each other. The scale of ω is in arbitrary units and the scale of k is in fractions of $|\mathbf{Q}|$.

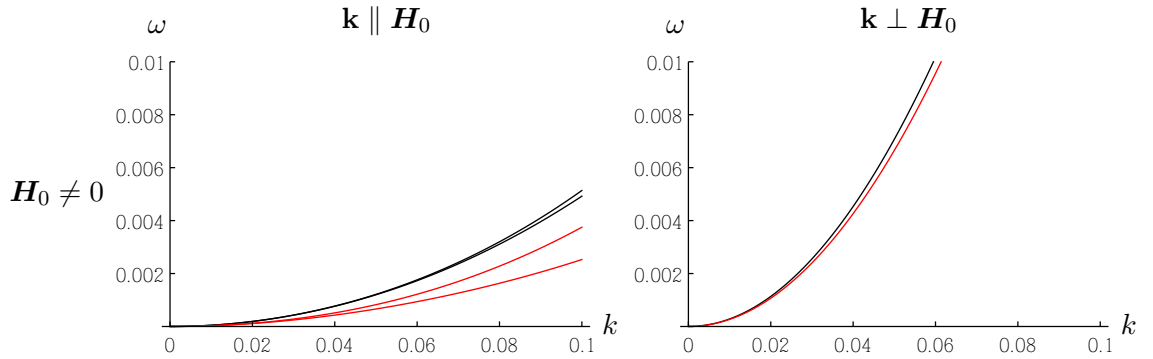


Figure 3.15: Dispersion relations in the Skyrmion phase. Black lines are obtained via calculations that include just the f_0 term in the free energy (1.7) and the red curves by including demagnetization fields of the sphere and dipole-dipole interactions (1.21). Since Skyrmions only form in the presence of a finite magnetic field, plots for zero field are not shown. The scale of ω is in arbitrary units and the scale of k is in fractions of $|\mathbf{Q}|$.

Electric Excitations

ELECTRIC EXCITATIONS OCCUR, for instance, when an oscillating electric field couples to a polarization. This chapter introduces an expression for the polarization to the theory as well as the coupling to an exciting electric field. The different nature of said coupling leads to a stronger directional dependence, compared to magnetic excitations, which is discussed. Finally, we give a brief overview of the change of the resonance frequencies compared to purely magnetic excitations.

4.1 The polarization

Skyrmions and the helical structure in B20 compounds are magnetic structures. Most of the time, magnetism and ferroelectricity occur only individually in materials and, when they do coexist, interact only marginally with each other [52]. Recent studies on multiferroics found, that non trivial magnetic structures like spin frustration, can cause the appearance of a spontaneous polarization, that can be manipulated by magnetic fields [53]. Particularly the Skyrmion spin structure affects the symmetry of charge distribution and induces a finite polarization [7], that is influenced by a magnetic field. The reverse argument is, that an electric field can influence the magnetic structure. This could have future engineering advantageous because, in insulating materials like Cu_2OSeO_3 , the energy dissipation of an electric field is negligibly and a manipulation of Skyrmions via an electric field could hence be more energy efficient compared to current driven manipulations in metals [7].

These multiferroic properties motivate us to study the electric polarization and charge, carried by Skyrmions and helices, in more detail and furthermore, the effect of electric excitations in chiral magnets.

4.1.1 Introduction and derivation of the static polarization in chiral materials

The electric dipole moment per unit volume, i.e. the polarization \mathbf{P} , is given by electrodynamic textbooks as follows [54]

$$\mathbf{D} = \epsilon_0 \mathbf{E} + \mathbf{P} = \epsilon_0(1 + \chi_{el})\mathbf{E} \quad (4.1)$$

with the displacement \mathbf{D} , an electric field \mathbf{E} , the dielectric constant ϵ_0 and especially

$$\mathbf{P} = \epsilon_0 \chi_{el} \mathbf{E} \quad (4.2)$$

Analogous to our studies in the magnetic case, we are now not interested in the magnetic susceptibility, but in the electric susceptibility $\chi_{el} = \frac{\partial \mathbf{P}}{\partial \mathbf{E}}$, that also appears in (4.1). First,

however, we need an expression for \mathbf{P} , that suits our problem setup. Such a local expression for the Ginzburg-Landau theory of order parameters has been given by Ye-Hua Liu *et al.* [55] as

$$\mathbf{P} = \lambda \begin{pmatrix} M_y M_z \\ M_z M_x \\ M_x M_y \end{pmatrix} \quad (4.3)$$

with a coupling constant λ . Its derivation bases upon the so-called *pd*-hybridization, which has also been confirmed by Seki *et al.* [56] to be the mechanism responsible for electric dipole moment induction in Cu_2OSeO_3 .

Like the magnetic field couples to the magnetization in the free energy, so couples the electric field to the polarization. For the last term of (1.7) we obtain

$$f_{\text{oszil. electric}}^\omega(t) = \mathbf{E}(t) \cdot \mathbf{P} \quad (4.4)$$

That background in mind, it is possible to motivate such a term on symmetry grounds [57]. Under time reversal $t \rightarrow -t$, the polarization transforms as $\mathbf{P} \rightarrow \mathbf{P}$, the electric field as $\mathbf{E} \rightarrow -\mathbf{E}$ and the magnetization as $\mathbf{M} \rightarrow -\mathbf{M}$. This requires the lowest order coupling term to be quadratic in \mathbf{M} . Additionally, the symmetries of the $P2_13$ non-centrosymmetric spacegroup need to be obeyed, as well as combinations of time inversion symmetry and crystal symmetries. For example, an allowed rotation of angle π around $[001]$ has the following transformations as a result.

$$\mathbf{R}_{[001]}^\pi \quad \begin{array}{ll} E_x \rightarrow -E_x & M_x \rightarrow -M_x \\ E_y \rightarrow -E_y & M_y \rightarrow -M_y \\ E_z \rightarrow E_z & M_z \rightarrow M_z \end{array} \quad (4.5)$$

The x-component of \mathbf{E} obtains a minus sign, and the only way for (4.4) to be invariant, is for the quadratic magnetization term to be either $M_x M_z$ or $M_y M_z$. Considering additionally a rotation about $[100]$, we get that only a term proportional to $E_x M_y M_z$ is allowed. Checking all possible combinations leads to a term of the form (4.4) with \mathbf{P} as defined in (4.3).

For the time dependent electric field, we use the following convention throughout this chapter.

$$\mathbf{E}^\omega(t) = \bar{\mathbf{E}} \sin(\omega t) \quad (4.6)$$

where $\bar{\mathbf{E}}_{in}$ encapsulates the excitation direction.

4.1.2 Directional dependance of the static polarization on the external magnetic field

While the magnetic excitations depend, at least in the field-polarized phase as well as the conical and Skyrmion phases, purely on the direction of the external magnetic field and the excitation direction, the situation could be different, when dealing with electric excitations. The crystal alignment now plays an elevated role, since the polarization depends explicitly on it. Three characteristically different directions are $[001]$, $[011]$, $[111]$ and have the following properties in the static case:

$$\mathbf{M} \parallel [001] \curvearrowright \mathbf{P} = 0 \quad \mathbf{M} \parallel [011] \curvearrowright \mathbf{P} \parallel [100] \quad \mathbf{M} \parallel [111] \curvearrowright \mathbf{P} \parallel [111]$$

In the field-polarized phase, this translates directly to a relation between \mathbf{P} and the magnetic field direction, because $\mathbf{H}_0 \parallel \mathbf{M}$.

The other phases are characterized by the magnetic field direction as well, but the proper polarization has to be calculated using the explicit local magnetization direction.

4.1.3 The polarization and charge in the Skyrmion and conical phases

Due to its directional dependance on the local magnetization, the polarization in the Skyrmion phase is most interesting, as it has the most diverse magnetic structure of the three studied phases. Additionally, it carries a local electric charge, which is proportional to the divergence of the polarization [54].

$$\rho_{\text{sky}}(\mathbf{r}) = \nabla \cdot \mathbf{P}(\mathbf{r}) \quad (4.7)$$

In Figure 4.1 we show a vector-density plot of the familiar magnetization distribution of the Skyrmion lattice as a point of reference for the other plots in the picture, which relate to the same Skyrmion position arrangement. The other plots in Figure 4.1 contain maps of the local polarization within the Skyrmion plane as well as a mapping of the local electric charge carried by the Skyrmions. These two types of plots are shown for the three, aforementioned, different directions of the applied magnetic field. One can see, that they are quite different. Furthermore, there is a nice effect to be noticed, that is due to the overlay of the cubic symmetry and the hexagonal Skyrmion structure. If one looks closely, one can see, that the Skyrmion arrangement is slightly tilted with respect to the cubic axes, for example in the $\mathbf{H}_0 \parallel [001]$ case with respect to $[100]$. This is a consequence of the lack of anisotropy terms in our calculations. Despite this angular offset, the polarization and charge keep their orientation according to the crystal axes. In fact, they rather seem to shear like a parallelogram than rotate around a given Skyrmion center.

The color coding of each of the plots in Figure 4.1 is scaled individually between minus one and one, according to the individual minimal and maximal value of the polarization component. This scaling lets us resolve the structure of the plot in the most detailed way. It furthermore lets us compare these plots to pictures obtained by Seki *et al.* [56] and Mochizuki *et al.* [58] with which we find good agreement.

Figure 4.2 shows the same plots, but with a different scaling. There, we use a global maximum of the absolute value of the polarization and charge components as the outer limit of the color code. This lets us compare the different strengths of the polarization and charges between the different field directions. It is noticeable, that there is a strong bias of the polarization component in magnetic field direction for the $[011]$ and $[111]$ field directions, while its maximal and minimal values equally polarize in the $[001]$ case.

The polarization and charge in the conical phase has been calculated analogously. The results are shown in Figure 4.3 and Figure 4.4. Here, the change in polarization and charge, respectively, does not happen in planes perpendicular to the applied magnetic field, but only parallel to it. The color coding is the same as in the Skyrmion case. Most interesting is a magnetic field direction of $[111]$, which leads to vanishing of the charge in the considered plane. Interestingly enough this does not happen spontaneously but gradually when tilting the field from the $[001]$ direction, where the carried, local charge is largest, to the $[111]$ direction. Similarly, the polarization component perpendicular to the plane, changes from equally polarized in both directions to almost uniform in $[11\bar{2}]$ direction.

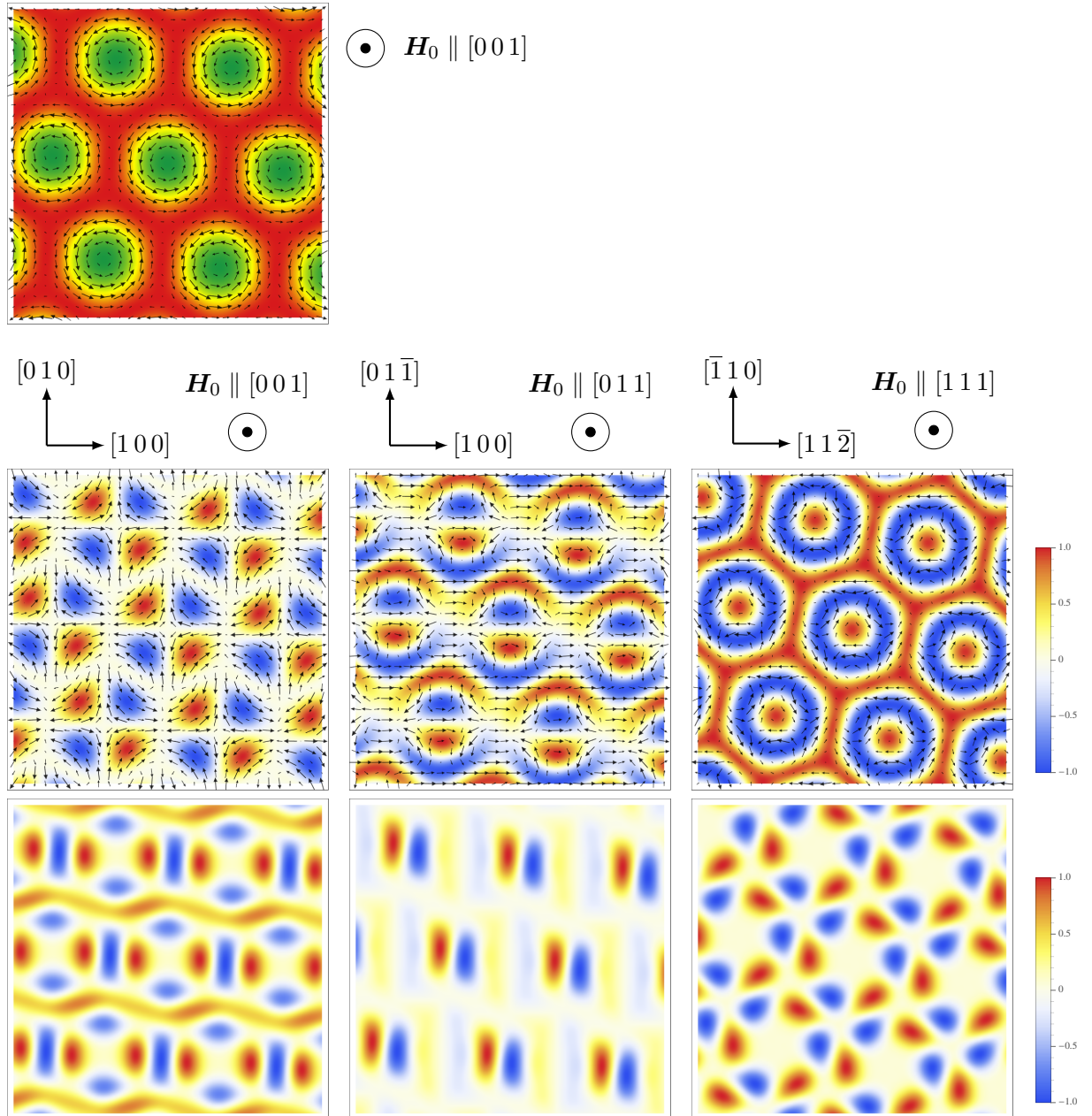


Figure 4.1: Top row: Magnetization in the Skyrmion Phase. Color coding represents the magnetization component in field direction (green = antiparallel, red = parallel). Arrows represent the in-plane components.

Middle row: The polarization of the Skyrmion phase in dependence of the magnetic field direction as shown by directional drawings above.

Bottom row: Local electric charge in the Skyrmion phase in dependence of the magnetic field direction.

The scaling of the density plots has been done as such, that the minimum and maximum value of the polarization and charge, respectively, were taken for each picture individually, and the color code interpolates between those two values. For more details see text.

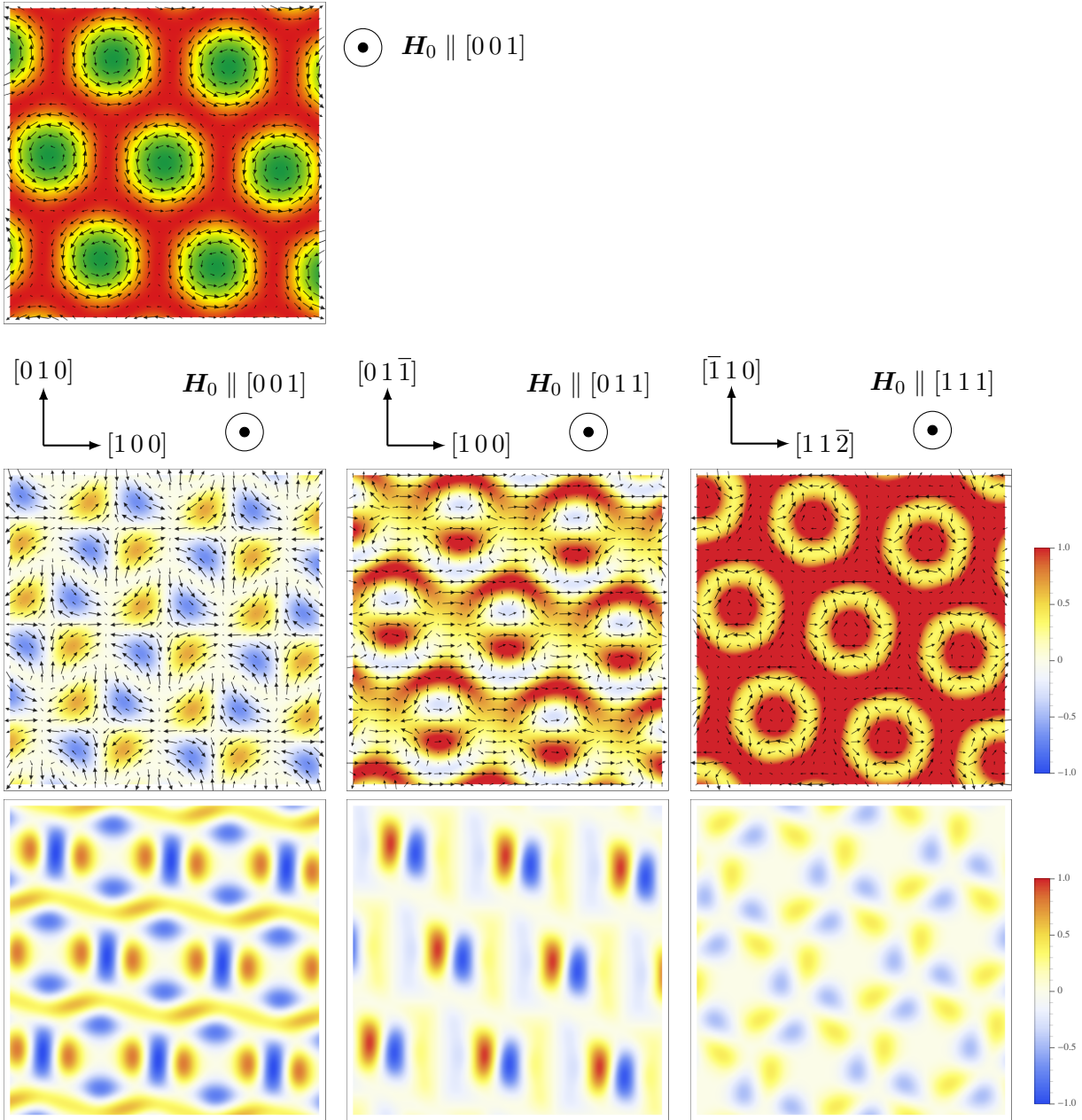


Figure 4.2: Top row: Magnetization in the Skyrmion Phase. Color coding represents the magnetization component in field direction (green = antiparallel, red = parallel). Arrows represent the in-plane components.

Middle row: The polarization of the Skyrmion phase in dependence of the magnetic field direction as shown by directional drawings above.

Bottom row: Local electric charge in the Skyrmion phase in dependence of the magnetic field direction.

The scaling of the density plots has been chosen as such, that one global maximal absolute value of the polarization (charge) component was set to be the global absolute value of the color coding scale. This lets us compare the relative strengths of the polarization (charge) for the different field direction to each other. For more details see text.

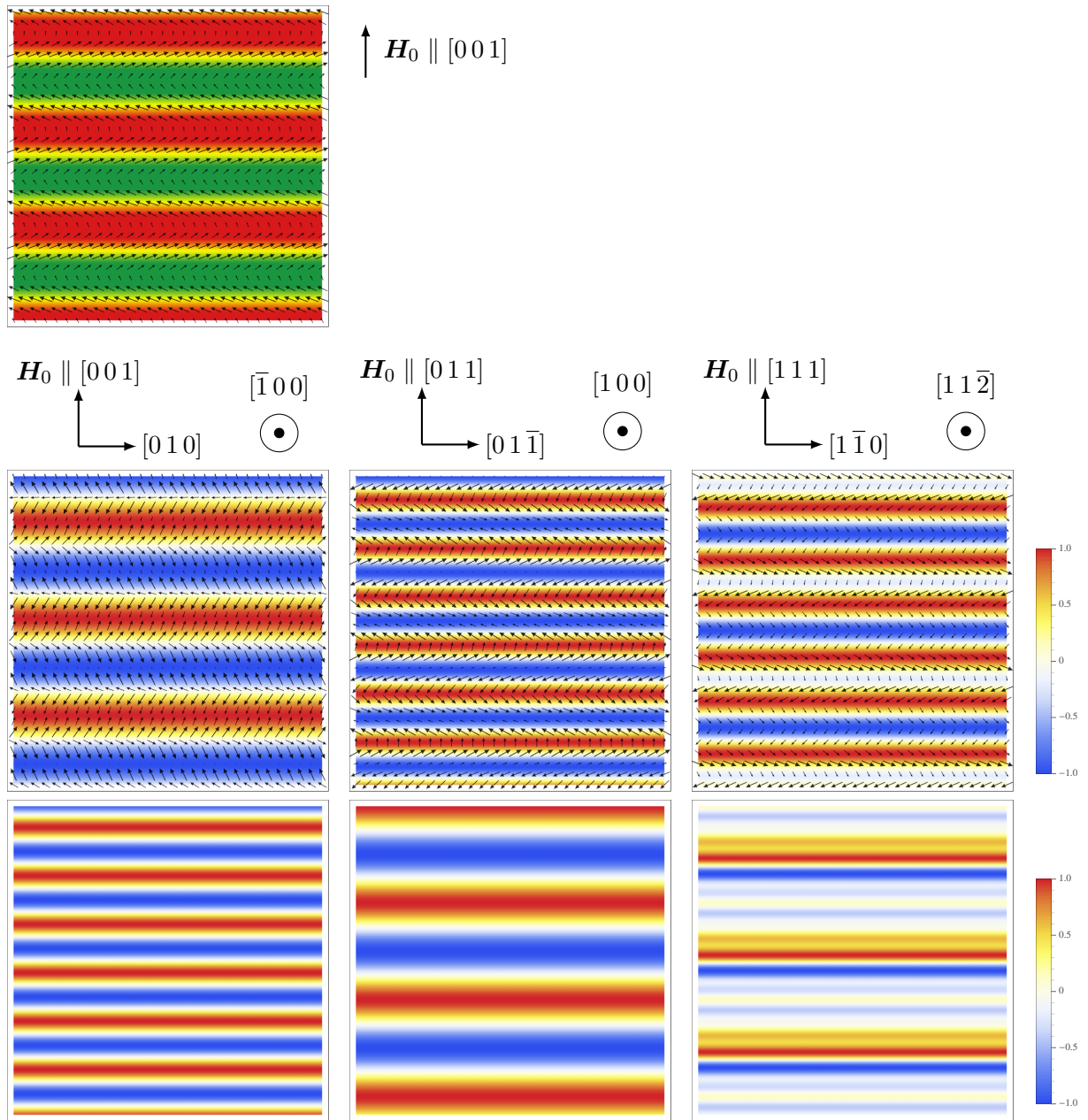


Figure 4.3: Top row: Magnetization in the conical Phase. Color coding represents the magnetization component perpendicular to the field direction (green = into the plane, red = out of the plane component). Arrows represent the in-plane components.

Middle row: The polarization of the conical phase in dependence of the magnetic field direction as shown by directional drawings above.

Bottom row: Local electric charge in the conical phase in dependence of the magnetic field direction. The scaling of the density plots has been done as such, that the minimum and maximum value of the polarization and charge, respectively, has been taken for each picture individually, and the color code interpolates between those two values. For more details see text.

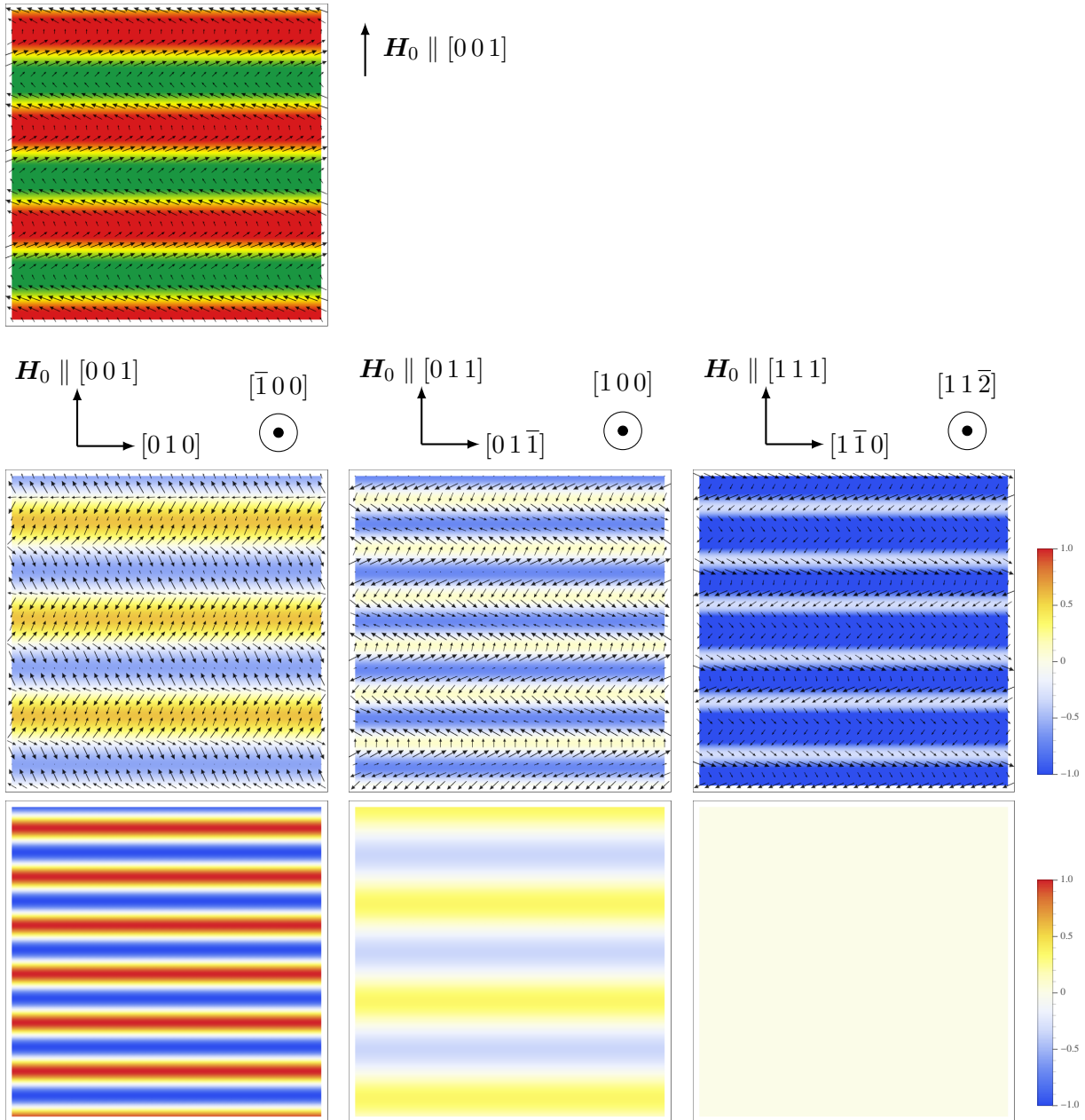


Figure 4.4: Top row: Magnetization in the conical Phase. Color coding represents the magnetization component perpendicular to the field direction (green = into the plane, red = out of the plane component). Arrows represent the in-plane components.

Middle row: The polarization of the conical phase in dependence of the magnetic field direction as shown by directional drawings above.

Bottom row: Local electric charge in the conical phase in dependence of the magnetic field direction. The scaling of the density plots has been chosen as such, that one global maximal absolute value of the polarization (charge) component was set to be the global absolute value of the color coding scale. This lets us compare the relative strengths of the polarization (charge) for the different field direction to each other. For more details see text.

4.2 Linear response and the field-polarized phase

Having now explained, that Skyrmions and helices induce an appreciable polarization, it seems likely, that the major influence in the resonance spectrum is also due to this substantial polarization. We hence pursue the goal to calculate the resonance frequencies analogously to magnetic excitations, only by now using the previously mentioned coupling term of an electric field to the polarization (4.4). Similarly to the magnetic case we start with an analytic calculation in the field-polarized phase and continue with numerical results for the conical and Skyrmion phases.

Before getting into more detail in the polarized phase, one key ingredient to our resonance theory needs to be deduced, namely $\boldsymbol{\xi} = \left. \frac{\delta \tilde{F}}{\delta \mathbf{M}} \right|_{\mathbf{M}^{MF}}$ in (2.28). Associating the terms properly, one arrives at

$$\tilde{F} = \int d^3r \mathbf{E}^\omega \cdot \mathbf{P} \quad (4.8)$$

Making a linear ansatz for the magnetization as $\mathbf{M}^{MF} + \delta \mathbf{M}$, one obtains

$$\mathbf{E}^\omega \cdot \mathbf{P} = \mathbf{E}^\omega \cdot \mathbf{P}^{MF} + \mathbf{E}^\omega \cdot \begin{pmatrix} 0 & M_z^{MF} & M_y^{MF} \\ M_z^{MF} & 0 & M_x^{MF} \\ M_y^{MF} & M_x^{MF} & 0 \end{pmatrix} \cdot \delta \mathbf{M} \quad (4.9)$$

and therefore

$$\boldsymbol{\xi} = \lambda \begin{pmatrix} 0 & M_z^{MF} & M_y^{MF} \\ M_z^{MF} & 0 & M_x^{MF} \\ M_y^{MF} & M_x^{MF} & 0 \end{pmatrix} \cdot \bar{\mathbf{E}} \quad (4.10)$$

It has to be noted, that its Fourier transform is now momentum dependent, since $\boldsymbol{\xi}$ depends explicitly on \mathbf{M}^{MF} . The projection direction $\hat{\mathbf{e}}^{out}$ in (2.31), to obtain the resonance weights, equally momentum dependent, because we assume the measurement to be of electrical nature as well.

4.2.1 Discussion of the field-polarized phase

As mentioned above, the direction of the homogeneous applied magnetic field \mathbf{H}_0 , plays a distinct role in the resonance behavior when using a term like (4.8). We pick the three aforementioned directions, i.e. [001], [110] and [111], to illustrate the differences and similarities between electric and magnetic excitations. We begin by going through the derivation of Kittel's formula for electric excitations in the case of $\mathbf{H}_0 \parallel \hat{\mathbf{e}}_z$.

Analogous to the calculation in subsection 3.2.1, we have a shift of the effective inner magnetic field compared to the externally applied fields. The difference to the shift in the magnetic case lies now in the direction and form of the exciting electric field contribution. The additional term to the effective magnetic field is

$$\mu_0 \mathbf{H}^{eff, el} = - \left. \frac{\delta \tilde{F}}{\delta \mathbf{M}} \right|_{\mathbf{M}^{MF}} = -\lambda \begin{pmatrix} M_z E_y^\omega + M_y E_z^\omega \\ M_z E_x^\omega + M_x E_z^\omega \\ M_y E_x^\omega + M_x E_y^\omega \end{pmatrix} \Big|_{\mathbf{M}^{MF}} \quad (4.11)$$

Let us assume as an example an electric excitation in y-direction, i.e. $\bar{\mathbf{E}} \parallel \hat{\mathbf{e}}_y$, to concretize the calculation. Together with $\mathbf{H}_0 \parallel \hat{\mathbf{e}}_z$, we obtain an analogous set of equations to (3.5).

$$\begin{aligned} H_x^i &= H_x^o - N_x M_x = -N_x M_x - \lambda M_z E_y^\omega \\ H_y^i &= H_y^o - N_y M_y = -N_y M_y \\ H_z^i &= H_z^o - N_z M_z = H_0 - N_z M_z - \lambda M_x E_y^\omega \end{aligned} \quad (4.12)$$

Note, that the electric analog to the demagnetization factors are not used here, because we assumed, that the oscillating electric field is small, as was the oscillating magnetic field compared to the static, external field for which the demagnetization factors were applied.

Neglecting again terms, that are not linear in $M_{x,y}$ or combinations between them and $E_{x,y}^\omega$, the equations of motions take the following form

$$\begin{aligned}\frac{dM_x}{dt} &= \gamma\mu_0 [H_0 + (N_y - N_z)M_z] M_y = \gamma\mu_0\eta_y M_y \\ \frac{dM_y}{dt} &= -\gamma\mu_0 [H_0 + (N_x - N_z)M_z] M_x - \gamma\mu_0\lambda M_z^2 E_y^\omega = -\gamma\mu_0\eta_x M_x - \gamma\mu_0\lambda M_z^2 E_y^\omega \\ \frac{dM_z}{dt} &\approx 0\end{aligned}\quad (4.13)$$

We can pick the same ansatz for the magnetization as in subsection 3.2.1. Plugging it and (4.6), i.e. the ansatz for the electric oscillation, into (4.13), yields

$$\omega\bar{M}_x = \gamma\mu_0\eta_y\bar{M}_y \quad (4.14a)$$

$$\omega\bar{M}_y = \gamma\mu_0\eta_x\bar{M}_x + \gamma\mu_0\lambda M_z^2 \bar{E}_y = \gamma^2\mu_0^2\eta_x\eta_y\frac{1}{\omega} + \gamma\mu_0\lambda M_z^2 \bar{E}_y \quad (4.14b)$$

In the last line we used (4.14a). Solving both equations for \bar{M}_x and \bar{M}_y lets us obtain

$$\bar{M}_x = -\lambda\frac{M_z}{1 - \frac{\omega^2}{\omega_0^2}} M_z \bar{E}_y \quad (4.15a)$$

$$\bar{M}_x = -\lambda\omega\frac{M_z}{1 - \frac{\omega^2}{\omega_0^2}} M_z \bar{E}_y \quad (4.15b)$$

where the resonance frequency ω_0 is again given by (3.10). Most interesting is the expression (4.15a), because, using the same conventions as in the magnetic case, it can be written as

$$\bar{M}_x = -\lambda\frac{\chi_x^0}{1 - \frac{\omega^2}{\omega_0^2}} M_z \bar{E}_y = -\lambda\chi_{xx}^{mag} M_z \bar{E}_y \quad (4.16)$$

Calculating the electric susceptibility, the upper expression comes in handy.

$$\chi_{yy}^{el} = \frac{\partial P_y}{\partial E_y} = \frac{\partial(M_z\bar{M}_x)}{\partial\bar{E}_y} = -\lambda\chi_{xx}^{mag} M_z \quad (4.17)$$

We find, that an oscillating electric field in y-direction corresponds to a magnetic field in x-direction and vice versa.

For an excitation parallel to the magnetic field in [001] direction, there is no response in first order, because $\mathbf{H}^{eff,el}$ contains only terms of quadratic order like $M_x E_z$. For excitations including the other two directions, the results are summarized in Table 4.1 according to [59]. One can see, that the situation for \mathbf{H}_0 in [110] direction is basically opposite to $\mathbf{H}_0 \parallel [001]$. In this case no resonances occur to linear order for excitations perpendicular to \mathbf{H}_0 . For $\mathbf{H}_0 \parallel [111]$ the situation is again similar to the [001] case.

4.2.2 Symmetry arguments in the field-polarized phase

The consideration of symmetry arguments to in- or to exclude physical phenomena is quite a common practice. Within the so far established setup, we can with their use check for consistency

Table 4.1: Dependence of electric excitations on the direction of the external magnetic field in the field-polarized phase.

$\mathbf{H}_0 \parallel [001]$	$\mathbf{E}^\omega \parallel \mathbf{H}_0$	\rightarrow	no excitation to linear order
	$\mathbf{E}^\omega \perp \mathbf{H}_0$	\rightarrow	$\mathbf{E}^\omega \parallel [100] \hat{=} \mathbf{H}^\omega \parallel [010]$ $\mathbf{E}^\omega \parallel [010] \hat{=} \mathbf{H}^\omega \parallel [100]$
$\mathbf{H}_0 \parallel [110]$	$\mathbf{E}^\omega \parallel \mathbf{H}_0$	\rightarrow	$\mathbf{E}^\omega \parallel [110] \hat{=} \mathbf{H}^\omega \parallel [001]$
	$\mathbf{E}^\omega \perp \mathbf{H}_0$	\rightarrow	no excitation to linear order
$\mathbf{H}_0 \parallel [111]$	$\mathbf{E}^\omega \parallel \mathbf{H}_0$	\rightarrow	no excitation to linear order
	$\mathbf{E}^\omega \perp \mathbf{H}_0$	\rightarrow	$\mathbf{E}^\omega \parallel [1\bar{1}0] \hat{=} \mathbf{H}^\omega \parallel [1\bar{1}0]$
		\rightarrow	$\mathbf{E}^\omega \parallel [11\bar{2}] \hat{=} \mathbf{H}^\omega \parallel [1\bar{1}0]$

with the perturbatively obtained results.

The applied magnetic field \mathbf{H}_0 breaks certain symmetries of the crystal. Therefore, not all so far possible terms in the dynamical polarization are allowed. As an example, we consider again a magnetic field parallel to $[001]$.

Due to the magnetic field, only three symmetries are left: rotation around the field axis by π , and rotations by π around the other two $\langle 100 \rangle$ axes combined with time reversal. The dynamic polarization is given by

$$\mathbf{P}_{[001]} = \lambda \begin{pmatrix} M_z \delta M_y \\ M_z \delta M_x \\ \delta M_x \delta M_y \end{pmatrix} \approx \lambda \begin{pmatrix} M_z \delta M_y \\ M_z \delta M_x \\ 0 \end{pmatrix} \quad (4.18)$$

The effects of the symmetry transformations are either accompanied by a sign change of the magnetization and polarization, respectively, or not. The effects of the three transformations to the individual components are shown in Table 4.2. Sign changes are denoted by a minus sign in the table and if the symmetry transformation has no effect on $\delta \mathbf{M}$ or the polarization, a plus sign stands in its place. While the couplings of P_x (P_y) and δM_y (δM_x) are perfectly allowed, a linear coupling of $\delta \mathbf{M}$ to P_z is even forbidden on symmetry grounds. Remarkably, this restriction is already caused by rotation symmetry alone, without a time reversal.

For the $[110]$ direction, a similar analysis can be made. It turns out, however, that symmetry arguments do not yield further restrictions to the otherwise obtained excitations, whether linear in $\delta \mathbf{M}$ or not. One can use this result, on the other hand, to verify, that the obtained linear couplings are indeed allowed. The dynamic polarization is given by

$$\mathbf{P}_{[110]} = \lambda \begin{pmatrix} \frac{1}{\sqrt{2}} M_1 (M - M_2) \\ \frac{1}{\sqrt{2}} M_1 (M + M_2) \\ \frac{1}{2} (M + M_2) (M - M_2) \end{pmatrix} \approx \lambda \begin{pmatrix} \frac{1}{\sqrt{2}} M_1 M \\ \frac{1}{\sqrt{2}} M_1 M \\ \frac{1}{2} M^2 \end{pmatrix} \quad (4.19)$$

To this end, we decompose the magnetization again into a *big* part parallel to the magnetic field, and a perturbation $\delta \mathbf{M}$ perpendicular to it, as

$$\mathbf{M} = \frac{M}{\sqrt{2}} \begin{pmatrix} 1 \\ 1 \\ 0 \end{pmatrix} + \underbrace{M_1 \begin{pmatrix} 0 \\ 0 \\ 1 \end{pmatrix} + \frac{M_2}{\sqrt{2}} \begin{pmatrix} 1 \\ -1 \\ 0 \end{pmatrix}}_{\delta \mathbf{M}} \quad (4.20)$$

Table 4.2: List of symmetry transformations (left column) and their effect on the polarization and the magnetization for a magnetic field \mathbf{H}_0 in $[001]$ direction. Time reversal is expressed by T and a rotation about an angle φ around the axis \hat{e} by $R_{\hat{e}}^\varphi$.

	P_x	P_y	P_z	δM_x	δM_y
$R_{[001]}^\pi$	-	-	+	-	-
T $R_{[010]}^\pi$	-	+	-	+	-
T $R_{[100]}^\pi$	+	-	-	-	+

Table 4.3: Effect of the symmetry transformation on the polarization and the magnetization for a magnetic field \mathbf{H}_0 in $[1\bar{1}0]$ direction. Time reversal is expressed by T and a rotation about an angle φ around the axis \hat{e} by $R_{\hat{e}}^\varphi$.

	$P_{[100]}$	$P_{[0\bar{1}1]}$	$P_{[011]}$	$\delta M_{[0\bar{1}1]}$	$\delta M_{[001]}$
T $R_{[001]}^\pi$	+	-	-	+	-

The effect of the allowed symmetry transformation is shown in Table 4.3.

In the case of $\mathbf{H}_0 \parallel [111]$ the system is invariant under the rotation $R_{[111]}^{\frac{2}{3}\pi}$. If one would decompose the magnetization like above into a parts parallel and perpendicular to \mathbf{H} , the perpendicular component would not stay on the same axis, so that it the rotation would correspond to a spacial inversion, but gets rotated away from it. An excitation in that direction would comply with that result and is hence not allowed as has also been confirmed by the calculation to obtain Table 4.1.

4.2.3 Numerical calculation of the resonance frequencies

The more complicated form of the resonance spectrum in the conical and Skyrmion phases is calculated numerically. The transition into the field-polarized phase happens automatically for large enough magnetic fields and is hence also included in the calculations. The parts, within the numerical calculation for electric excitations, that differ from the calculations with a magnetic excitation are, for one, the already explained momentum dependent $\boldsymbol{\xi}$ but also the directional dependence, whose implementation is as follows. It may be noted, that a goal was to keep the description of the coupling term in the free energy in terms of one coordinate system to minimize numerical effort.

For the case, where $\mathbf{H}_0 \parallel [001]$, the formula for the polarization stays as defined in (4.3). This gives a certain expression C for the coupling term as shown above, where the polarization is described by the components of the local magnetization in coordinates canonical to the cubic system:

$$C = \mathbf{E} \cdot \mathbf{P}|_M \quad (4.21)$$

The rotation of the magnetic field to a new direction, say \mathbf{H}' , leads to a new arrangement of the local magnetization $\mathbf{M}' = \underline{R}' \cdot \mathbf{M}$, where \underline{R}' stands for the rotation matrix, that transforms a vector $\{0, 0, 1\}^T$ into a vector \hat{e}' , like for instance $\{0, 1, 1\}^T/\sqrt{2}$ or $\{1, 1, 1\}^T/\sqrt{3}$ in our case. Plugging this transformed magnetization into \mathbf{P} , yields a transformed polarization \mathbf{P}' , that still consists of the magnetization components described in the old coordinate system. To get the

4 Electric Excitations

correct coupling term for the new field direction, the electric field direction needs to be rotated via \underline{R}' as well.

$$C' = \mathbf{E}' \cdot \mathbf{P}|_{M'} = (\underline{R}'\mathbf{E}) \cdot \mathbf{P}|_{\underline{R}'M} \quad (4.22)$$

This term can then be decomposed into

$$C' = \mathbf{E} \cdot \underline{K} \cdot \mathbf{M} = E_i \frac{\partial C'}{\partial E_i \partial M_j} M_j \quad (4.23)$$

that can be used to obtain $\boldsymbol{\xi}$ for the new orientation (cf. (4.9)).

Numerical results and plots

Numerical results for the conical phase are shown in Figure 4.7 in form of bubble-resonance plots, where the resonance weight is like before proportional to the area of the bubble. For the calculations themselves, we have assumed a spherical shape of the specimen and $\tilde{\chi}_{\text{con}}^{\text{sphere}} = 1$. The plots are arranged in a grid, where rows relate to a mutual magnetic field direction and columns to the direction of the oscillating electric field. The first two columns contain graphs of excitations perpendicular to the magnetic field direction, with both of those directions being perpendicular to each other. The third column shows excitations parallel to \mathbf{H}_0 and the last column unites all of the previous excitations. For a comparison to the case of magnetic excitations, the resonances of the conical and field-polarized phases are shown as a reference by a dashed line. It may be noted, that we have not included directional dependence in those reference lines, because there would be none for longitudinal excitations. these conventions are also used in Figure 4.8.

A first thing to check, is whether the previously performed theoretical predictions for the field-polarized phase hold. Comparing the diagrams to Table 4.1, one finds that they do agree with our numerical results or vice versa. For example, no excitation is found for $\mathbf{H}_0 \parallel [011]$ when $\mathbf{E}^\omega \perp \mathbf{H}_0$ for values of $|\mathbf{H}_0| > H_{c2}$. Concerning the comparison to the magnetic excitations, one can see for the here considered coupling to the polarization, that the plus and minus Q modes are electrically excited in numerous directions as well. The most noteworthy difference is the appearance of an additional mode at slightly more than twice the frequency of the two original modes. It also seems to be doubly degenerate.

An analogous grid of plots for the resulting resonance frequencies in the Skyrmion phase is shown in Figure 4.8. On first sight, it seems like a plethora of cluttered points. Shown here are however all numerically obtained points, including the previously mentioned fluctuating mini-modes, i.e. modes with vanishingly small weight. The shown calculations have been done by including 3 rings of \mathbf{Q} -vectors to obtain a fairly stable result for the modes with considerable weight. It also needs to be noted, that the potentially, experimentally realized portion of the shown frequencies lies only in a small magnetic field range within $H_0 = 0$ and $H_0 = H_{c2}$, cf. Figure 3.11. Again, the conical excitations are shown as a reference line. A first consistency check reveals, that the ferromagnetic excitations coincide also here with the predictions made in Table 4.1.

Most remarkable is, that calculations for Skyrmion crystals show several additional modes when excited electrically according to the here described approach, than magnetically. Liu and collaborators [55] studied these modes as well and present three cases (I-III), shown in Figure 4.5(I), that relate to the in Figure 4.8 shown subfigures (A3), (B1) and (C3), respectively. Liu *et al.* [55] compare their findings to magnetic resonance frequencies calculated by Mochizuki *et al* [50], which provides a good reference of where their calculated frequencies lie in our plots. One can identify his R1 and R2 modes with the clockwise and counter-clockwise modes as well as B1 with the already magnetically excited breathing mode. The other four modes (E, X1, X2 and B2) are also found in our calculation and are labeled accordingly in the appropriate plots in

Figure 4.8. We find very good agreement.

In their most recent work, Mochizuki *et al.* [58] also studied electric excitations. Their comparison to the magnetic excitations is shown in Figure 4.5(II) In their case, $\mathbf{H}_0 \parallel \langle 110 \rangle$ and they excite both longitudinal (red line in the lower part of the figure) and perpendicular (blue dashed line) to \mathbf{H}_0 . These cases relate well to subfigures (B3) and (B1) in Figure 4.8, when remembering that his convention for clockwise and counterclockwise is opposite to ours. Unfortunately, their shown frequency range does not suffice to be able to compare the high frequency modes.

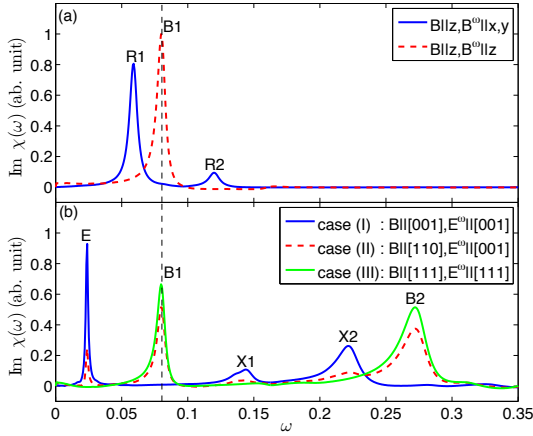


Figure 4.5(I): Spectra by Liu *et al.* [55]. The upper portion has its origin in Mochizuki's work [50].

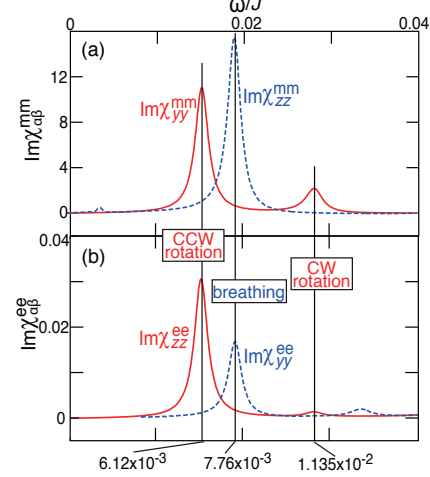


Figure 4.5(II): Spectra by Mochizuki *et al.* [58]. The magnetic field direction is given by $\mathbf{H}_0 \parallel \hat{e}_z \parallel \langle 110 \rangle$.

Figure 4.5: Comparison of calculated absorption spectra for a.c. uniform magnetic (a) and electric (b) fields for different directions.

4.2.4 Conflicts and prospects

While the upper calculation show nice analogies to the magnetic excitations, recently conducted and still unpublished experiments by the research group of PD Dr. Hemberger from Cologne indicate, that some assumptions made for the calculations above might not yield a proper description of the experimentally measured resonances, It seems like they need to be at least extended by further arguments. Potential disagreement ranges from the presence of measured resonances that should have been excluded, according to the calculations done so far, to additional occurring excitations, which cannot be described by the previous assumption of how the electric field couples to the magnetic structure.

A solution to this problem could potentially be obtained by a coupling term not yet included in the electric theory, for example

$$f^* = \mathbf{M} \cdot \partial_t \mathbf{E} \quad (4.24)$$

This is a term invariant under time reversal symmetry, as well as rotationally invariant and hence perfectly allowed in our situation. Taking Maxwell's equation $\epsilon_0 \partial_t \mathbf{E} = \nabla \times \mathbf{H}$ into account and plugging it into (4.24), a resemblance to the Dzyaloshinsky-Moriya interaction becomes evident.

$$f^* = \frac{1}{\epsilon_0} \mathbf{M} \cdot (\nabla \times \mathbf{H}) \quad (4.25)$$

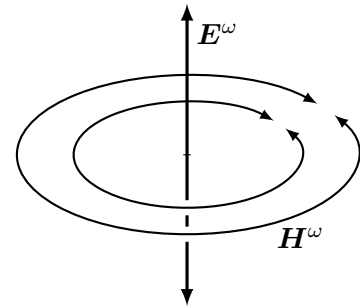


Figure 4.6: Figure of the magnetic field induced by a changing electric field.

4 Electric Excitations

This formulation also incorporates the fact, that a changing electric field results in a two dimensional circular field as shown in Figure 4.6, whereas the previous calculations were done with an excitation, that is directed in only one direction. Elaborate calculations with this additional insight are current work in progress.

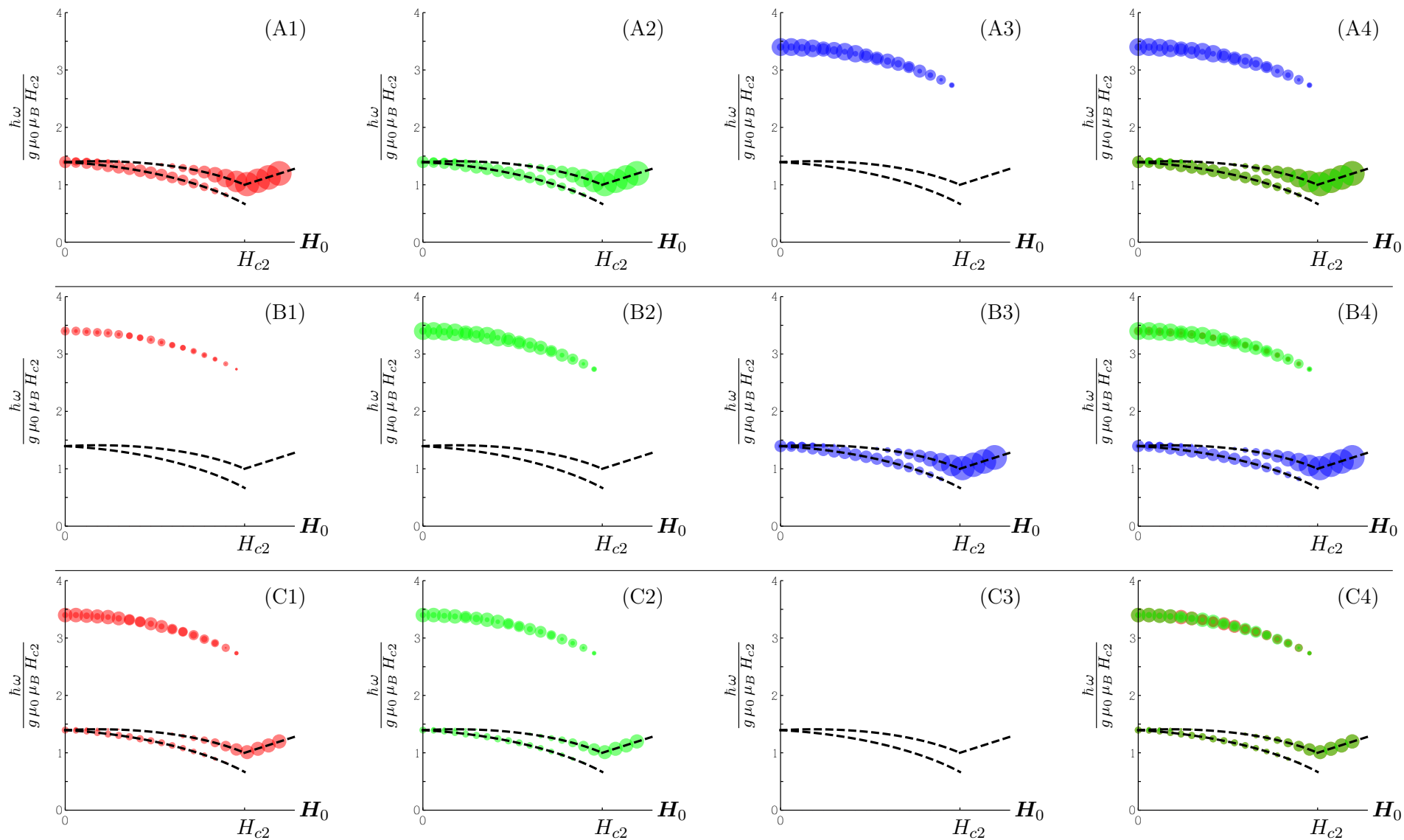


Figure 4.7: Electric resonances in the conical phase - (A1-A4): $H_0 \parallel [001]$, (B1-B4): $H_0 \parallel [011]$, (C1-C4): $H_0 \parallel [111]$; (A1-C1) and (A2-C2): $\mathbf{E}^\omega \perp \mathbf{H}_0$ and $\mathbf{E}_{(1)}^\omega \perp \mathbf{E}_{(2)}^\omega$, (A3-C3): $\mathbf{E}^\omega \parallel \mathbf{H}_0$; (A4-C4): All plots of same letter together in one. The dashed line shows the resonance frequencies in the conical and field-polarized phase of magnetic excitations as a reference. The demagnetization factors are that from a sphere. For more details see text.

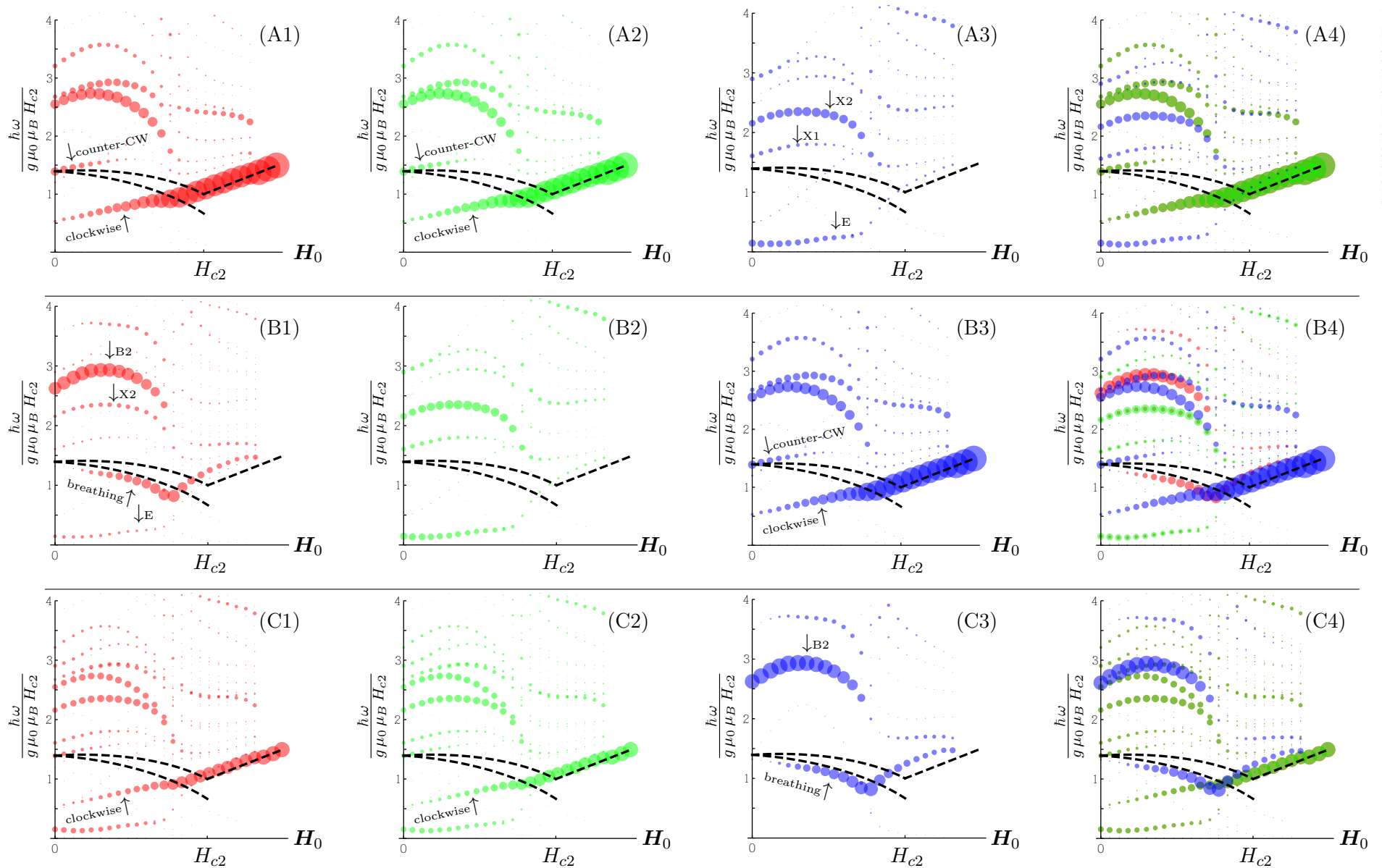


Figure 4.8: Electric resonances in the Skyrmion phase - (A1-A4): $H_0 \parallel [001]$, (B1-B4): $H_0 \parallel [011]$, (C1-C4): $H_0 \parallel [111]$; (A1-C1) and (A2-C2): $\mathbf{E}^\omega \perp \mathbf{H}_0$ and $\mathbf{E}_{(1)}^\omega \perp \mathbf{E}_{(2)}^\omega$, (A3-C3): $\mathbf{E}^\omega \parallel \mathbf{H}_0$; (A4-C4): All plots of same letter together in one. The dashed line shows the resonance frequencies in the conical and field-polarized phase of magnetic excitations as a reference. The demagnetization factors are that from a sphere. For more details see text.

Summary

In the present thesis, the behavior of chiral magnets, which accommodate helical spin structures and magnetic Skyrmion lattices, was studied under the influence of oscillating magnetic and electric fields. The major part of the thesis dealt with the calculation of resonance frequencies and their corresponding weights. The formulation of the theory for resonances due to magnetic excitations was accompanied and influenced by experimental results provided by research group around Prof. Dr. Pfeleiderer and Prof. Dr. Grundler of the Technical University of Munich. For the electric excitations, we presented an analogous approach.

Our general analysis was based upon a linear response theory. While resonance frequencies were calculated numerically for all different phases, it was also possible to provide some analytical expressions in agreement with the numerical calculations. This was achieved for the field-polarized phase in both cases and for magnetic excitations even in the conical phase.

In the part of this thesis contributed to magnetic excitations only, we refer to three specific experimental measurements. A big part of the work was to incorporate sample-shape dependent demagnetization factors into the theory for both numerical and analytical results. An extension to not completely homogeneous excitation fields concluded that chapter. The highlight of the developed theory was, that it was not only possible to explain the resonance frequencies for the different materials individually, but on a universal basis that was independent of the conducting properties of the specimen and, most prominently, of temperature. Merely the sample-shape and the approximately constant, conical susceptibility were needed.

Within the chapter about electric excitations it was explained in an analogous manner, how resonance spectra would look like, if the coupling of the oscillating electric field to the magnetization comes about via an effective coupling of the electric field to a polarization. The latter is induced by the non-trivial magnetic texture. The structure of the induced polarization was described as well. Recently conducted experiments by the research group of PD Dr. Hemberger in Cologne hint, that this form of coupling might not yield the biggest contribution to the resonance frequencies. Current work on electric excitations leave exciting prospects for the future.

Bibliography

- [1] M. Faraday, "A course of six lectures on the various forces of matter and their relations to each other", (1860).
- [2] T. H. R. Skyrme, "A unified field theory of mesons and baryons", *Nucl. Phys.* **31**, 556 (1962).
- [3] A. N. Bogdanov and D. A. Yablonskii, "Thermodynamically stable "vortices" in magnetically ordered crystals. The mixed state of magnets", *Sov. Phys. JETP* **68**, 1 (1989).
- [4] S. Mühlbauer *et al.*, "Skyrmion Lattice in a Chiral Magnet", *Science* **323**, 915 (2009).
- [5] X. Z. Yu *et al.*, "Near room-temperature formation of a skyrmion crystal in thin-films of the helimagnet FeGe", *Nature Materials* **10**, 106 (2010).
- [6] W. Münzer *et al.*, "Skyrmion lattice in the doped semiconductor $\text{Fe}_{1-x}\text{Co}_x\text{Si}$ ", *Physical Review B* **81**, 041203 (2010).
- [7] S. Seki, X. Z. Yu, S. Ishiwata, and Y. Tokura, "Observation of Skyrmions in a Multiferroic Material", *Science* **336**, 198 (2012).
- [8] X. Z. Yu *et al.*, "Real-space observation of a two-dimensional skyrmion crystal", *Nature* **465**, 901 (2010).
- [9] P. Milde *et al.*, "Unwinding of a skyrmion lattice by magnetic monopoles", *unpublished* (2013).
- [10] A. Fert, V. Cros, and J. Sampaio, "Skyrmions on the track", *Nature Nanotechnology* **8**, 152 (2013).
- [11] F. Jonietz *et al.*, "Spin Transfer Torques in MnSi at Ultralow Current Densities", *Science* **330**, 1648 (2010).
- [12] T. Schulz *et al.*, "Emergent electrodynamics of skyrmions in a chiral magnet", *Nature Physics* **8**, 301 (2012).
- [13] K. Everschor *et al.*, "Rotating skyrmion lattices by spin torques and field or temperature gradients", *Physical Review B* **86**, 054432 (2012).
- [14] C. Pfleiderer and A. Rosch, "Single skyrmions spotted", *Nature* **465**, 880 (2010).
- [15] N. Ashcroft and D. Mermin, *Solid State Physics* (Harcourt College Publishers, Orlando, 1976).
- [16] P. M. Chaikin and T. C. Lubensky, *Principles of condensed matter physics*, 3 ed. (Cambridge University Press, Cambridge, 2006).

Bibliography

- [17] I. Dzyaloshinsky, “A thermodynamic theory of “weak” ferromagnetism of antiferromagnetics”, *Journal of Physics and Chemistry of Solids* **4**, 241 (1958).
- [18] T. Moriya, “Anisotropic Superexchange Interaction, and Weak Ferromagnetism”, *Physical Review* **120**, 91 (1960).
- [19] A. Leonov, Ph.D. thesis, TU Dresden, Dresden, 2011.
- [20] K. Everschor, M. Garst, R. Duine, and A. Rosch, “Current-induced rotational torques in the skyrmion lattice phase of chiral magnets”, *Physical Review B* **84**, 064401 (2011).
- [21] N. Manyala *et al.*, “Large anomalous Hall effect in a silicon-based magnetic semiconductor”, *Nature* **3**, 255 (2004).
- [22] Y. Ishikawa, G. Shirane, J. A. Tarvin, and M. Kohgi, “Magnetic excitations in the weak itinerant ferromagnet MnSi”, *Physical Review B* **16**, 4956 (1977).
- [23] S. Grigoriev *et al.*, “Magnetic Structure of Fe_{1-x}Co_xSi in a Magnetic Field Studied via Small-Angle Polarized Neutron Diffraction”, *Physical Review B* **76**, 224424 (2007).
- [24] K. Kohn, “A New Ferrimagnet Cu₂SeO₄”, *Journal of the Physical Society of Japan* **42**, 2065 (1977).
- [25] A. Bauer *et al.*, “Quantum phase transitions in single-crystal Mn_{1-x}Fe_xSi and Mn_{1-x}Co_xSi: Crystal growth, magnetization, ac susceptibility, and specific heat”, *Physical Review B* **82**, 064404 (2010).
- [26] A. Bauer (private communication).
- [27] T. Adams *et al.*, “Long-Wavelength Helimagnetic Order and Skyrmion Lattice Phase in Cu₂OSeO₃”, *Physical Review Letters* **108**, 237204 (2012).
- [28] M. Janoschek *et al.*, “Fluctuation-induced first-order phase transition in Dzyaloshinskii-Moriya helimagnets”, *Physical Review B* **87**, 134407 (2013).
- [29] T. Adams *et al.*, “Long-Range Crystalline Nature of the Skyrmion Lattice in MnSi.”, *Physical Review Letters* **107**, 217206 (2011).
- [30] O. Nakanishi, A. Yanase, A. Hasegawa, and M. Kataoka, “The origin of the helical spin density wave in MnSi”, *Solid State Communications* **35**, 995 (1980).
- [31] P. Bak and M. H. Jensen, “Theory of helical magnetic structures and phase transitions in MnSi and FeGe”, *Journal of Physics C: Solid State Physics* **13**, L881 (2000).
- [32] K. Everschor, Ph.D. thesis, University of Cologne, Cologne, 2012.
- [33] M. Garst (private communication).
- [34] C. Kittel, “Interpretation of Anomalous Larmor Frequencies in Ferromagnetic Resonance Experiment”, *Physical Review* **71**, 270 (1947).
- [35] W. F. Brown, *Magnetostatic Principles in Ferromagnetism, Selected topics in solid state physics* (North-Holland Pub. Co., Amsterdam, 1962).
- [36] M. S. Livingston, *Particle Physics - The high energy frontier* (McGraw-Hill, Berkeley, 1968).

- [37] T. H. R. Skyrme, “A Non-Linear Field Theory”, *Proceedings of the Royal Society A: Mathematical, Physical and Engineering Sciences* **260**, 127 (1961).
- [38] S. Buhrandt and L. Fritz, “The phase diagram and thermodynamics of three-dimensional chiral magnets in a magnetic field from Monte Carlo simulations”, *unpublished* (2013).
- [39] C. Kittel, *Einführung in die Festkörperphysik*, 8 ed. (R. OldenbourgVerlag, München, 1989).
- [40] K. Kopitzki and P. Herzog, *Einführung in die Festkörperphysik*, 6 ed. (Vieweg & Teubner, Wiesbaden, 2007).
- [41] D. Belitz, T. Kirkpatrick, and A. Rosch, “Theory of helimagnons in itinerant quantum systems”, *Physical Review B* **73**, 054431 (2006).
- [42] A. Altland and B. Simons, *Condensed Matter Field Theory*, 1 ed. (Cambridge University Press, New York, 2007).
- [43] I. Stasinopoulos *et al.*, in *DPG Spring Conference* (Regensburg, 2013).
- [44] Y. Onose *et al.*, “Observation of Magnetic Excitations of Skyrmion Crystal in a Helimagnetic Insulator Cu_2OSeO_3 ”, *Physical Review Letters* **109**, 037603 (2012).
- [45] C. Bilzer, Ph.D. thesis, Paris-Sud 11, Paris, 2007.
- [46] T. Schwarze (private communication).
- [47] C. Kittel, “On the Theory of Ferromagnetic Resonance Absorption”, *Physical Review* **73**, 155 (1948).
- [48] M. Kataoka, “Spin Waves in Systems with Long Period Helical Spin Density Waves Due to the Antisymmetric and Symmetric Exchange Interactions”, *Journal of the Physical Society of Japan* **56**, 3635 (1987).
- [49] M. Date, K. Okuda, and K. Kadowaki, “Electron Spin Resonance in the Itinerant-Electron Helical Magnet MnSi ”, *Journal of the Physical Society of Japan* **42**, 1555 (1977).
- [50] M. Mochizuki, “Spin-Wave Modes and Their Intense Excitation Effects in Skyrmion Crystals”, *Physical Review Letters* **108**, 017601 (2012).
- [51] C. Herring and C. Kittel, “On the Theory of Spin Waves in Ferromagnetic Media”, *Physical Review* **81**, 869 (1951).
- [52] S.-W. Cheong and M. Mostovoy, “Multiferroics: a magnetic twist for ferroelectricity”, *Nature Materials* **6**, 13 (2007).
- [53] T. Kimura *et al.*, “Magnetic control of ferroelectric polarization”, *Nature* **426**, 55 (2003).
- [54] J. D. Jackson, *Classical Electrodynamics*, 6 ed. (John Wiley & Sons, Inc., New York, 1967).
- [55] Y.-H. Liu, Y.-Q. Li, and J. H. Han, “Skyrmion dynamics in multiferroic insulators”, *Physical Review B* **87**, 100402 (2013).
- [56] S. Seki, S. Ishiwata, and Y. Tokura, “Magnetoelectric nature of skyrmions in a chiral magnetic insulator Cu_2OSeO_3 ”, *Physical Review B* **86**, 060403 (2012).
- [57] M. Mostovoy, “Ferroelectricity in Spiral Magnets”, *Physical Review Letters* **96**, 067601 (2006).

Bibliography

- [58] M. Mochizuki and S. Seki, “Magnetoelectric resonances and predicted microwave diode effect of the skyrmion crystal in a multiferroic chiral-lattice magnet”, *Physical Review B* **87**, 134403 (2013).
- [59] K. Everschor (private communication).

Acknowledgements

First of all, I would like to thank my supervisor Prof. Dr. Achim Rosch for providing me with the opportunity to work on such an interesting and rewarding project. His endless enthusiasm and drive to discover have inspired me from the start. Despite the extent of his research group, he was always able to find time for me and provided more than a helping hand when I had questions.

My gratitude is also owed to Priv.-Doz. Dr. Markus Garst for his utter patience, numerous discussions and guidance throughout the year. He always took time to answer my questions no matter how big or small.

A special *thank you* deserves Dr. Karin Everschor-Sitte for always being there to lend a hand and especially for her exceeding and meticulous proof reading.

Furthermore, I wish to thank the experimental physics groups from Munich and Cologne for insightful conversations, the experimental data used in this thesis and a vivid cooperation.

Working on this thesis would not have been the same without the influence of the entire Solid State Theory group at the University of Cologne. I am grateful for the excellent working atmosphere that was both entertaining as well as highly educative due to the great communicative interchange between colleagues.

Last but not least, I would like to thank my parents and my sister for their endless support throughout my studies.

Erklärung

Hiermit versichere ich, die vorliegende Arbeit selbstständig und ohne fremde Hilfe angefertigt zu haben. Verwendete Literatur und andere Unterlagen sind jeweils im Text vermerkt und im Literaturverzeichnis aufgelistet.

Köln, 2013-04-15

Johannes Waizner